

Characterization of the amyloid precursor α -synuclein
by NMR spectroscopy

Dissertation

zur Erlangung des Doktorgrades

der Mathematisch-Naturwissenschaftlichen Fakultäten

der Georg-August-Universität zu Göttingen

vorgelegt von

Hai-Young Kim

aus Pusan, Süd Korea

Göttingen 2008

D7

Referent: Prof. Dr. Ulf Diederichsen

Korreferent: Prof. Dr. Christian Griesinger

Tag der mündlichen Prüfung:

Abstract

A number of human neurodegenerative diseases, including Alzheimer's and Parkinson's diseases (PD), are associated with the deposition of proteinaceous aggregates known as amyloid fibrils. Surprisingly, proteins with very different amino acid sequences and three-dimensional structures aggregate into amyloid fibrils that share common characteristics, such as a similar morphology and a specific β -sheet-based molecular architecture. This suggests that the ability to fibrillate is an intrinsic property of a polypeptide chain and that the native structure is not necessarily the only ordered structure that each protein can assume. An additional common property of aggregation into amyloid fibrils is the presence of partially or fully unfolded states of the misfolding proteins. Whereas there is increasing knowledge about the factors that drive aggregation, the structural characteristics of intermediates and the molecular details that determine the arrangement of misfolded proteins in amyloid fibrils are still only understood in outline. Here in **Chapter 3**, it is demonstrated, by a combination of solution-state and solid-state NMR spectroscopy, that the structure of amyloid fibrils of α -synuclein (α S) is directly correlated to the conformational properties of the unfolded state and monomeric state of misfolding proteins.

Amyloid fibrils have very high stability placing them among the strongest known biological materials. It can be dissociated by high concentrations of chemical denaturants or by high pressure. In **Chapter 4**, it is showed that amyloid fibrils formed by the protein α S, which constitute the insoluble aggregates found in brains of patients suffering from PD, are highly sensitive to low temperature. Despite their remarkable

stability to high temperature, mature amyloid fibrils of α S are rapidly dissociated into monomers and small aggregates in supercooled water at $-15\text{ }^{\circ}\text{C}$, without freezing.

Finally, **Chapter 5** sheds light on understanding the mechanisms that govern α S aggregation and toxicity in PD and related α -synucleinopathies by NMR in combination with other spectroscopic methods. It is demonstrated that the phosphorylation at S129 and S87 expands the structure of α S, increases the conformational flexibility of wt α S and inhibits its fibrillogenesis *in vitro*. In addition, the phosphorylation mimics (S129E and S129D) do not reproduce the effect of phosphorylation on the structural and aggregation properties of α S *in vitro*. However, the phosphorylation mimic S87E is able to mimic the effect of phosphorylation on the aggregation properties of α S *in vitro*.

Acknowledgements

사랑을 입은자는 그 곁에 안전히 거하리로다 여호와께서 그를 날이 맞도록 보호하시고

그로 자기 어깨 사이에 처하게 하시리로다 (신명기 33:12)

In an acknowledgement section such as this it is impossible to cover all persons who have directly or indirectly contributed to my years in Göttingen. However, there are some people that I wish to mention in particular.

I am deeply grateful to the director of the department **Prof. Dr. Christian Griesinger** and my direct supervisor **Prof. Dr. Markus Zweckstetter** for providing the opportunity to do my doctoral studies in an excellent scientific environment with outstanding equipments, encouragement and for their guidance in NMR, stimulating suggestions, support and immense faith in me.

I would also like to thank **Prof. Dr. Ulf Diederichsen** for accepting me as an external Ph.D. student in the Chemistry Faculty of the Georg-August Göttingen University and **Prof. Dr. Jörg Schroeder**, **Prof. Dr. Uwe Klingebiel**, **Prof. Dr. Franc Meyer** and **Prof. Dr. Michael Buback** for agreeing to be members of my external Ph.D. thesis committee.

I thank my collaborators with other laboratories, some of them presented on this thesis:

Prof. Dr. Marc Baldus and **Prof Dr. Henrike Heise** for solid state NMR experiments and useful suggestions.

Dr. Stefan Becker and **Karin Giller** for their help in the bio-lab and outstanding guidance in α -synuclein purification.

Dr. Rezaei-Ghaleh Nasrollah (Hessam), **Pinar Karpinar** and **Min-Kyu Cho** for their corporation, support and stimulating discussion in trouble-shooting tricky synuclein problems.

Dr. Dietmar Riedel for his electron microscopy images and his professional suggestion for the same.

Dr. Volker klauken and **Gerhard Wolf** for the training in peptide synthesis and HPLC and Mass spectroscopy analyzed.

Prof. Dr. Hilal Lashuel and **Katrina E. Paleologou** (at Brain Mind Institute in Lausanne, Switzerland) for their help in the aggregation study of phosphorylated α S.

Claudio O. Fernandez, **Gonzalo R. Lamberto**, at Instituto de Biología Molecular y Celular in Rosario, Argentina for their scientific discussion and support in α S phosphorylation.

Prof. Dr. Roland Benz and **Elke Maier** at Würzburg universität in Germany, for lipid bilayer membrane experiment and useful comments while analyzing synucline conductance data

I am grateful to all the present and former members of our group, who have contributed in every way to make my stay a very memorable one:

Monika, Marco, Nils, Sergey, Lukasz, Fernando, ShengQi, Julian, Laura, Dirk, Stefan, Stafen, Jörg, Peter, Mate, Melanie, Uwe, Valerie, Francesca, Ulrich, Anni, Gabi, Sebastian, Edith, Fabian, Edward, Sigrun, Adam, Carlos, Donghan, Nicolas, Tea, Irene, Raghavendran, Jürgen, and Carsten for their cordiality and the rest of my department for a delightful working atmosphere.

I would like to express my sincere gratitude to:

Dr. Shyamala Thirunavukkuarasu for unofficially but always very useful discussion for synuclein project and the thorough proofreading while still recovering from the baby birth and I wish all the best for ‘Vishwaved Vinesh’ who will be the great scientist.

Dr. Vinesh Vijayan who is my trusted friend who made my Göttingen pleasant and memorable and I sincerely thank his ‘Superman’ help when I had difficulties in spectrometer.

Dr. Young-Sang Jung for his faith in me, cheering me with simple, short meaningful conversations and his help in developing backbone assignment program (MARS).

Dr. Pierre Montaville for being my counsellor, more like a brotherly figure and giving me a chance to learn how to set ‘logics’ in science and life during ‘coffee break’.

Dr. Jegannath Korukottu for his happy greetings every morning, sharing emotions during my Ph.D. period and help in different computational aspects.

Mrs. Silberer Siegrid, secretary to Prof. Griesinger, for her helping attitude in dealing with bureaucratic and other paper works.

Prof. Dr. Wontae Lee for his constant support and advice from Korea.

Prof. Dr. K.Hun Mok for his scientific suggestion and his patient hearing to all my difficulties.

Pastor Jae-Jung An and the group of Goettingen Korean church people especially, **Eun-Jung Kim, Yong Shin, Yuna Park** and **Song-i Know** for their endless helping and cheering whenever I need.

Kyu-Young Han for useful discussions, teaching tennis and for his delicious Korean dinner.

Dr. Jung-Sup Rhee and **Sun-hae Park** for their kind supports and warm advice in my Göttingen life.

My deep and warm thanks go my two brothers **Hye-woong** and **Jin-woong** for their encouragement and affection, my aunt ‘**imong**’ for her care through mailing, prayers and visits to Goettingen, **Min-Kyu** for his love and helping from the first and till the end of my PhD journey. Last but not the least, I want to express all my thanks and love to **My parents** for their continuous love and prayers which gave me the strength to finish this thesis.

Publication list

This thesis is based on the following publications:

- (1) **Kim H-Y**, Heise H, Fernandez C.O, Baldus M and Zweckstetter M: Correlation of Amyloid Fibril beta-Structure with the Unfolded State of alpha-synuclein. *Chembiochem.* **2007**, Sep; 8(14):1671-1674. **(Chapter 3)**
- (2) **Kim H-Y**, Cho M-K, Riedel D, Fernandez C.O and Zweckstetter M: Dissociation of amyloid fibrils of α -synuclein in supercooled water. *Angew Chem Int Ed Engl.* **2008**, Jun; 47(27):5046-5048. **(Chapter 4)**
- (3) **Kim H-Y**, **Cho M-K**, Ashotosh K, Riedel D, Benz R, Fernandez C.O, Lashuel HA, Kügler S, Lange A, Griesinger C and Zweckstetter M: High-resolution characterization of the structure of toxic α -synuclein oligomers. (*In preparation*). **(Chapter 4)**
- (4) **Paleologou KE**, Schmid AW, Rospigliosi CC, **Kim H-Y**, Lamberto GR, Fredenburg RA, Lansbury, Jr. PT, Fernandez CO, Eliezer D, Zweckstetter M and Lashuel HA: Phosphorylation at 129, but not the phosphomimic S129E/D inhibits the fibrillization of alpha-synuclein. *J Biol Chem.* **2008**, Jun; 283(24):16895-16905. **(Chapter 5)**
- (5) **Paleologou KE**, Shakked G, Rospigliosi CC, **Kim H-Y**, Lamberto GR, Schmid A, Chiappe D, Moniate M, Eliezer D, Zweckstetter M, Masliah E and Lashuel HA: Potential physiological and pathological roles of α -synuclein phosphorylation at Serine 87. (*Submitted*). **(Chapter 6)**
- (6) **Montaville P**, **Kim H-Y**, Vijayan V, Becker S, Zweckstetter M. ^1H , ^{15}N , and ^{13}C resonance assignment of the C2A domain of rabphilin-3A. *J Biomol NMR.* **2006**; 36 Suppl 1:20 **(Appendix)**

Other publications:

- (7) Cho M-K, **Kim H-Y**, Bernado P, Fernandez C.O, Blackledge M, and Zweckstetter M: Amino Acid Bulkiness Defines the Local Conformations and Dynamics of Natively Unfolded α -synuclein and Tau. *J. Am. Chem. Soc.* **2007**, Mar; 129(11):3032-3033.

- (8) Skora L, Cho M-K, **Kim H-Y**, Becker S, Fernandez CO, Blackledge M and Zweckstetter M: Charge-Induced Molecular Alignment of Intrinsically Disordered Proteins. *Angew Chem Int Ed Engl.* **2006**, Oct; 45(42):7012-7015.

- (9) Cho M-K, **Kim H-Y**, Fernandez C.O, and Zweckstetter M: Secondary structure arrangements in amyloid fibrils of wild-type and A30P α -synuclein. (*in preparation*).

Table of contents

ABBREVIATIONS	XI
1. INTRODUCTION	14
1.1. Protein folding, misfolding and amyloid disease	14
1.1.1. Fibrillization and structure of amyloid fibrils	19
1.1.2. α -synuclein aggregation related to Parkinson's disease (PD)	20
1.2. Cold dissociation	22
1.3. NMR spectroscopy	26
1.3.1. <i>J</i> -couplings.....	26
1.3.2. Chemical shift.....	27
1.3.3. Nuclear Overhauser effect (NOE)	27
1.3.4. Paramagnetic relaxation enhancement (PRE).....	28
1.3.5. Diffusion ordered spectroscopy (DOSY).....	29
2. MATERIALS AND METHODS	33
2.1. Materials.....	33
2.1.1. Chemical reagents and enzymes	33
2.1.2. Bacterial strains.....	34
2.1.3. Oligonucleotide primers for mutagenesis of α -synuclein.....	34
2.1.4. Equipments	35
2.2. Methods.....	36
2.2.1. Molecular biology methods	36
2.2.1.1. Isolation of DNA	36
2.2.1.2. Site-directed mutagenesis of α -synuclein.....	37
2.2.1.3. DNA sequencing	37
2.2.1.4. Transformation of <i>E. coli</i>	37
2.2.2. Methods for protein biochemistry.....	38
2.2.2.1. Expression and purification of α -synuclein.....	38
2.2.2.2. Site-directed spin-labelling of proteins.....	40
2.2.2.3. Phosphorylation of α -synuclein <i>in vitro</i>	41
2.2.2.4. Synthesis of random coil peptides	41
2.2.2.5. Reversed phase-high performance liquid chromatography (RP-HPLC)	42

2.2.2.6. Sample preparation for supercooled water.....	42
2.2.2.7. Protein aggregation assay	43
2.2.2.8. Immunoblotting (dot blotting).....	44
2.2.3. NMR spectroscopy	46
2.2.3.1. ¹ H- ¹⁵ N HSQC.....	46
2.2.3.2. Paramagnetic relaxation enhancement (PRE)	48
2.3.3.3. Diffusion coefficient and hydrodynamic radius	49
2.2.3.4. Relaxation properties and motion.....	50
2.2.3.5. Secondary structure determination	51
2.2.3.6. Mapping of long-range interactions by chemical shift differences	51
2.2.4. Other spectroscopic methods	52
2.2.4.1. UV absorbance	52
2.2.4.2. Electrospray Quadrupole Mass spectrometry	53
2.2.4.3. Circular dichroism (CD) spectroscopy	53
2.2.4.4. Electron microscopy (EM)	53
3. CORRELATION OF AMYLOID FIBRIL β-STRUCTURE WITH THE UNFOLDED STATE OF α-SYNUCLEIN.....	55
3.1. Introduction	55
3.2. Experimental procedure.....	57
3.3. Results and discussion	57
3.3.1. Backbone assignment of α -synuclein at -15°C	57
3.3.2. Comparison of secondary chemical shifts and NOE intensity at $+15^{\circ}\text{C}$ and -15°C ..	60
3.3.3. Attenuation of transient long-range interactions in α -synuclein at -15°C	62
3.3.4. Correlation of amyloid β -structure with the unfolded state of α -synuclein.....	64
3.4. Conclusion.....	69
4. DISSOCIATION OF AMYLOID FIBRILS OF α-SYNUCLEIN IN SUPERCOOLED WATER.....	71
4.1. Introduction	71
4.2. Experimental procedure.....	73
4.3. Results and discussion	74
4.3.1. Dissociation of α -synuclein fibrils in supercooled water	74
4.3.1.1. Dissociation followed by real-time 2D ¹ H- ¹⁵ N HSQC NMR	76

4.3.1.2. Comparisons of biophysical properties: dissociated and native monomer of α -synuclein.....	77
4.3.1.3. Which interactions hold α -synuclein fibrils together?	80
4.3.2. Characterization of α -synuclein oligomers derived from amyloid fibrils through supercooled water	84
4.3.2.1. Quantification of oligomers.....	84
4.3.2.2. Morphology of the oligomers	86
4.3.2.3. α -synuclein oligomers are on-pathway to fibril formation.....	87
4.3.2.4. Toxicity induced by membrane pore formation	91
4.4. Conclusion	93
4.5. Outlook	94
5. BIOPHYSICAL STUDIES OF α-SYNUCLEIN PHOSPHORYLATION AND ITS AGGREGATION	95
5.1. Introduction	95
5.2. Experimental procedure.....	97
5.3. Results and discussion	99
5.3.1. α -synuclein phosphorylation at S129	99
5.3.1.1. α -synuclein is disordered independent of phosphorylation.....	100
5.3.1.2. Phosphorylation expands the ensemble of conformations populated by wt α -synuclein.....	102
5.3.1.3. S129E/D do not reproduce the structural consequences of phosphorylation	103
5.3.1.4. Phosphorylation disrupts transient intramolecular long-range interactions.....	104
5.3.1.5. S129E exhibits similar <i>in vitro</i> aggregation properties as wt α -synuclein	106
5.3.1.6. Phosphorylation at S129 is sufficient to inhibit the aggregation of wt α -synuclein	107
5.3.2. α -synuclein phosphorylation at S87	111
5.3.2.1. Phosphorylation at S87 is sufficient to block α -synuclein fibrillization and phosphomimic S87E aggregates slower than wt and S87A	111
5.3.2.2. α -synuclein S \rightarrow A and S \rightarrow E mutations can mimic S87, but not S129, phosphorylation	113
5.3.2.3. α -synuclein is disordered independent of phosphorylation at S87.....	115
5.3.2.4. Kinetics of wt and mutants α -synuclein phosphorylation	117

5.3.2.5. Neither S87 nor S129 phosphorylation is required for LBs formation.....	120
5.4. Conclusion.....	122
6. BIBLIOGRAPHY	124
7. APPENDIX.....	140
7.1. Backbone assignment of wt α -synuclein at $-15\text{ }^{\circ}\text{C}$	140
7.2. Backbone assignment of the C2A domain of Rabphilin-3A using the automatic assignment program MARS	143
7.3. Protocol of the automatic assignment program MARS.....	148
7.4. Pulse programs of PG-SLED and (HA)CANNH	156
CURRICULUM VITAE.....	168

Abbreviations

Aβ	Amyloid- β peptide
AD	Alzheimer's disease
APP	Amyloid precursor protein
αS	α -Synuclein
Asp	Aspartate
ATP	Adenosine -5'-Triphosphate
B0	External magnetic field
CD	Circular dichroism
CK1	Casein Kinase1
DLB	Dementia with Lewy bodies
DLS	Dynamic light scattering
DNA	Deoxyribonucleic acid
DTT	Dithiothreitol
<i>E.coli</i>	<i>Escherichia coli</i>
EDTA	Ethylenediamine tetraacetic acid
TEM	Transmission electron microscopy
Glu	Glutamate
HEPES	2-(4-(2-hydroxyethyl)1-piperazinyl) ethansulfonic
HMQC	Heteronuclear multiple quantum coherence
HPLC	High performance liquid chromatography
HSQC	Heteronuclear single quantum coherence
im-HSQC	Intensity modulated HSQC

INEPT	Insensitive nuclei enhanced by polarization transfer
IPAP	In-Phase-Anti-Phase
IPTG	Isopropyl- β -D-thiogalactopyranoside
$^3J_{H^N H^\alpha}$	Three bond H^N - H^α scalar coupling
kDa	kilo-Dalton ($=10^3$ g/mol)
LB	Luria Bertani
LBs	Lewy bodies
ml	Milliliter
ms	Milliseconds
μl	Microliter
μs	Microseconds
MS	Mass spectrometry
MTSL	(1-oxy-2,2,5,5-tetramethyl-D-pyrroline-3-methyl) methanethiosulfonate
MWCO	molecular weight cutoff
NAC	Non-A β Component of Alzheimer's disease amyloid plaques
NMR	Nuclear magnetic resonance
NOE	Nuclear Overhauser effect
NOESY	Nuclear Overhauser effect spectroscopy
ns	Nanoseconds
OD	Optical density
PCR	Polymerase chain reaction
PDB	Protein data bank
PD	Parkinson's disease

PFG-NMR	Pulse field gradient-NMR
PG-SLED	Pulse gradient stimulated echo longitudinal encode-decode
PMSF	Phenylmethylsulfonyl fluoride
PRE	Paramagnetic relaxation enhancement
PrP	Prion protein
ps	Picoseconds
R₁	Longitudinal or spin-lattice relaxation rate
R_{1ρ}	Longitudinal relaxation rate in rotating frame
R₂	Transversal or spin-spin relaxation rate
R_H	Hydrodynamic radius
SAXS	Small angle X-ray scattering
Ser	Serine
SDS	Sodium Dodecyl Sulfate
SDS-PAGE	SDS-polyacrylamide gel electrophoresis
T₁	Longitudinal or spin-lattice relaxation time
T_{1ρ}	Longitudinal relaxation time in rotating frame
T₂	Transversal or spin-spin relaxation time
TEMED	N,N,N',N'-tetramethylethylenediamine
TFA	Trifluoroacetic acid
Thr	Threonine
ThT	Thioflavin-T
Tris	Tris (hydroxymethyl)-amino-methane
τ	Correlation time for the electron-nuclear interaction
wt	Wild type

1. Introduction

1.1. Protein folding, misfolding and amyloid disease

A protein is created by ribosomes that "read" mRNA that is encoded by codons in the gene and assemble the requisite amino acid combination from the genetic instruction, in a process known as translation ^[1]. Once this post-translational modification process has been completed, the protein begins to fold, curling up on itself so that hydrophobic elements of the protein are buried deep inside the structure and hydrophilic elements end up on the outside ^[2]. Organisms have evolved such as the native states of proteins are required to perform diverse biochemical functions, ranging from mere pillars of the overall cellular architecture, like actins and tubulin, up to exquisitely complex molecular machines, as the DNA and RNA polymerases. In all cases adopting a proper structure is essential if the proteins are to carry out their biological function. Failing to do so has often critical consequences for cellular homeostasis ^[3].

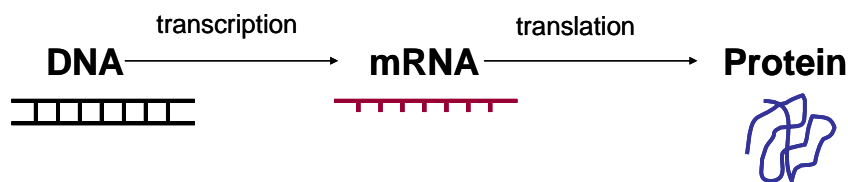


Figure 1.1: The flow of protein synthesis from gene ^[1].

Protein folding is one of the most crucial steps during the life of a protein. Generally, any kind of protein allowed only one folding pathway, called the native state; the most stable folding stage for molecules. A malfunction in achieving the native

conformation, render the polypeptide totally inactive, or worse, it can produce a misfolded molecule that can interfere with or block components of the cellular machinery to the point of causing cell malfunction or death^[3]. Nevertheless the fold of a protein appears to be solely encoded in the primary amino acid sequence, in as much as polypeptide chains fold *in vitro* in the absence of any auxiliary factors^[4, 5]. Indeed, the self assembling capability of proteins has allowed the occurrence of the early biologically-driven chemical processes, and the stability of such catalytically competent polypeptide-based systems is believed to have been crucial for evolution to take place.

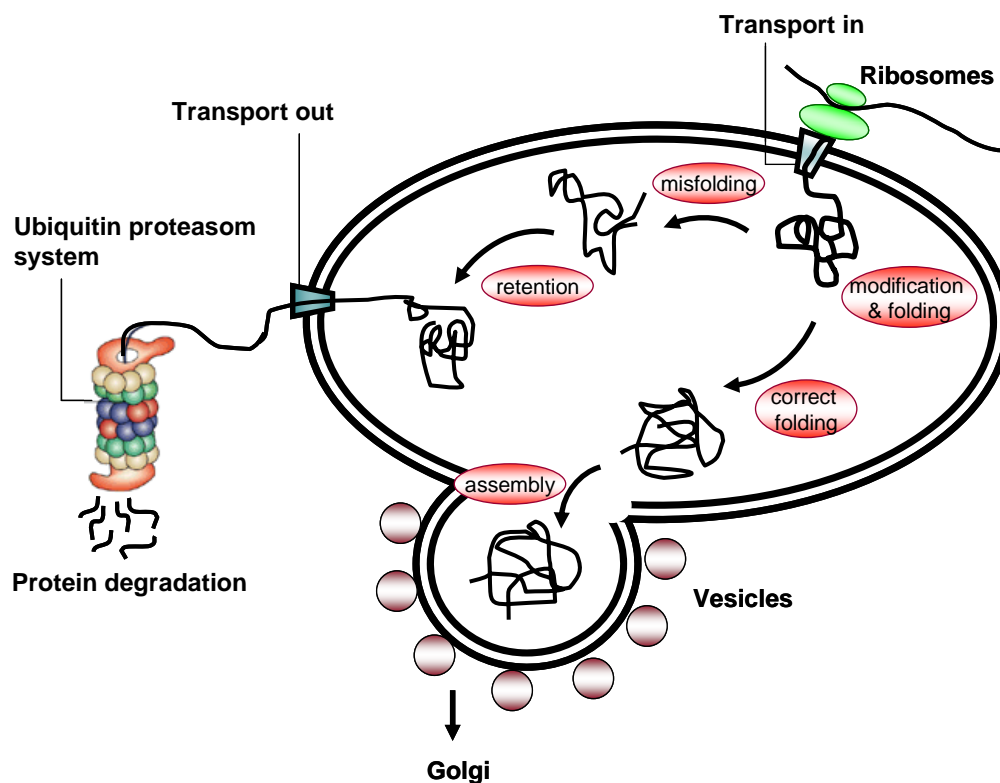


Figure 1.2: Correctly folded proteins are then transported to the Golgi complex and then delivered to the extracellular environment. However, incorrectly folded proteins are detected by a quality-control mechanism and sent along another pathway (the unfolded protein response) in which they are ubiquitinated and then degraded in the cytoplasm by proteasomes. Adapted from Dobson *et al.*^[3].

An unbiased search for the most stable structure of a protein would demand the population of all possible conformations that the polypeptide chain could adopt, until the state with the lowest energy is attained. Several models have emerged to explain the existence of folding pathways, from the framework model according to which secondary structure forms locally by collision of the folded segments, to the nucleation model in which folding is initiated locally and propagated through the chain. A third model is the hydrophobic collapse model that the polypeptide would collapse rapidly around its hydrophobic side chains and rearrange from the restricted conformational space ^[6]. The fact that three models are reasonable and fit experimental data, suggest that a single generic mechanism for protein folding may not exist in nature. The population of a defined secondary structure requires that many residues concomitantly adopt concerted backbone conformations capable of forming hydrogen bonds between amide and carbonyl groups of the main chain, which further reduced the degree of freedom of the system. In many cases, depending on the mechanism by which the protein folds, a relatively stable transition state is populated, which adopts an overall three-dimensional shape that closely resembles one of the native state of the protein ^[7].

In a folding energy landscape, as schematized on Figure 1.3, at the high energy, a multitude of unfolded conformations is present. 'Funnelling' on a rugged energy surface occurs towards the natively folded state by a rapid intramolecular contact formation ^[8]. By a nucleation process and subsequent autocatalytic aggregation reaction of partially unfolded structures, formation of aggregates and amyloid fibrils through intermolecular contact may occur and the system enters the aggregation funnel. Within the aggregation funnel, loosely packed oligomeric or amorphous aggregates as well as

different amyloid fibrillar states with different packing properties and with deep energy minima may form, thus exhibiting conformational polymorphism.

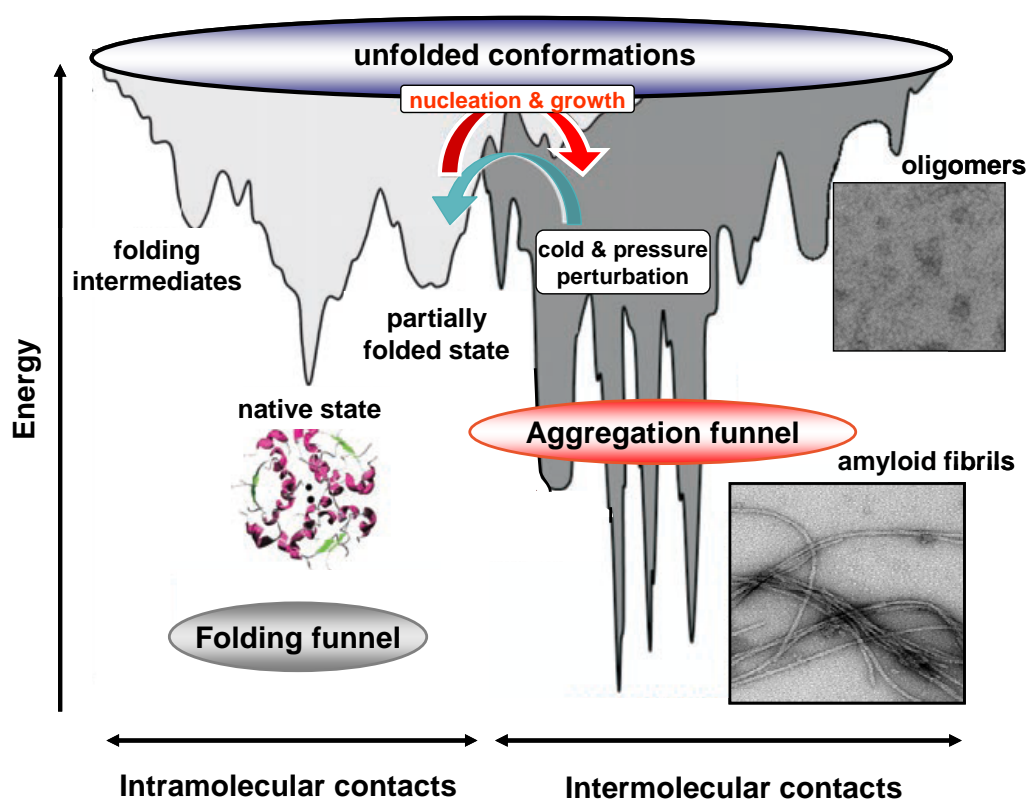


Figure 1.3: Schematic energy landscape for protein folding and aggregation funnel. While the protein attains the native conformation at its global energy minimum under normal physiological conditions, the amyloidogenic stacking of many protein molecules may lead to lower energies beyond this level in the aggregation funnel^[8, 9]. At low temperature and high pressure, dissociation of less densely packed protein aggregates and fibrils is possible. Figure adapted from Mishra *et al.*^[10].

In recent years, it has become evident that a wide range of human diseases are associated with aberrations in the folding process^[3, 11]. The transient formation of protofibrils has been observed during the *in vitro* fibrillization of all amyloid-forming proteins studied so far, irrespective of whether these proteins are linked to human disease. These diseases include Alzheimer's disease (AD, responsible protein: A β and

tau), Parkinson’s disease (PD, α -synuclein), prion protein related encephalopathies and type II diabetes mellitus (islet amyloid polypeptide). A sub-set of these pathologies, including AD, PD, Prion diseases (PrP) and late-onset diabetes, among others, are associated with the deposition of structurally defined protein aggregates in the tissue known as amyloid fibrils [12, 13]. Amyloid in disease is generally defined to be extracellular, although intracellular structures sharing the same core structures are described in PD [12]. Indeed, a huge variety of previously unrelated diseases share the feature of misfolded and aggregated protein deposits (Fig.1.4). These disease-causing proteins have various three dimensional folds with nothing in common in terms of sequences, but instead converge in a unique fibrillar structure called “amyloids” [14].

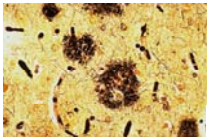
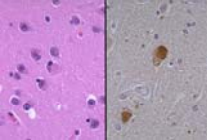
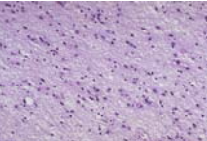
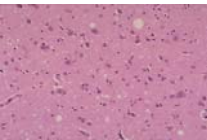
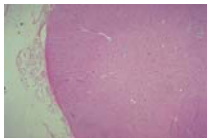
Disease	Protein	site of folding	Pathology
Alzheimer’s disease	Amyloid β -peptide/ Tau	ER	
Parkinson’s disease	α -synuclein	Cytosol	
Huntington’s disease	Huntingtin	Cytosol	
Creutzfeldt-Jakob disease	Prion protein	ER	
Amyot. Lateral sclerosis	Cu, Zn, superoxide dismutase	Cytosol	

Figure 1.4: Representative protein folding disease. Human diseases characterized by progressive misfolding and aggregation of proteins (Figures reproduced from internet pathology laboratory for medical education, Florida state university college of medicine, USA).

1.1.1. Fibrillization and structure of amyloid fibrils

Amyloid formation is a complex process and proceeds through a series of discrete β -sheet-rich oligomeric intermediates that appear before formation of fibrils and disappear upon fibril formation *in vitro*.

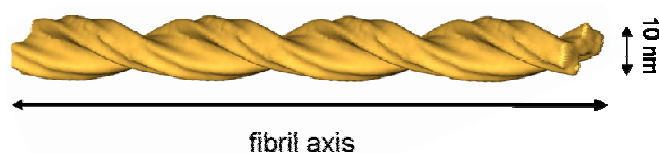


Figure 1.5: Computer generated molecular model of α -synuclein fibrils.

Fibrillization of many proteins is controlled by two kinetic parameters: the nucleation rate and the elongation rate. A kinetic theory of fibrillogenesis was established which relates the concentration of the amyloidogenic protein and the rate of fibrillogenesis^[15]. The time gap before the seed formation and beginning of rapid aggregation called the lag time is very dependent on sample conditions and may range from minutes to days^[16, 17]. All amyloid fibrils are ordered in secondary structures, including a core cross β -sheet structure, in which continuous β sheets are formed with beta strands running perpendicular to the fibril axis^[11]. And these amyloid fibrils consist of two to six unbranched protofilaments associated laterally or twisted together to form fibrils that are approximately 10 nm diameter (Fig.1.5). Once formed the rigid structure of amyloid fibrils, and the deep energy minima acquired to form those structures are extremely stable and hard to solubilize^[18].

The first phase in amyloid formation seems to involve the formation of soluble oligomers. The earliest species visible by electron microscopy generally resemble small, bead-like structures. These early preformed aggregates then transform into species with

more distinctive morphologies, often called protofibrils. These structures are commonly short, thin, sometimes curly, fibrillar species that are thought to assemble into mature fibrils, perhaps by association accompanied by some degree of structural reorganization. Interestingly, several amyloid proteins form pore-like structures in solution in the absence of membrane. In some cases, the propensity of the protein to form pore-like structures correlates very well with its ability to permeabilize membranes [19, 20] (Fig.1.6).

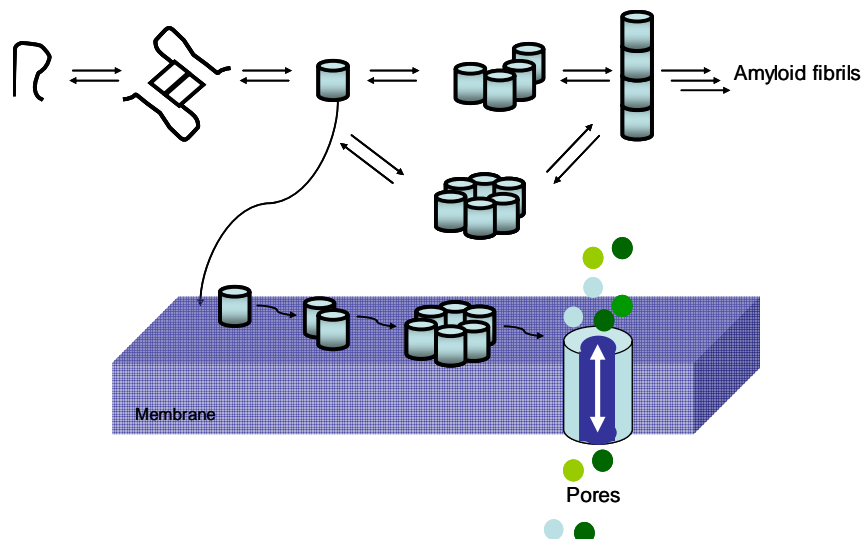


Figure 1.6: Pore formation by amyloid-forming proteins may occur by one of several mechanisms similar to those used by evolved pore-forming protein toxin. The mechanism of pore formation by pore-forming toxin includes a series of complex events involving binding to the membrane, oligomerization, and insertion into the membrane. Picture adapted from Lashuel *et al.* [20].

1.1.2. α -synuclein aggregation related to Parkinson's disease (PD)

PD is the second most common neurodegenerative disorder after AD [21]. It arises from the loss of dopaminergic neurons in the *substantia nigra* pars compacta of the brain and is accompanied by the presence of eosinophilic intracellular inclusions

known as Lewy bodies (LBs) and Lewy neurites, which are confined largely to nerve cells [22]. Ultrastructurally, LBs are protein rich depositions in the form of long amyloid-like fibrils, the major component of which is the pre-synaptic protein α S [23]. LBs are also found in other major neurodegenerative disorders that occur increasingly with aging, including dementia with LBs and AD [24].

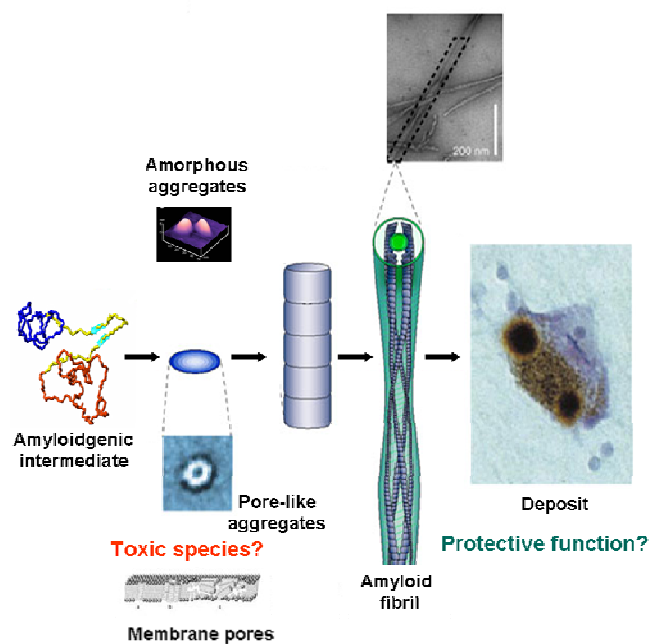


Figure 1.7: A schematic representation of the general mechanism of aggregation to form amyloid fibrils. Protofibrils or protofilaments, mature fibrils, accumulate in plaques or other structures such as the Lewy bodies associated with PD's disease. Some of the early aggregates seem to be amorphous or micellar in nature. Picture adapted from Dobson *et al.* [3].

PD is primarily a sporadic disorder, more than 10 different loci are responsible for rare Mendelian forms of PD, and the study of these gene products has provided new insights that has assisted experimental models of neurodegeneration [24]. α S has been unequivocally linked to PD due to the discovery of genetic mutations. Three different mutations in the α S gene result in early onset of PD (A30P, E46K and A53T), and

additionally, a locus triplication causing an increased dosage of the wild type (wt) α S gene potentiates the disease [25-28]. The role of α S in the formation of LBs and the pathogenesis of PD has been compared to the role of A β peptide and amyloid plaques in Alzheimer's disease. The appealing hypothesis for LBs formation is that α S monomers combine to form oligomers (or protofibrils), which coalesce into fibrils and then co-aggregate with other proteins into Lewy body inclusions [29, 30]. While the monomers and oligomers of α S are soluble, the fibrils and LBs are insoluble in the neuronal cytoplasm. However, the roles of the various physical forms of α S in PD pathogenesis are controversial. LBs have been proposed to be both neurotoxic [31, 32], and protective [33, 34]. Other hypotheses state that the protofibrillar intermediates, made of α S oligomers, are the main species toxic to dopaminergic neurons [29].

1.2. Cold dissociation

Denaturation of protein results in a loss of secondary and tertiary structure, although the peptide bonds between the amino acids are left intact. In contrast to intrinsically unstructured proteins, which are unfolded in their native state, but still functionally active, denatured proteins lose their ability to function. Denatured proteins can exhibit a wide range of characteristics, from loss of solubility to communal aggregation. In practice, the stability of a protein will depend strongly on solution conditions such as pH, the presence of chemical denaturants or co-solutes. Chemical denaturants interfere with stabilizing intra-molecular interactions mediated by non-covalent forces such as hydrogen bonds, Van der Waals forces, and hydrophobic effects. The addition of co-solutes or cosolvents can have a large effect on the volume change,

and Scharnagl *et al.* have recently given a comprehensive thermodynamic description of the effect of co-solutes and co-solvents on the stability of the protein ^[35].

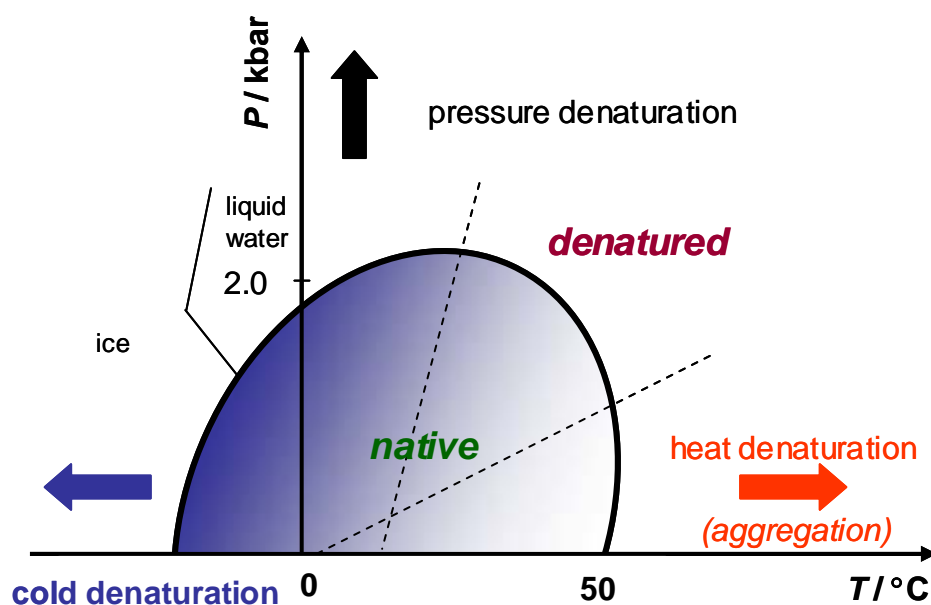


Figure 1.8: Schematic of the pressure-temperature phase diagram of a protein. The boundary of the ellipse is given by $\Delta G=0$, heat denaturation: ΔV and ΔS are positive, denatured: ΔV is negative and ΔS is positive and pressure denaturation: both ΔV and ΔS are negative ^[9]. The region of the cold denaturation is indicated by blue arrow. The different routes of unfolding of the native protein as well as the corresponding thermodynamic properties are depicted. Heat denaturation is often accompanied by irreversible aggregation. The water/ice phase-transition line is also given. Adapted from Mishra *et al* ^[10].

It is well known that proteins can also be unfolded by cooling (called cold denaturation) ^[36]. Comparatively little structural characterization has been applied to these states although a number of detailed thermodynamic studies have been reported ^[36, 37]. In particular, it is not known how compact these states are and how their hydrodynamic properties compare to other unfolded states. The phenomenon of protein cold denaturation has been known for several decades and the existence of such a cold-

denatured state is predicted by Gibbs-Helmholtz equation. Theoretically, cold denaturation should be a universal property for all proteins, reflecting interaction between water and protein molecules. The thermodynamic stability of a protein is an energy landscape as a multidimensional function of temperature, pressure, and solution conditions. When the solution conditions (pH value, ionic strength, salt and cosolvents concentration) are kept constant, the stability of the protein is a function of only temperature (T) and pressure (p)^[10]. The transition line, where the protein unfolds upon a temperature or pressure change, is given by the Gibbs free energy of unfolding ($\Delta_u G$) = 0. The physically relevant solution of the curve in the p, T plane has an elliptical shape (Fig.1.8), calculated from a second-order expansion of the Gibbs energy change of unfolding, assuming a simple native \leftrightarrow unfolded (denatured) equilibrium behavior^[9].

According to the stability diagram shown in Figure 1.8, the possibility to explore the temperature region below 0 °C at slightly elevated pressure can be used to study the cold denaturation process of protein. At low temperatures, a marked decrease of the hydration enthalpy term ΔH_{hydr} (in the hydration shell owing to exposure of formerly buried residues, $\Delta H_u = \Delta H_{\text{conf}} + \Delta H_{\text{hydr}}$) leads to the destabilization of the native structure^[38]. Thus, with the enthalpy change of unfolding being a function of temperature, at a low enough temperature, the Gibbs free energy of unfolding ($\Delta_u G$) becomes negative and the protein will unfold under the release of heat. Usually, the transition temperatures for the cold denaturation is well below 0 °C, so that high pressure has to be applied to keep the water in the liquid state, or freezing of cold water has to be avoided using supercooling techniques and small sample volumes^[39, 40]. There have been several attempts to reach the cold denatured state without strongly perturbing the

environment, in the presence of denaturants ^[36], mutations ^[41], supercooled proteins encapsulated in micelles ^[42] and supercooling with very thin capillaries ^[39]. In this thesis, it is proved that the transition temperatures for the cold denaturation lie well below 0 °C, freezing of cold water be avoided using supercooling techniques and small sample volumes ^[40].

1.3. NMR spectroscopy

NMR is a widely used spectroscopic method today for purposes ranging from geological measurements to medical imaging and bimolecular dynamics. In 1946 two groups independent of each other performed both solid-state and solution-state NMR experiments ^[43, 44]. Today the magnetic fields are significantly higher than in 1946 and 800-900 MHz magnets are not uncommon. The methods used to study biological molecules have an increasing complexity and have developed from continuous wave 1D methods to Fourier transformed pulsed heteronuclear multidimensional experiments. One important application of biological NMR is structure determination, but also dynamical properties, such as local mobility and hydrodynamics are within reach of NMR. In this thesis NMR has been used to obtain a detailed insight to understand the mechanism of amyloid precursor α S using diffusion measurements to clarify the size of various ensemble, relaxation measurements, paramagnetic relaxation enhancement (PRE) for the intermolecular distance information and chemical shifts for the backbone secondary structure information. Some structural properties of the protein are also studied using measurements of J -coupling. A brief introduction to NMR parameters used for biomolecules is given below.

1.3.1. J -couplings

J -couplings, or indirect couplings, arise through the coupling of two neighboring spins through covalent bonds. The indirect spin-spin coupling gives rise to a splitting of the signal due to polarization of the spins and altered orbital motion of the valence electrons. One and two-bond scalar coupling (1J , 2J) are heavily used in heteronuclear solution-state NMR to transfer the magnetization in multidimensional experiments ^[45].

The J -coupling is most often measurable up to 3-bonds separation, and is not dependent on the magnetic field. The 3-bond, 3J , couplings carry information on the structure of the molecule and are dependent on the dihedral angle between the spins. This relation can be parameterized and this was done by Karplus^[46] using the empirical relation (1). Here A , B and C are constants that are dependent on the molecular system and ϕ is the dihedral angle.

$$J(\phi) = A \cos^2 \phi + B \cos \phi + C \quad (1)$$

The protein secondary structure can be predicted directly from the ${}^3J(\text{H}^{\text{N}}\text{H}^{\alpha})$ coupling constant by calculating the difference between the experimental coupling constant and the random coil value^[47].

1.3.2. Chemical shift

NMR chemical shifts, especially of ${}^{13}\text{C}^{\alpha}$ and ${}^{13}\text{C}'$ atoms, are very sensitive probes of secondary structure in proteins^[48]. Relative to random coil chemical shifts ${}^{13}\text{C}^{\alpha}$ and ${}^{13}\text{C}'$ resonances tend to shift upfield in β -strands and extended sheets and downfield in helices. Therefore, secondary structure elements can be identified by subtracting random coil values (δC_{coil}) from the experimental chemical shifts (δC_{exp}). The secondary chemical shift ($\Delta\delta C$) is defined as the difference between δC_{exp} and δC_{coil} are used for the secondary structure determination on a given sequence. In this notation, negative secondary chemical shifts indicate β -strand and positive values indicate α -helix.

$$\Delta\delta C = \delta C_{\text{exp.}} - \delta C_{\text{coil}} \quad (2)$$

1.3.3. Nuclear Overhauser effect (NOE)

NOE is a through-space spin-spin (inter-nuclear) interaction and is dependant on

an inter-nuclear distance (r), as well as on the rotational correlation time τ_c (describing the Brownian tumbling motion of the protein in solution), and inversely proportional to the sixth power of the distance between the dipoles under solution condition. Using a first-order approximation, the NOE cross-peak intensities or volume V is proportional to the relaxation rates and may be expressed as ^[49]:

$$V = r^{-6} f(\tau_c) \quad (3)$$

NOE is detectable when the two spins are close ($\sim 5 \text{ \AA}$) in space, and this makes NOE exceptionally useful for spatial proximity. By measuring cross-peak intensities V , distance restraints can be derived. It can be estimated in the 2D and 3D NOESY spectra. Proton-proton NOEs are the most widely used parameter for the structure determination by NMR ^[50].

1.3.4. Paramagnetic relaxation enhancement (PRE)

Distance restraints between residues in the denatured state of proteins can be obtained by covalently attaching a probe containing a free radical to a unique cysteine residue introduced by mutagenesis. The magnetic interaction between the unpaired electron in the spin label and a proton in the same molecule is similar to the Nuclear Overhauser Effect (NOE) between pairs of protons. Broadening effects of the unpaired electron in spin label can be observed up to 20-25 \AA ^[51]. The enhanced relaxation rate R_{2P} is inversely proportional to the distance between the electron and the nuclear spins r ^[51]:

$$R_{2P} = \frac{K}{r^6} \left(4\tau_c + \frac{3\tau_c}{1 + \omega^2\tau_c^2} \right) \quad (4)$$

where τ_c is the correlation time for this electron-nuclear interaction, ω is the Lamor frequency of the nuclear spin (proton). K is composed of the physical constants:

$$K = \frac{1}{15} S(S+1) \gamma^2 g^2 \beta^2 \quad (5)$$

in which γ is the nuclear gyromagnetic ratio, g is the electronic g factor and β is the Bohr magneton. Overall K is $1.23 \times 10^{-32} \text{cm}^6 \text{s}^{-2}$ [52].

The peak intensity ratio ($I_{\text{para}}/I_{\text{dia}}$) of the corresponding ^{15}N - ^1H crosspeak can be converted in the paramagnetic transverse relaxation rate enhancement (R_{2p}) [51] by estimating the additional relaxation needed to reduce the peak intensity in the diamagnetic case to the intensity observed in the paramagnetic case:

$$\frac{I_{\text{para}}}{I_{\text{dia}}} = \frac{R_2 e^{-R_{2p} t_{\text{inept}}}}{R_2 + R_{2p}} \quad (6)$$

where R_2 is the transverse relaxation rate of the amide proton without spin label, R_{2p} is the transverse relaxation rate of the amide proton with spin label. $I_{\text{para}} / I_{\text{dia}}$ is the intensity ratio for an amide cross peak between with spin label and without spin label, t is the duration of INEPT delays (~ 10 ms) in HSQC pulse sequence. The distance (r) can be extracted from above two equations and has been used for the generation of the αS structural ensemble [53].

1.3.5. Diffusion ordered spectroscopy (DOSY)

Translational diffusion and relaxation are the two important parameters in dealing with dynamic systems like protein-protein interactions and protein movements in various time scales. Translational diffusion is defined as translational motion in the

absence of a concentration gradient. Stejskal *et al.* showed that the diffusion coefficient of molecules in solution can be measured using pulse field gradient (PFG) NMR methods ^[54]. PFG techniques are used extensively to measure translational diffusion in solution ^[55]. Due to diffusion, molecules will change their spatial localization between the application of the first and second gradient, and thus they will experience an inhomogeneous total field, causing an attenuation of the measured signal. For unrestricted diffusion of a molecule in an isotropic liquid, the PFG NMR signal amplitude, A , normalized to the signal obtained in the absence of gradient pulses, is related to the diffusion coefficient D by

$$A = e^{-(r^2 \delta^2 D (\Delta - \delta/3) \times g^2)} \quad (7)$$

here γ is the gyromagnetic ratio of the observed nucleus, g and δ are the magnitude and duration of the magnetic field pulses, and Δ is the time between the gradient pulses ^[54]. The determination of D is achieved by acquiring a series of 16 one-dimensional PFG spectra at different gradient strengths and fitting the decay of the signal intensity to a Gaussian function with the form

$$I_{(g)} = a \times e^{-d_D \times g^2} \quad (8)$$

where $I_{(g)}$ is the ratio between the intensity of the signal measured at gradient strength g and in the absence of gradient, and a is the pre-exponential factor (~ 1). The Stokes-Einstein equation relates D to the hydrodynamic radius, R_H , as follows:

$$D = \frac{kT}{6\pi\eta R_H} \quad (9)$$

where k is the Boltzmann constant, T is the temperature of the sample and η is the viscosity of the solution. Thus determination of the R_H of a polypeptide chain requires the determination of the viscosity of the solution. In order to overcome this, a viscosity probe of known size is included in the determination, usually dioxane ^[56, 57], providing the relationship:

$$R_H^{prot} = \frac{D_{ref}}{D_{prot}} R_H^{ref} \quad (10)$$

The intensities decay as a function of gradient strength was fitted with a single Gaussian curve with decay rate. The observed decay rate, for protein d_{prot} , and for reference d_{ref} , is proportional to the diffusion coefficient (D) of each molecule. Combined with the known hydrodynamic radius of the reference (R_H^{ref}), the hydrodynamic radius of the protein (R_H^{prot}) can be calculated as follows:

$$R_H^{prot} = \frac{d_D^{ref}}{d_D^{prot}} R_H^{ref} \quad (11)$$

2. Materials and methods

2.1. Materials

2.1.1. Chemical reagents and enzymes

During the development of the present thesis work the following reagents from the mentioned suppliers summarized in Table 2.1 were used.

Table 2.1: Chemical reagents and enzymes

Chemicals/Enzymes	Company
Agar, DNaseI, IPTG, Streptomycine	AppliChem, Darmstadt, Germany
Ammonium chloride (>98 % ¹⁵ N)	Cambridge Isotope Laboratories, Andover, USA
¹³ C-D-glucose (>98 % ¹³ C)	Spectra Stable Isotopes, Columbia, USA
BamHI, CIAP, _HindIII, NcoI, NdeI, X174DNA/BsuRI(HaeIII), T4-DNA ligase	Fermentas, St. Leon-Rot, Germany
Ammonium molybdate tetrahydrate, ascorbic acid, Coomassie Brill-lant Blue R-250, Copper chloride dihydrate, Iron (II) sulfate hep-tahydrate	Fluka, Neu-Ulm, Germany
DTT	Gerbu, Gaiberg, Germany
Agarose	GibcoBRL, Karlsruhe, Germany
Ficoll 400	ICN Biomedicals Inc, Costa Mesa, USA
Bench Mark protein ladder	Invitrogen, Karlsruhe, Germany
Acetic acid, α-D(+)-glucose monohydrate, Ammonium sulfate, Ammonium chloride, Ammonium hydrocarbonate, Boric acid, Disodium hydrogen phosphate, Ethanol, Glycerol, Glycine, Hydrochloric acid, Manganese chloride dihydrate, Magnesium sulfate heptahydrate, Sodium chloride, Sodium dihydrogen phosphate, Sodium hydroxide, TFA, Thiaminechloride hydrochloride, Tris, Urea	Merck, Darmstadt, Germany
Casein Kinase I (CKI)	New England Biolabs, Ipswich, USA
Hot Star Taq, Ni-NTA Agarose, QIAGEN Plasmid Midi Kit, QI-Aprep Spin Miniprep Kit,	Qiagen, Hilden, Germany
Cobalt chloride hexahydrate	Riedel-de Haën, Seelze, Germany
Complete TM protease inhibitors, Complete TM EDTA-free, Elastase, Protease K, Trypsin	Protease inhibitors Roche Diagnostics, Mannheim, Germany
Acetonitrile, Ampicillin sodium salt, APS, Dipotassium hydrogen phosphate, Ethidium bromide, EDTA, HEPES, Imidazole, Magnesium chloride hexahydrate, MES, MOPS, Potassium dihydrogen phosphate, Rotiphorese Gel 30, Sodium acetate, TEMED, Tryptone, Yeast extract	Roth, Karlsruhe, Germany
SDS	Serva, Heidelberg, Germany
Turbo Pfu DNA polymerase, dNTP	Stratagene, La Jolla, USA
MTSL	Toronto Research Chemicals, Toronto, Canada
Ready Gel@ precast gels (20 %, 15 %)	BioRad, California, USA

2. Materials and methods

Purified Mouse Anti- α -synuclein (BD)	BD Biosciences, Heidelberg, Germany
Rabbit anti-amyloid oligomer polyclonal antibody (A11)	Invitrogen, Biosource, Europe, S.A

2.1.2. Bacterial strains

-*Escherichia coli* BL21 (DE 3). F-, *ompT*, *hsdS* β (r β -m β -), *dcm*, *gal*, (DE3) tonA.

-*Escherichia coli* XL1-Blue. *recA1 endA1 gyrA96 thi-1 hsdR17 supE44 relA1 lac* [F'proAB lacIqZ M15Tn10 (Tetr)] (Stratagene).

2.1.3. Oligonucleotide primers for mutagenesis of α -synuclein

The coding sequences for wt human α S was kindly provided by Dr. Peter Lansbury, Harvard Medical School, Cambridge, MA. This construct was cloned *NdeI/EcoRI* in the plasmid PT7.7 under the string promoter T7.

Table 2.2: DNA primers employed for the construction of Cys-containing mutants

Y136 (TAC→TAT) F 5' GGAAGGGTATCAAGACTATGAACCTGAAGCCTAAG 3'
Y136 (TAC→TAT) R 5' CTTAGGCTTCAGGTTTCATAGTCTTGATACCCTTCC 3'
S87A F 5'GTGGAGGGAGCAGGGGCGATTGCAGCAGCCACTGG 3'
S87A R 5'CCAGTGGCTGCTGCAATCGCCCCCTGCTCCCTCCAC 3'
S87D F 5'GTGGAGGGAGCAGGGGATATTGCAGCAGCCACTGG 3'
S87D R 5'CCAGTGGCTGCTGCAATATCCCCTGCTCCCTCCAC 3'
S87E F 5'GTGGAGGGAGCAGGGGAAATTGCAGCAGCCACTGG 3'
S87E R 5'CCAGTGGCTGCTGCAATTTCCCCTGCTCCCTCCAC 3'
A18C F 5' GGAGGGAGTTGTGGCTTGCCTGAGAAAACCAAACAGG 3'
A18C R 5' CCTGTTTGGTTTTCTCAGCGCAAGCCACAACCTTCCTCC 3'
A90C F 5' CAGGGAGCATTGCATGCGCCACTGGCTTTGTC 3'
A90C R 5' GACAAAGCCAGTGGCGCATGCAATGCTCCCTG 3'
A140C F 5' GACTACGAACCTGAATGCTAAGAAATATCTTTG 3'
A140C R 5' CAAAGATATTCTTAGCATTTCAGGTTTCGTAGTC 3'
S129A F 5' GGCTTATGAAATGCCTGCGGAGGAAGGGTATCAAG 3'
S129A R 5' CTTGATACCCTTCCTCCGCAGGCATTTTCATAAGCC 3'
S129D F 5' GGCTTATGAAATGCCTGATGAGGAAGGGTATCAAG 3'
S129D R 5' CTTGATACCCTTCCTCATCAGGCATTTTCATAAGCC 3'

The protein α S mutants were cloned by Pinar Karpinar. Sequence of DNA primers forward (F) and reverse (R) employed for the construction of the Cys-containing mutants in Y136 codon mutated α S shown in Table 2.2. The ‘TAC’ codon in Y136 in wt α S was mutated into ‘TAT’ to prevent the misreading of cysteine [58]. In order to provide an attachment site for the nitroxide spin label employed in PRE studies, three different α S cysteine containing mutants A18C, A90C and A140C were constructed on the Y136 (TAT) mutated wt protein. To study the phosphorylation effect of wt α S four different mutants S87A, S87D, S129A and S129E were constructed using the Quick Change site directed mutagenesis kit.

2.1.4. Equipments

Laboratory instruments and consumables are summarized in Table 2.3.

Table 2.3: Instruments

Common Name	Identifier/Company
Balances	Sartorius B 3100 S, Sartorius, Göttingen, Germany Sartorius AC 210 S, Sartorius, Göttingen, Germany
Centrifuges	Beckmann-Coulter Avanti J-20 and J-301, rotors: JLA 8.100, JLA 9.100, JLA 16.250, JA 25.50 Ti, JA 30.50 Ti, Krefeld, Germany Eppendorf Centrifuge 5415D, Wesseling-Berzdorf, Germany Eppendorf Centrifuge 5804, Wesseling-Berzdorf, Germany Heraeus Biofuge primo, Kendro, Hanau, Germany
Concentrators	Microcon, YM-3 and YM-10, Amicon, Bedford, USA Centricon, YM-3 and YM-10, Amicon, Bedford, USA Centriplus, YM-3 and YM-10, Amicon, Bedford, USA Vivaspin 2 ml MWCO 10.000 PES, Vivascience, Hannover, Germany
Desalting	NAPT M -10, Amersham Pharmacia Biotech, Freiburg, Germany PDT M -10, Amersham Pharmacia Biotech, Freiburg, Germany
Dialysis	Slide-A-Lyzer Dialysis Cassettes, MWCO 3500, 0.1-0.5 ml Capacity, Pierce Biotechnology, Inc., Rockford, IL, USA Slide-A-Lyzer Dialysis Cassettes, MWCO 10000, 0.1-0.5 ml Capacity, Pierce Biotechnology, Inc., Rockford, IL, USA Spectra Por membranes, MWCO 10000, Roth, Karlsruhe, Germany Spectra Por membranes, MWCO 3500, Roth, Karlsruhe, Germany
Electrophoresis	Kodak Electrophoresis documentation and analysis system 120, Eastman Kodak Co., New York, NY, USA Power Pac 300, BioRad, München, Germany Polyacrylamide gel electrophoresis: Mini-PROTEAN 3 Cell, BioRad, München, Germany Agarose gel electrophoresis: Mini-Sub Cell GT, BioRad, München, Germany

2. Materials and methods

-80°C freezer	MDF-U71V Ultra-low temperature freezer, SANYO Electric Co., Ltd, Osaka, Japan
Filtering	Sterile filter 0,20 µm, Sartorius, Göttingen, Germany
FPLC	Äkta prime, Amersham Pharmacia Biotech, Freiburg, Germany Äkta basic, Amersham Pharmacia Biotech, Freiburg, Germany HiTrap™ SP XL, Amersham Pharmacia Biotech, Freiburg, Germany
HPLC	System 1: UV-975, PU-980, LG-980-02, DG-980-50, AS-2055Plus, CO-200, JASCO International, Groß-Umstadt, Germany System 2: MD-910, PU-980, LG-1580-04, DG-1580-54, AS-950-10, CO-200, JASCO International, Groß-Umstadt, Germany System 3: MD-2010Plus, PU-2080Plus, LG-2080-04, DG-2080-54, AS-2055Plus, CO-200, JASCO International, Groß-Umstadt, Germany Vydac C18 10x250 mm, Hesperia, CA, USA Vydac C18 4.6x250 mm, Hesperia, CA, USA
Incubator	Infors Multitron HT, Einsbach, Germany Certomat R, B. Braun Biotech International, Melsungen, Germany
Lyophilisation	Christ Alpha 2-4, B. Braun Biotech International, Melsungen, Germany
NMR	AVANCE 400 MHz, Bruker, Karlsruhe, Germany AVANCE 600 MHz, with cryoprobe, z-axis, Bruker, Karlsruhe, Germany DRX 600 MHz, Bruker, Karlsruhe, Germany AVANCE 700 MHz, triple axis gradient, Bruker, Karlsruhe, Germany DRX 800 MHz, triple axis gradient, Bruker, Karlsruhe, Germany AVANCE 900 MHz, with cryoprobe, z-axis gradient, Bruker, Karlsruhe, Germany
NMR tube	Quality NMR Sample Tubes 5 mm, Norell, Inc., Landisville, NJ, USA Shigemi NMR tube 5 mm, Shigemi Corp., Tokyo, Japan Capillary NMR tube 0.1 mm OD, Willmed, USA
DLS	DynaPro DLS, Wyatt Technology Corporation, Santa Barbara, USA
CD	Chirascan spectrometer, Applied Photophysics Ltd, Leatherhead, UK
UV	Hewlett Packard 8453, HP, Canada

2.2. Methods

2.2.1. Molecular biology methods

2.2.1.1. Isolation of DNA

10 ml *E. coli* XL2-blue overnight cultures were used for purification of up to 20 µg plasmid DNA with the help of the QIAprep spin miniprep kit. Plasmid DNA was isolated from the cell pellets according to the manufacturer's instructions. For the removal of enzymes, salts and buffers, columns with a silica gel membrane (QIAquick spin columns) were used according to the manufacturer's instructions.

2.2.1.2. Site-directed mutagenesis of α -synuclein

Single site amino acid changes were generated using the QuikChange[®] site-directed mutagenesis kit (Stratagene). The 50 μ l PCR reaction mixtures contained 125 ng of each primer, 10 ng plasmid DNA template, 6.25 μ mol dNTPs and 2.5 units Turbo Pfu DNA polymerase in cloned Pfu buffer.

The cycling after an initial step at 95 °C for 30 s was performed as follows: I) denaturing for 30 s at 95 °C, II) annealing for 1 min at 60 °C and III) elongation for 5 min per kb of plasmid length at 68 °C. For creating single nucleotide changes and for creating double or triple nucleotide changes the number of cycles was 16. Following temperature cycling, 10 units of Dpn I restriction enzyme were directly added to each PCR reaction mixture and incubated for 1 h at 37 °C. 1 μ l of the reaction mix was transformed into *E. coli* XL1-blue for single site. The plasmid DNA was isolated and the desired mutation was confirmed by DNA sequencing.

2.2.1.3. DNA sequencing

Sequencing of purified plasmid DNA was performed via the extended Hot Shot DNA sequencing service of SeqLab (Göttingen, Germany) 200 μ l PCR tubes with a flat lid were loaded with a total volume of 7 μ l containing 20 pmol of primer and 0.6-0.7 μ g plasmid DNA.

2.2.1.4. Transformation of *E. coli*

1 μ l plasmid DNA was added to 50 μ l competent cells and incubated for 30 min on ice. Cells were subjected to a heat shock of 42 °C for 45 s and subsequently cooled for 2 min on ice. Afterwards, the cells were supplemented with 0.5 ml of 2 x YT

medium and incubated for 1 h at 37 °C. Finally, the cells were plated onto LB-agar plates containing ampicillin and incubated overnight at 37 °C.

2.2.2. Methods for protein biochemistry

2.2.2.1. Expression and purification of α -synuclein

The same protocol was applied ^[53] for purification of all the α S variants production. Following transformation, *E. coli* BL 21 cells were grown overnight in 10 ml of LB medium containing 100 μ g/ml ampicillin. The pre-culture was diluted (10 ml in 1 l LB containing 100 μ g/ml ampicillin) and allowed to grow at 37 °C until an optical density (OD) of 0.6-0.8. Expression of the desired gene construct was then induced with 1 mM IPTG. Cells were then harvested, after 3-4 hours of incubation at 37 °C, by centrifugation at 3000 x g for 10 minutes.

The bacterial pellet was resuspended in 10 ml of 10 mM Tris, pH 8.0, 1 mM EDTA and 1 mM PMSF, and lysed by multiple freeze-thaw cycles and sonication. The cell lysate was boiled for 20 minutes and centrifuged at 20000 x g (30 minutes at 4 °C), in order to precipitate the heat-sensitive proteins (synuclein remain soluble). Streptomycin-sulfate (Sigma) was added to the supernatant from the previous step (final concentration 10 mg/ml) for precipitation of DNA. The mixture was stirred at 4 °C for 15 minutes, followed by centrifugation at 20,000 g (30 minutes at 4 °C).

The synuclein protein was then precipitated by addition of ammonium sulfate (Merck, Darmstadt, Germany) (361 mg/ml) to the supernatant from previous centrifugation. The solution was stirred at 4 °C for 15 minutes and centrifuged once again at 20000 x g (30 minutes at 4 °C). The protein pellet was resuspended in 20 ml of 25 mM Tris, pH 7.7, and loaded onto a POROS8 anion exchange column in in ÄKTA

Basic system equilibrated with 25 mM Tris-HCl, pH 7.7. Full length α S and mutated proteins were eluted with a salt gradient at ~300 mM NaCl. The fractions containing protein (determined UV spectrophotometer) were pooled together and concentrated using Centriprep YM-10 filter devices (10 kDa molecular weight cut off) (Amicon, Bedford, MA) to a final concentration of 300 μ M. Concentrated proteins were dialyzed overnight against the desired buffer (50 mM Na-phosphate, pH 7.4, 100 mM NaCl). Purity of the protein was assessed by SDS-PAGE and the concentration was determined with absorbance at 275 nm using an extinction coefficient of 5600 M⁻¹cm⁻¹. Proteins were aliquoted, flash frozen in liquid N₂ and stored at -80 °C.

Purification of Cys-containing mutants was performed similarly to wt protein but 5 mM dithiothreitol (DTT) was included throughout the different purification steps in order to avoid Cys oxidation and disulfide-linked dimer formation. Preparation of ¹⁵N- and ¹³C/¹⁵N labeled proteins were carried out exactly as for the non-labeled proteins with the only difference that LB medium was replaced by M9 minimal medium supplemented with ¹⁵NH₄Cl or ¹⁵NH₄Cl and ¹³C-D-glucose. A 5x stock solution of M9 salts, with the absence of NH₄Cl, was prepared adding 64 g of Na₂HPO₄·7H₂O (Sigma), 15 g KH₂PO₄ (Sigma), 2.5 g NaCl (Sigma) and adding water to a final volume of 1 l followed by autoclaving. For 500 ml of final culture media, 100 ml of M9 5x stock solution was mixed with 1 ml of 1M MgSO₄, 50 μ l of 1 M CaCl₂, 0.5 g of ¹⁵NH₄Cl, 10 ml of 20 % D-glucose (¹³C-D-glucose for double labeled proteins) and autoclaved after making up to a final volume of 500 ml with ddH₂O. The pH of the solution was adjusted to 7.3 and the media was filter-sterilized (0.2 μ m filter). Prior to the start of incubation, 100 μ g/ml of ampicillin was added.

2.2.2.2. Site-directed spin-labelling of proteins

Studies of PRE by nitroxide spin labels involve the site-directed addition of a nitroxide radical in the evaluated position of the protein. In most commonly employed procedures, a unique sulfhydryl group is selectively modified with a nitroxide reagent. Single cysteine mutants for the attachment of a spin label were generated by site directed mutagenesis and modified with the thiol-specific nitroxide spin label reagent (Fig.2.1). A methanethiosulfonate-based nitroxide spin label can be efficiently coupled to the reduced sulfhydryl of the cysteine under physiological buffer conditions.

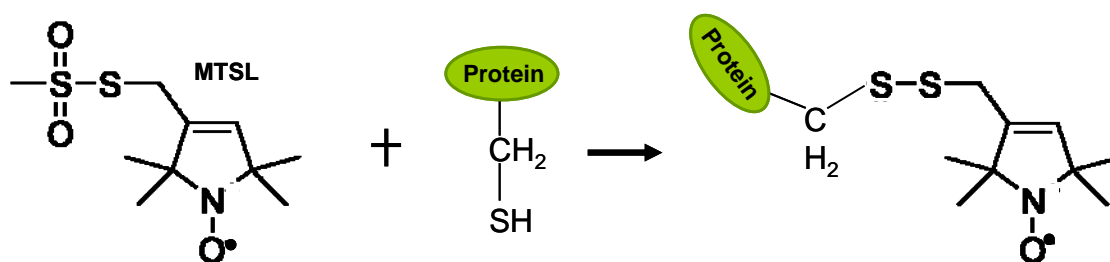


Figure 2.1: Reaction of the nitroxide-melamine MTSL with a Cys residue in the target protein. Chemical structure of the spin label reagent MTSL and the disulfide bond adduct formed with the side-chain of the single Cys residue in the protein.

The reaction of α S Cys-containing mutants (A18C, A140C and S87A-A18C) with the nitroxide spin label MTSL (1-oxo-2,2,5,5-tetramethyl-D-pyrroline-3-methyl)-methanethiosulfonate was carried out as described in Der-Sarkissian *et al.* ^[59] with slight modifications. Briefly, DTT was removed prior to labeling from the buffer using Sephadex-G25 fast desalting columns (PD-10 columns, Amersham Biosciences) and the proteins were equilibrated in 20 mM Tris, pH 7.4, 100 mM NaCl (or 50 mM Na-phosphate, pH 7.4, 100 mM NaCl). Free sulfhydryl groups were reacted with a 5-fold molar excess of the MTSL maleimide reagent solubilized in acetone, at 4 °C for 16 h,

wrapped by aluminum foil. Access of spin label was removed during dialysis against four liters NMR-buffer (50 mM Na-phosphate, pH 7.4, 100 mM NaCl or 300 mM NaCl). Complete labeling with the nitroxide radical was verified by mass spectrometry and proteins were aliquoted, flash freezed in liquid N₂ and stored at -80 °C.

2.2.2.3. Phosphorylation of α -synuclein *in vitro*

wt and variants of α S (S87A, S87E, S129A and S129D) were phosphorylated by Casein Kinase1 (CK1) (specific activity 2,000,000 U/mg) (New England Biolabs) at a concentration of 1.44 mg/ml (100 μ M), unless otherwise stated. The reaction was carried out in the presence of 1.09 mM ATP (Sigma), 1x reaction solution supplied with the enzyme and 1200U of CK1/145 μ g of α S. The reaction was stopped with ethylenediaminetetraacetic acid (EDTA) disodium salt (5 mM final concentration). The progress of the reaction was monitored by RP-HPLC and mass spectrometry. The *in situ* phosphorylation assay was performed in a Shigemmi NMR tube (Shigemmi, Inc. USA) at 15 °C, with a sample containing 100 μ M ¹⁵N-labeled wt or mutants α S and 2 mg/ml CK1 in the standard phosphorylation buffer. After addition of 1.5 mM ATP solution, a series of ¹H-¹⁵N HSQCs were measured on a Bruker 600 MHz spectrometer. Each HSQC was measured with 16 scans per increment for 90 minutes.

2.2.2.4. Synthesis of random coil peptides

Synthesis of random coil peptides was made by Dr. Volker Klaukien in the department of NMR-based Structural biology, MPIBPC. Two types of random coil peptides, Ac-GGXAGG-NH₂ and Ac-GGXGG-NH₂, were synthesized employing standard solid-phase Fmoc chemistry. The peptides were purified by semi-preparative

C₄-RP column (see 2.2.2.5) and the purity (> 95 %) were analyzed by mass spectrometry (MS).

2.2.2.5. Reversed phase-high performance liquid chromatography (RP-HPLC)

RP-HPLC systems were operated by Gerhard Wolf in the department of NMR-based Structural biology, MPIBPC. Monitoring the phosphorylation reaction and purification of the various phosphorylated species of wt, S129E, S129A, S87E and S87A α S and synthesized random coil peptides were accomplished using RP-HPLC on JASCO systems using semi-preparative C₄- or C₁₈-RP column. A 35-50 % linear gradient (flow rate 1 ml /min) [0.09 % (v/v) trifluoroacetic acid (TFA) (buffer A)/90 % (v/v) acetonitrile aqueous solution (buffer B)] was applied, and the signal was monitored at 214 nm.

2.2.2.6. Sample preparation for supercooled water.

For measurements in supercooled water at -15 °C, monomeric α S (100 μ M protein) and fibrillar α S were suspended in 50 mM Na-phosphate buffer pH 7.4, 300 mM NaCl and injected into glass capillaries of 1.0 mm outer diameter (Wilmed-Labglass, USA) using 25 μ m syringe (Hamilton Syringe, USA).



Figure 2.2: Open-ended glass capillaries of different dimensions. Comparisons of outer dimension 1.0 mm OD, 1.7 mm OD capillaries and thin-walled 5 mm NMR tube.

Ends of the capillaries were flame sealed, and ten capillaries were placed in a 5 mm NMR tube (Fig.2.2) ^[39]. Prior to insertion of the sample into the NMR spectrometer, the temperature was set to $-15\text{ }^{\circ}\text{C}$.

2.2.2.7. Protein aggregation assay

Investigation of amyloid fibril formation requires not only the ability to distinguish the characteristic ordered extended β -sheet structure from the amorphous aggregates, but quantification of the amyloid form as well. Thioflavin-T (ThT) is commonly used to stain amyloid fibrils *in vitro* ^[60, 61] (Fig.2.3). Upon binding to amyloid fibrils, ThT exhibits a spectral shift of 100 nm for excitation ($\lambda_{\text{ex}} = 342\text{ nm}$ to 442 nm) and 50 nm for emission ($\lambda_{\text{em}} = 430\text{ nm}$ to 482 nm). This large fluorescence spectral shift allows selective excitation of amyloid fibrils bound to ThT. Characteristic spectral alterations that occur for a variety of amyloid fibrils are absent when ThT binds to the precursor monomers or amorphous aggregates.

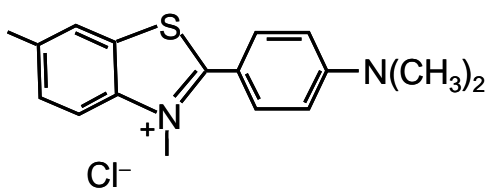


Figure 2.3: Structure of Thioflavin-T (ThT) compound. Fluorescence with ThT was used to detect amyloid fibrils of αS containing β -sheets.

Aggregation measurements of αS were performed with $100\text{ }\mu\text{M}$ protein in 20 mM Tris, $\text{pH } 7.4$, 100 mM NaCl containing $0.01\text{ }\%$ NaN_3 (Sigma). In all experiments $500\text{ }\mu\text{l}$ of protein sample were incubated in glass vials (Zinsser Analytik, Frankfurt, Germany) at $37\text{ }^{\circ}\text{C}$ under constant stirring (200 rpm) with magnetic microbars. The

amount of fibril formation at different time points was carried out by ThT assay. Briefly, 5-10 μ l aliquots were withdrawn from the incubations and diluted into 2 ml of 50 μ M ThT in 50 mM Glycine buffer, pH 8.0. ThT fluorescence was measured in a Varian Cary Eclipse spectrofluorimeter, with an excitation wavelength of 446 nm. Fluorescence emission from 460 to 600 nm was collected. Fluorescence at 480 nm was employed for determination of the relative content of α S fibrils in the sample. ThT fluorescence values were normalized to the values at the end of the aggregation assay.

2.2.2.8. Immunoblotting (dot blotting)

A technique for detecting, analyzing, and identifying proteins, similar to the western blot technique but differing in that protein samples are not separated electrophoretically but are spotted through circular templates directly onto the membrane or paper substrate ^[62]. wt α S, oligomers and fibrils were spotted onto nitrocellulose membrane (Protran BA85, 0.45 μ m pore size). 2 μ l-8 μ l of sample was loaded onto nitrocellulose membrane. Blotting was performed using the conformation-specific A11 antibody (1:1000, Invitrogen's Biosource) as described previously ^[62]. The amount of protein used for each spot was around 10 μ g. In a parallel experiment, same samples were blotted using the anti- α S antibody (1:2000, BD Biosciences). The amount of the protein used was 1 μ g.

2.2.2.9. Lipid bilayer experiments

Black lipid bilayer membranes were performed as described by Benz *et al* ^[63] and performed by Elke Maier in Prof. Roland Benz group, Würzburg, Germany. The instrumentation consisted of a teflon chamber with two aqueous compartments

connected by a small circular hole with a surface area of about 0.4 mm². Membranes were formed across the hole by painting on a 1 % solution of asolectin (lecithin type IIIs from soy beans from Sigma Chemical Co., St. Louis, MO) in n-decane. The aqueous salt solutions (Merck, Darmstadt, FRG) were buffered with 10 mM HEPES–KOH and had a pH 7.0 if not stated otherwise. The temperature was maintained at 20 °C throughout. The potentials applied to the membranes throughout the study refer always to those applied to the cis (front) side, the side of addition of α S oligomer. Similarly, positive currents were caused by positive potentials at the cis side and negative ones by negative potentials at the same side. The membrane current was measured with a pair of Ag/AgCl electrodes with salt bridges switched in series with a voltage source and an electrometer (Keithley 617). In case of the current recordings the electrometer was replaced by a home-made current amplifier with a band-width of either 100 or 300 Hz dependent on the membrane conductance. The amplified signal was monitored and recorded with a personal computer or a strip chart recorder.

For selectivity measurements, the membranes were formed in a 3 M KCl solution. wt α S monomer, amyloid fibrils and oligomers were added to both sides of the membrane respectively, and the increase in membrane conductance due to insertion of pores was observed with an electrometer. Analysis of the zero current membrane potential was performed using the Goldman–Hodgkin–Katz equation ^[64]. For activity measurements wt α S monomer, amyloid fibrils and oligomers were added at different concentrations to the membrane and the membrane conductance was taken, every 30 min after the addition, until further conductance increase with time was negligible ^[65]. The applied membrane potential was +50 and +100 mV.

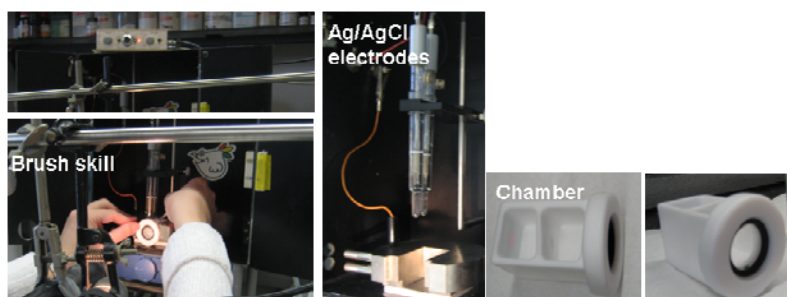


Figure 2.4: Basic equipments for planary bilayer lipid membrane experiment.

2.2.3. NMR spectroscopy

NMR spectra were generally acquired at 15 °C on a 100 μ M sample of ^{15}N labeled αS in buffer A (20 mM Tris, pH 7.4, 100 mM NaCl) or B (50 mM Na-phosphate, pH 7.4, 100 mM NaCl). For triple resonance experiments, spectra were acquired on ^{15}N - ^{13}C labeled αS . For low temperature measurements (-15 °C), buffer B salt concentration was increased 300 mM in order to avoid freezing of the sample during the experiments. All NMR spectra were processed using XWINNMR 3.5 (Bruker AG, Karlsruhe, Germany) or NMRPipe/NMRDraw ^[66] and analysed using NMRView 5.0.4 ^[67] or Sparky 3 (T.D Goddard and D.G. Kneller, University of California, San Francisco). Description of methods has been restricted to paramagnetic relaxation enhancement (PRE), pulsed field gradient NMR and dynamics relaxation experiments. In addition, a short insight into the ^1H - ^{15}N HSQC, the basic standard-NMR experiment employed in this work is provided.

2.2.3.1. ^1H - ^{15}N HSQC

The sensitivity in NMR is dependent upon the gyromagnetic ratio and natural abundance of the nucleus with half-integral spin quantum number. As both these terms are superior in protons over any other nuclei, transfer of magnetization from proton to

any other nuclei can be performed by complex pulse sequences. Heteronuclear NMR involves the transfer of magnetization between nuclei of different nature (^1H , ^{15}N , ^{13}C , etc.). Excitation of the proton (^1H), followed by polarization transfer to the heteronucleus (^{15}N), and subsequent reverse polarization transfer to the proton for detection, offers high sensitivity ^[68].

The pulse sequence for a basic HSQC experiment is shown in Figure 2.5. The experiment employs two INEPT (Insensitive nuclei enhancement through polarization transfer) magnetization transfers. The first one creates an anti-phase heteronuclear coherence ($I_Y \rightarrow 2I_ZS_Y$) and the second is used to convert this coherence back to observable magnetization ($2I_ZS_Y \rightarrow I_Y$) ^[69]. The first INEPT step creates a proton anti-phase magnetization ($2I_XS_Z$) during τ .

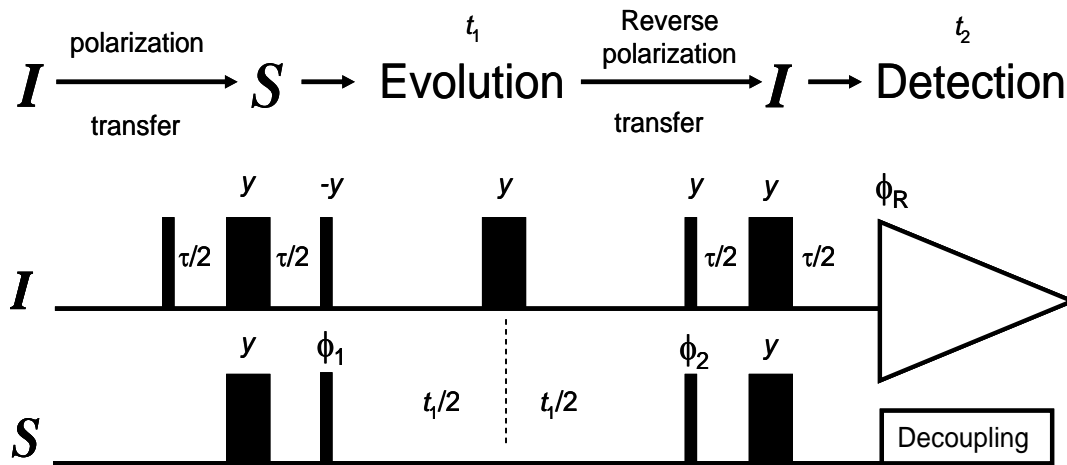


Figure 2.5: Fundamental pulse sequence for a HSQC experiment. Narrow and wide pulses correspond to 90° and 180° flip angles, respectively, with the indicated phase. The delay τ is set to $1/(2J_{IS})$. Decoupling of the S-spins during acquisition is accomplished using the Waltz-16 sequence. The basic phase cycling ϕ_1 (x, -x, x, -x), ϕ_2 (x, x, -x, -x), and receiver ϕ_R (x, -x, -x, x) is applied in the sequence.

To refocus chemical shift modulation during this period, a 180° pulse on both spins is introduced in the middle of τ period. Coherence is subsequently transferred to the directly attached heteronucleus (^{15}N for example) by simultaneous 90° pulses on both spins ($2I_ZS_Y$). The S -spin coherence is frequency-labeled during the t_I period. The 180° pulse on the I -spin in the middle of t_I refocuses the evolution of heteronuclear J_{IS} coupling. The 90° pulse on both spins transfer the magnetization back to proton as anti-phase I -spin magnetization ($2I_Y S_Z$). The final spin-echo period converts this anti-phase term into in-phase proton magnetization ($2I_Y S_Z \rightarrow I_X$). The outcome of such a pulse sequence is a signal, detected in the proton dimension (F2), which contains information on the chemical shifts of both ^1H and ^{15}N nuclei, for a given nitrogen frequency observed. The desired frequency space is sampled by repeating the pulse sequence for variable frequencies on the nitrogen dimension (F1), and the set of one dimensional spectrum is merged in a single two dimensional representation, the 2D ^1H - ^{15}N HSQC spectrum. NH bonds will thus be seen as cross-peaks situated at the intersection between the ^1H and ^{15}N resonance frequencies or chemical shifts.

2D ^1H - ^{15}N HSQC experiments in wt αS , S87A, S87, S129A and S129E were recorded using 256 x 1024 complex incremental data points in F1 (^{15}N) and F2 (^1H) dimensions, with 8 to 32 scans per increment and a relaxation delay of 1.2 s. The sampled frequency space (sweep width) was 26 ppm for the nitrogen dimension (centered in 119 ppm) and 10 ppm for the proton dimension (centered in 4.7 ppm).

2.2.3.2. Paramagnetic relaxation enhancement (PRE)

2D ^{15}N - ^1H HSQC spectra were recorded of phosphorylation mimic αS mutants and αS Cys-containing mutants, with and without the paramagnetic MTSL-tag, HSQC

experiments were recorded using 256 x 1024 complex data points in F1 and F2 dimensions with 32 scans or 64 scans per increment and a relaxation delay of 1.2 s. The removal of the spin label for measuring of the diamagnetic state was accomplished by addition of 0.5 mM DTT to the protein solution and 30 min incubation at room temperature. The reported intensity ratios are averages over repeated measurements for up to three different protein preparations.

2.3.3.3. Diffusion coefficient and hydrodynamic radius

The Stokes-Einstein equation shows that the hydrodynamic radius (R_H) of a protein is inversely proportional to the diffusion coefficient (D) of the protein. PFG NMR experiments can detect the translational diffusion coefficient of molecule. However, since the diffusion coefficient is affected by temperature and solvent viscosity, the absolute value of the diffusion coefficient can be difficult to measure.

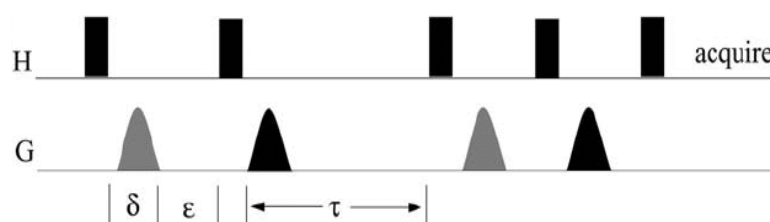


Figure 2.6: Pulse scheme of PG-SLED. The rectangles correspond to ^1H flip angle of 90° . The phase cycles are: $\varphi = x, x, y, y, -x, -x, -y, -y$; $\psi = x, -x, y, -y, -x, x, -y, y$. The delays are: $\delta = 6.3$ ms, $\epsilon = 1.0$ ms and $\tau = 100$ ms. The diffusion labeling gradients, shown in grey, were varied (2~95 %), while the crush gradients, shown in black, were applied at full as strength (adapted from Jones *et al* ^[56]).

wt αS , phosphorylated αS and phospho-mimic αS were acquired at 15°C on a $200\ \mu\text{M}$ unlabeled protein sample dissolved in 99.9 % D_2O , 20 mM phosphate buffer

pH 7.4, and containing dioxane (~20 mM) as an internal radius standard and viscosity probe [57]. To see the structural changes on α S with temperature, NMR experiments were performed from $-15\text{ }^{\circ}\text{C}$ to $47\text{ }^{\circ}\text{C}$ as mentioned above. Deuterium oxide was employed instead of water in order to minimize the power level necessary for water pre-saturation. 16 one-dimensional ^1H spectra were collected as a function of gradient amplitude employing the PG-SLED sequence (Fig.2.6) [56]. Each ^1H spectrum comprised 32 scans plus 16 steady-state scans. 16 K complex points were acquired with a spectral width of 6,000 Hz. With Topspin 2.0 (Bruker Biospin, Germany), the signals corresponding to the aliphatic region of the ^1H spectra (3.3-0.5 ppm) were integrated and the decay of the signal as a function of the gradient strength was fitted to a Gaussian function to determine d^{prot} . The same procedure was applied for the dioxane peak (~3.6 ppm) and the d^{ref} was measured. The R_{H} for the protein was calculated from the known R_{H} (2.12 Å) [57] for the dioxane and the ratio between the measured $d^{\text{ref}}/d^{\text{prot}}$.

2.2.3.4. Relaxation properties and motion

^{15}N relaxation T_2 , $T_{1\rho}$ and $^{15}\text{N}\{^1\text{H}\}$ -Steady state nuclear Overhauser effects (NOEs)

^{15}N relaxation data were acquired with modified versions of pulse sequences described earlier [70], incorporating pulsed field gradients and a WATERGATE for solvent suppression. T_2 times were sampled using seven different ^{15}N relaxation delays (Δ_{relax}): 3.8, 15.2, 22.8, 25.6, 91.2, 171, 342 and 3.8 ms. To extract ^{15}N T_2 relaxation times by measuring the peak height (I) for all spectra recorded with different relaxation delays and fitting the single-exponential function:

$$y = I(O) \exp(-\Delta_{\text{relax}} R_2^{-1}) \quad (12)$$

where R_2 is the transverse relaxation rate ($T_2 = 1/R_2$). Residue specific ^{15}N $R_{1\rho}$ spin relaxation rates were measured with a pulse sequence based on Farrow *et al.* [71] on a Bruker Avance 600 MHz spectrometer. Relaxation delays were set to 8, 48, 64, 128 and 184 ms with spin lock frequency of 2.5 kHz that makes a tilt angle bigger than 68° for the ^{15}N magnetization in the desired spectral width [72]. The peak intensity decay of each residue as a function of the delay time was fitted with single exponential curve and the corresponding $R_{1\rho}$ was acquired. Relaxation times were calculated by fitting an exponential function to the decaying signal integrals.

The heteronuclear nuclear Overhauser effect (NOEs) of ^{15}N nuclei in NH groups were measured using the Bruker standard pulse program `invinoef3gpse`. ^{15}N $\{^1\text{H}\}$ -NOEs values are reported as the ratio of peak heights in paired spectra collected with and without a period (4 s) of proton saturation during the 5-s recycle delay.

2.2.3.5. Secondary structure determination

^1H chemical shifts were referenced with 2,2-dimethyl-2-silapentane-5-sulfonic acid (DSS), and ^{15}N and ^{13}C chemical shifts were referenced indirectly [73]. Averaged secondary chemical shifts were calculated as $\Delta S = (3 \times \Delta S(^{13}\text{C}^\alpha) + 4 \times \Delta S(^{13}\text{C}')) / 7$, where $\Delta S(^{13}\text{C}^\alpha)$ and $\Delta S(^{13}\text{C}')$ are the difference between the experimental $^{13}\text{C}^\alpha$ and $^{13}\text{C}'$ chemical shifts and the corresponding random coil values [48, 73].

2.2.3.6. Mapping of long-range interactions by chemical shift differences

Chemical shifts depend on the local chemical environment of a nucleus. If effectors bind to a protein, this environment changes at the interaction site. This causes perturbations of the chemical shifts. These perturbations can be followed in every

NMR-spectrum. ^{15}N - ^1H -HSQC spectra have a high sensitivity. Therefore chemical shift values can be easily followed in the ^{15}N - ^1H -HSQC spectrum upon phosphorylation of the protein. The chemical shift perturbations are commonly combined with the following equation ^[74]:

$$\Delta\delta_{HN} = \sqrt{\frac{(\Delta\delta_N / 5)^2 + (\Delta\delta_H)^2}{2}} \quad (13)$$

$\Delta\delta_{HN}$: average amide chemical shift perturbation

$\Delta\delta_N$: amide nitrogen chemical shift changes

$\Delta\delta_H$: amide proton chemical shift changes

2.2.4. Other spectroscopic methods

2.2.4.1. UV absorbance

The concentration of proteins in solution was determined, according to the Lambert-Beer law, by measuring the absorption at 280 nm (A_{280}).

$$A_\lambda = \varepsilon_\lambda \cdot c \cdot d \quad (14)$$

A_λ : absorption at wavelength λ

ε_λ : molar extinction coefficient at wavelength λ in $\text{M}^{-1}\text{cm}^{-1}$

c : protein concentration (M)

d : thickness of the cuvette (cm)

2.2.4.2. Electrospray Quadrupole Mass spectrometry

For Electrospray Quadrupole Mass spectrometry the source capillary was set to 2.94 kV. Scans were acquired in positive-ion mode at m/z 500-2500. It was performed after RP-HPLC (see 2.2.2.5).

2.2.4.3. Circular dichroism (CD) spectroscopy

The secondary structure of monomeric α S, fibrils and dissociated fibrils were determined by CD spectroscopy using a Photophysics Chirascan spectrometer at the Department of neurobiology, MPI-BPC. The Far UV-CD spectra (190-250 nm, integration time of 2 seconds for 0.2 nm) were collected at 15 °C in a 1 mm path length quartz cuvette containing 100 μ M of protein in buffer 50 mM Na-phosphate buffer pH 7.4, 300 mM NaCl. Data were expressed as difference absorbance (ϵ) or circular dichroism ($\Delta\epsilon$) per molar concentration of protein. Spectrophotometric data were fit using the program Chirascan.

2.2.4.4. Electron microscopy (EM)

Electron microscopic images were taken by Dr. Dietmar Riedel at the Department of neurobiology, MPIBPC. For EM studies, wt α S or other aggregated protein samples were deposited on Formvar-coated 200 mesh copper grids (Electron Microscopy Sciences) at a concentration of 25 μ M. Grids were washed with two drops of water and stained with two drops of freshly prepared 0.75 % (w/v) uranyl acetate (Electron microscopy sciences). Specimens were inspected on a Philip CIME 12 electron microscope, operated at 80 kV. Digitized photographs were recorded with a slow scan CCD camera.

3. Correlation of amyloid fibril β -structure with the unfolded state of α -synuclein

3.1. Introduction

Many human neurodegenerative disorders, including Alzheimer's and Parkinson's disease, are associated with the deposition of proteinaceous aggregates known as amyloid fibrils^[75, 76]. Surprisingly, proteins with very different amino acid sequences and three-dimensional structures aggregate into amyloid fibrils that share common characteristics such as a similar morphology and a specific β -sheet based molecular architecture^[77, 78] (Fig.3.1). This suggests that the ability to fibrillate is an intrinsic property of a polypeptide chain and that the native structure is not necessarily the only ordered structure that each protein can assume^[3].

An additional common property of aggregation into amyloid fibrils is the presence of partially or fully unfolded states of the misfolding proteins. For proteins that are natively folded, unfolded states are present during biosynthesis, or as a result of proteolytic degradation^[3, 79-81]. Though there is increasing knowledge about the factors that drive aggregation^[82, 83], the structural characteristics of aggregation-prone states and the molecular details that determine the arrangement of misfolded proteins in amyloid fibrils are not still fully understood.

Is a high population of a specific conformation in denatured states required for the efficient generation of amyloid fibrils? What is the relation between the properties of the unfolded state and the β -structure in amyloid fibrils? Are differences in the

morphologies of the resulting fibrils associated with differences in the structures of the precursor states?

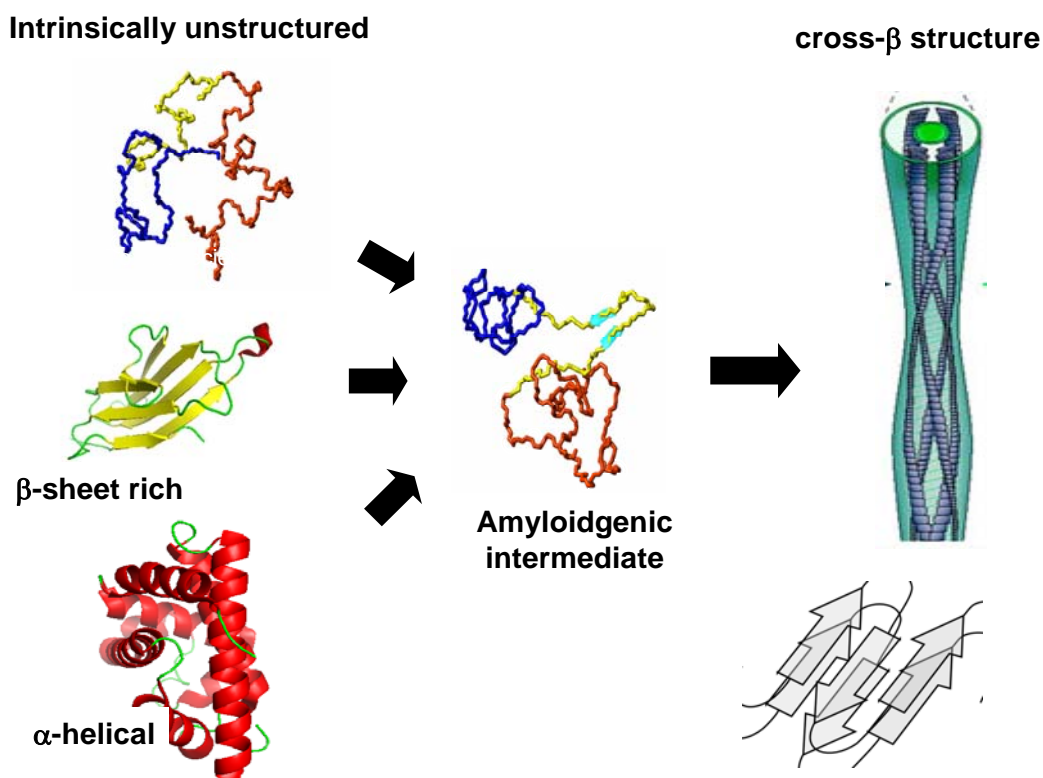


Figure 3.1: A schematic representation of the general mechanism of aggregation to form amyloid fibrils. Is the secondary β -structure of fibrils encoded in the denatured state of the monomer structure?

In this chapter, it is demonstrated by a combination of solution-state and solid-state NMR spectroscopy that the structure of amyloid fibrils is directly correlated to the conformational properties of the unfolded state. To induce the fully unfolded state we introduced supercooled water. When the temperature of the solution is reduced sufficiently without freezing, proteins can be denatured without the need for chemicals that would potentially interfere with the ensemble of conformations present in solution. In addition, interconversion between different conformations that causes averaging of

spectroscopic probes at higher temperatures is slowed down. Similar or even identical spectroscopic probes are used in solution-state and solid-state NMR, allowing a detailed comparison of the structure of proteins in their unfolded and fibrillar states.

3.2. Experimental procedure

Sample preparation for supercooled water: Expression and purification of ^{15}N - and $^{13}\text{C}/^{15}\text{N}$ -labeled wt α S were performed as described in 2.2.2.1. For measurements in supercooled water at $-15\text{ }^\circ\text{C}$, monomeric wt α S was dissolved in 50 mM Na-phosphate buffer, pH 7.4, 300 mM NaCl and taken up into open-ended glass capillaries of 1.0 mm outer diameter. The ends of the capillaries were flame sealed, and the capillaries were placed in a 5-mm NMR tube (see 2.2.2.6). Preparation of spin labeled α S was performed after the purification (see 2.2.2.2).

NMR Spectroscopy: Solution-state NMR experiments were recorded on Bruker Avance 600 and 700 MHz NMR spectrometers (see 2.2.3). Pulse field gradient NMR experiments were acquired using the PG-SLED sequence and Errors in hydrodynamic radius were estimated from repeat measurements and were about 0.3 \AA (see 2.3.3.3).

3.3. Results and discussion

3.3.1. Backbone assignment of α -synuclein at $-15\text{ }^\circ\text{C}$

Previous assignments of backbone resonances performed in our laboratory had independently corroborated the assignment of α S in physiological aqueous solution ^[84]. For the characterization of the structure and dynamics of α S at $-15\text{ }^\circ\text{C}$, we had to determine the sequence-specific assignment of backbone resonances of α S. 3D ^{15}N - ^1H

3. Correlation of amyloid fibril β -structure with the unfolded state of α S

NOESY-HSQC, (HA)CANNH^[85], HNC0 and HN(CA)CO were acquired at $-15\text{ }^{\circ}\text{C}$ on Bruker Avance 700 and DRX 600 spectrometers. Aggregation did not occur under this low temperature without stirring.

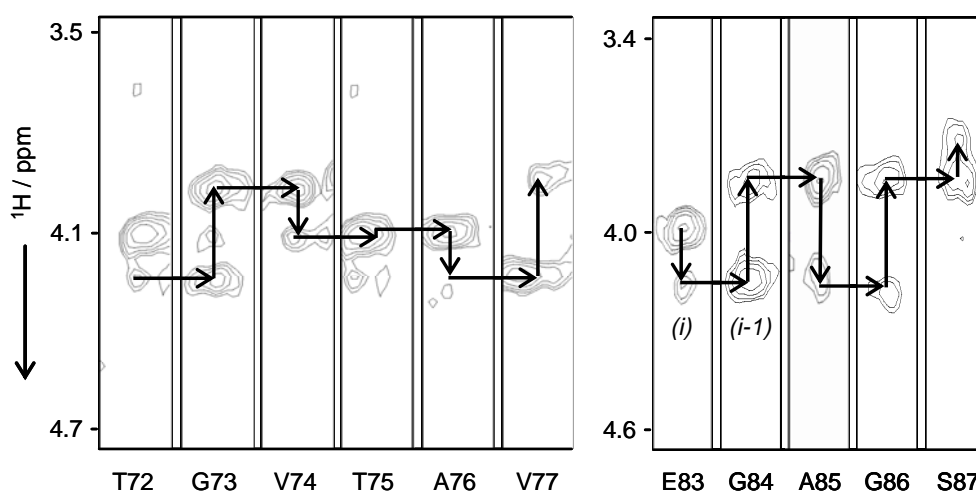


Figure 3.2: Selected strips of the 3D ^{15}N - ^1H NOESY-HSQC spectrum at $-15\text{ }^{\circ}\text{C}$, highlighting the sequential connectivities observed in the region T72–S87. Intra- and inter-residual H^{α} resonances are indicated.

Regions of secondary structure were confirmed by the sequential connection and by the characteristic NOE patterns^[50] in the 3D ^{15}N - ^1H NOESY HSQC (Fig.3.2). As observed in the ^1H - ^{15}N HSQC spectrum shown on Figure 3.3 amide cross-peaks of α S at $-15\text{ }^{\circ}\text{C}$ are localized into the narrow chemical shift dispersion in the ^1H dimension and some peaks are shifted.

3.3.2. Comparison of secondary chemical shifts and NOE intensity at +15 °C and -15 °C

The effect of cold denaturation on the structural properties of α S was investigated by comparison of NMR parameters of +15 °C and -15 °C. Although there are only small differences in the ^1H - ^{15}N HSQC spectra of α S between +15 °C and -15 °C, the averaged C^α and C' chemical shifts shows certain important differences between two temperatures (Fig.3.4.a).

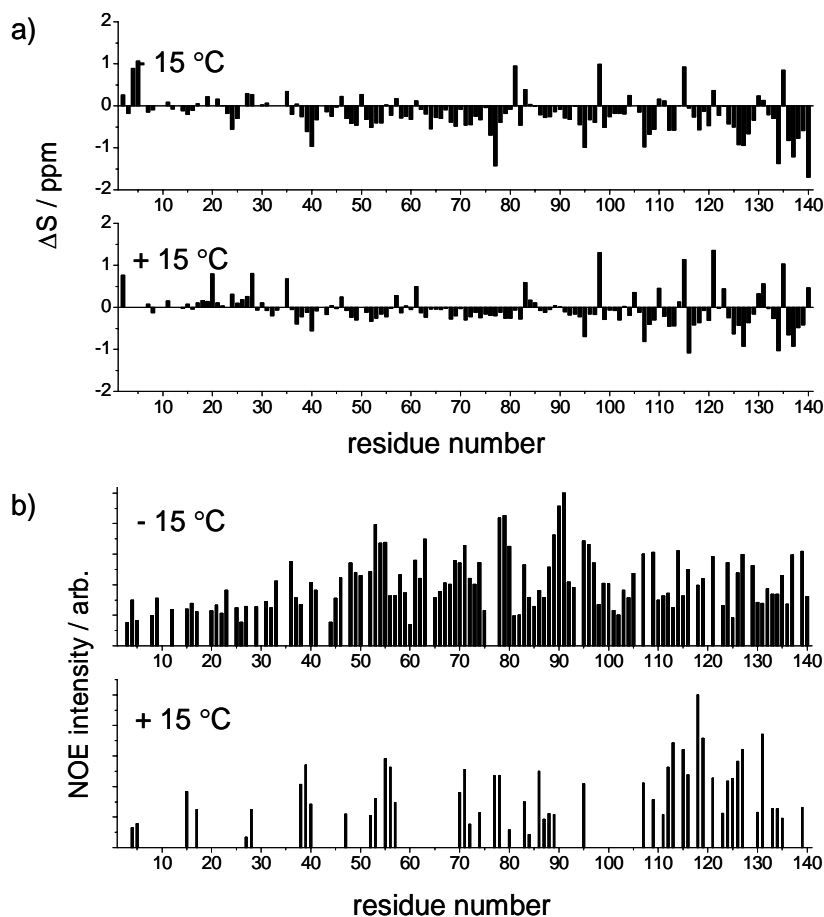
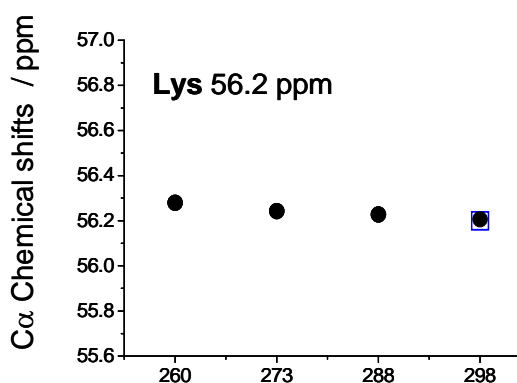


Figure 3.4: Comparisons of secondary chemical shifts and NOE intensity. a) Averaged C^α and C' secondary chemical shifts in α S at -15 °C and +15 °C. b) $\text{HN}_i\text{H}_{i-1}$ normalized NOE intensities in α S at -15 °C and +15 °C.

3. Correlation of amyloid fibril β -structure with the unfolded state of αS

At $-15\text{ }^{\circ}\text{C}$, it demonstrated that residues 39-98 have slightly increased negative secondary chemical shifts. In addition, the helical propensity previously observed for residues 18-31 ^[86] is no longer observable. To further search for factors that could explain the chemical shifts patterns, $\text{H}^{\text{N}}_{i-1}-\text{H}^{\alpha}_{i-1}$ NOE intensities were compared both temperatures. The highest normalized NOE intensities between the amide proton of a residue and the H^{α} atom of the previous residue were detected in the NAC region at $-15\text{ }^{\circ}\text{C}$. Both results indicate an increased propensity of residues 38-98 to populate extended structure. In contrast, at $+15\text{ }^{\circ}\text{C}$, many $\text{HN}_i\text{H}^{\alpha}_{i-1}$ NOE peaks were broadened beyond detection due to increased conformational averaging (Fig.3.4.b).

To calculate correct values for secondary structure, the random coil values ($\delta\text{C}_{\text{coil}}$) should be accurate. To confirm the temperature dependence of $^{13}\text{C}^{\alpha}$ random coil values, the amino acids embedded in Ac-GGXAGG-NH_2 ^[87] peptides were investigated with decreasing the temperature from $+15\text{ }^{\circ}\text{C}$ to $-15\text{ }^{\circ}\text{C}$. In all cases, changes in peptide chemical shifts were below 0.06 ppm (Fig.3.5).



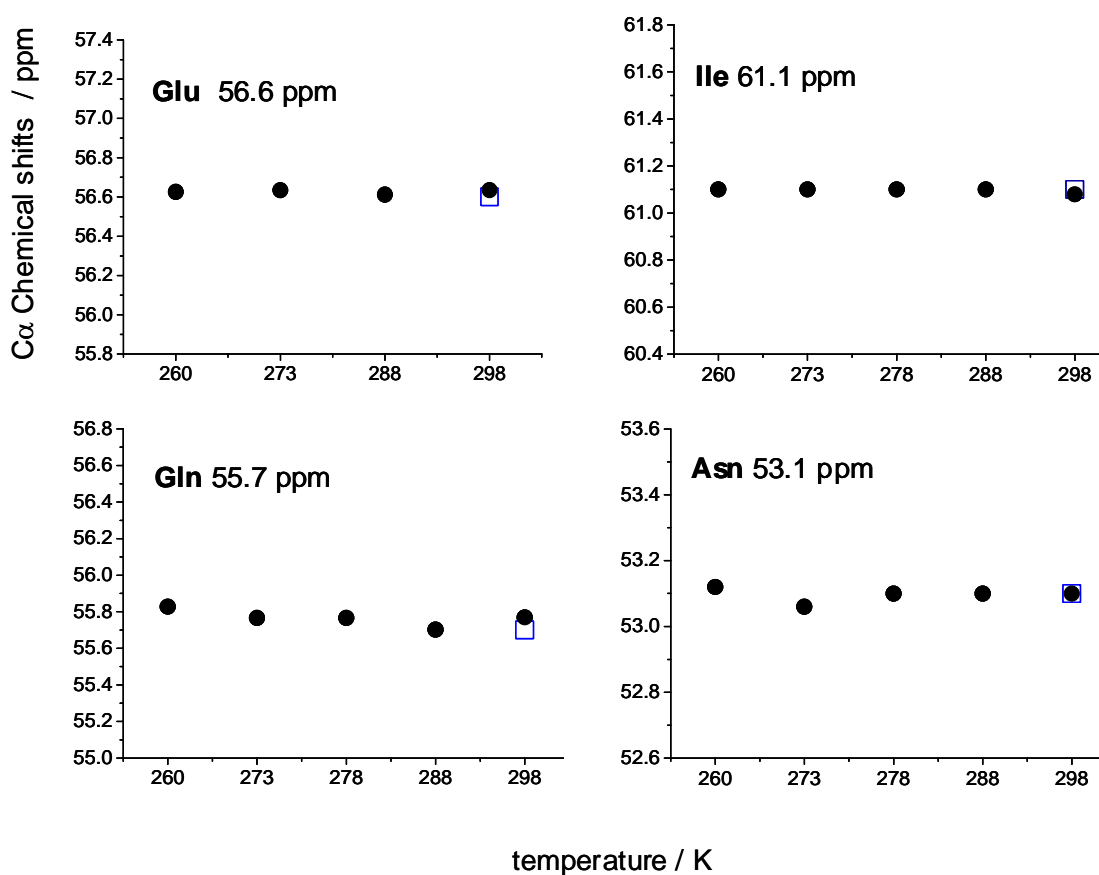


Figure 3.5: Temperature dependence of C^α chemical shifts for amino acids embedded in Ac-GGXAGG-NH₂ peptides. Random coil $^{13}C^\alpha$ chemical shifts for Lys, Glu, Gln, Ile, and Asn amino acids. Temperatures calibrated by methanol, chemical shifts are referenced to internal DSS^[73] at various temperatures, 50 mM Na-phosphate buffer pH 7.4, 300 mM NaCl.

3.3.3. Attenuation of transient long-range interactions in α -synuclein at -15°C

Using thin glass capillaries (see 2.2.2.6)^[39], the protein solution was cooled to -15°C without freezing. For wt α S, containing with 300 mM NaCl, a hydrodynamic radius of 29.3 Å was obtained at $+15^\circ\text{C}$. Upon addition of 8 M urea, it increased to 36.4 Å, and 36.6 Å at -15°C . If α S was a complete random coil structure, a hydrodynamic radius of 36.9 Å would be expected^[88]. Figure 3.6 shows that the hydrodynamic radius of α S was significantly increased up to 36.6 Å at -15°C and adopted a value similar to

that observed in the presence of 8 M urea at +2 °C, +15 °C and +47 °C. At high temperature, on the other hand, the hydrodynamic radius reached a maximum value that was further increased upon addition of urea, suggesting that long-range interactions are more efficiently removed at –15 °C than at +57 °C.

Following Gibbs-Helmholtz equation, proteins generally have a large positive ΔC_p and are predicted to unfold at both high and low temperatures. Cold denaturation causes a decrease in the enthalpy and entropy functions whereas heat denaturation causes their increase. Therefore, cold and heat denaturation are likely to be driven by different mechanisms.

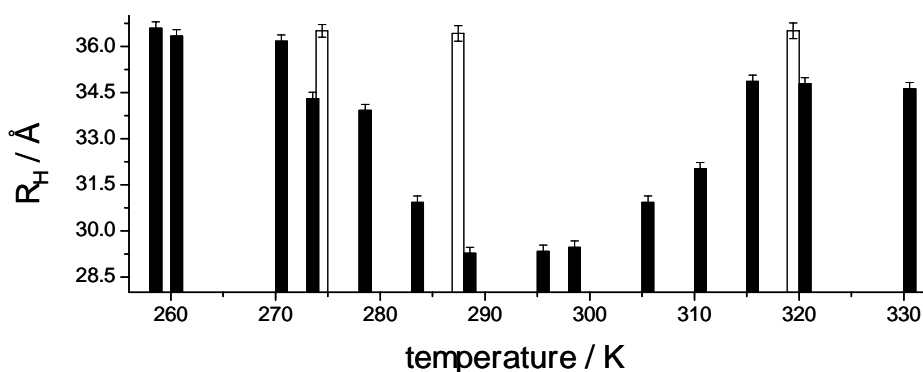


Figure 3.6: Hydrodynamic radius of αS . 50 mM Na-phosphate, pH 7.4, 300 mM NaCl buffer in the temperature range from –15 °C to +57 °C (black bars). Open bars indicate hydrodynamic radii in the presence of 8 M urea.

A paramagnetic relaxation enhancement (PRE) of amide protons due to the presence of a nitroxide spin label attached to residue 18 was also observed. At +15 °C, the decrease in peak intensity ratios that occurs in the C-terminal domain (far from the site of spin labeling), reports on a long-range interaction between the N- and the C-terminal domain ^[53] (Fig.3.7.a). The reduction of line broadening in the C terminus

indicates the removal of transient long-range interactions at $-15\text{ }^{\circ}\text{C}$ (Fig.3.7.b), in agreement with the increase in hydrodynamic radius. For residues 37-45, peak intensity ratios remained smaller than those expected for a random coil polypeptide, suggesting that more local interactions might not be fully removed.

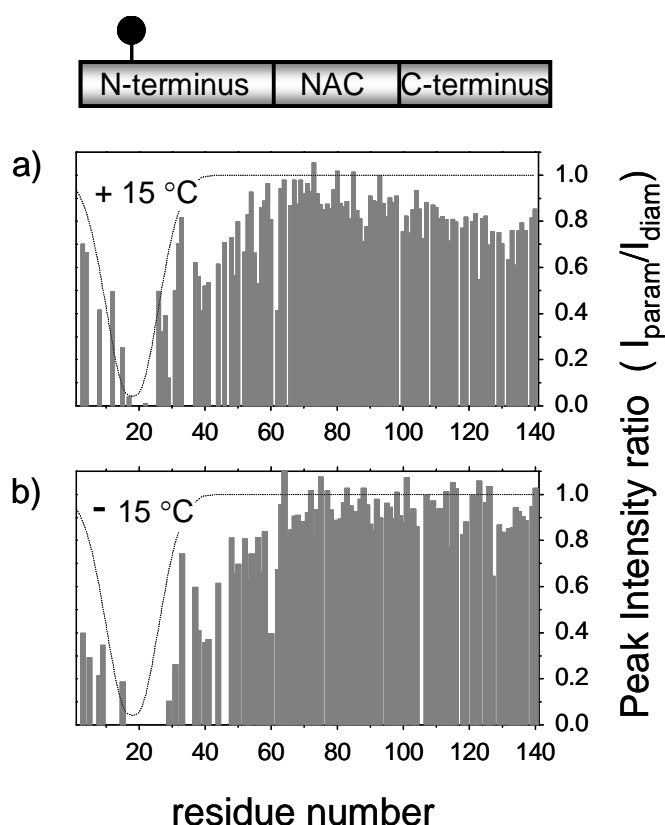


Figure 3.7: NMR paramagnetic relaxation enhancement of amide protons in α S. at a) $+15\text{ }^{\circ}\text{C}$, b) $-15\text{ }^{\circ}\text{C}$. The dotted line shows the profile of the paramagnetic broadening expected for a random coil polypeptide.

3.3.4. Correlation of amyloid β -structure with the unfolded state of α -synuclein

Previous solution-state NMR studies on natively unfolded proteins have shown that proteins in the unfolded state display deviations from a random coil structure, in particular in the regions which are converted into amyloid β -structure during

aggregation^[89-92]. However, for regions in which negative secondary chemical shifts identify nascent β -structure in solution, strong negative secondary chemical shifts were observed in α S fibrils. A detailed comparison of the conformational properties of the fibrillar and unfolded state was not possible so far due to a lack of high-resolution structural information for amyloid fibrils.

As shown in Figure 3.8, the secondary chemical shifts in the unfolded state of α S are compared to the recent observation made by solid-state NMR in amyloid fibrils of α S^[93], and the values detected in solution at $-15\text{ }^\circ\text{C}$. Clearly, the secondary chemical shifts in the monomeric state at $-15\text{ }^\circ\text{C}$ in solution are smaller than those observed in amyloid fibrils. For residues 1-38, the sign of secondary NMR chemical shifts was alternating, indicating the absence of a propensity for either helical or β -structure. Residues 38-98, which form the core of amyloid fibrils, as well as the acidic C-terminal domain showed predominantly negative secondary chemical shifts. While negative secondary chemical shifts are characteristic of either β -structure or poly-proline helix-like conformations, large $^3J_{\text{H}^{\text{N}}\text{H}^\alpha}$ scalar couplings are only found in extended β -structure. In the C-terminal domain of α S, $^3J_{\text{H}^{\text{N}}\text{H}^\alpha}$ were mostly below average in agreement with the presence of several proline residues. Only for residues 38-98, negative secondary chemical shifts and above average $^3J_{\text{H}^{\text{N}}\text{H}^\alpha}$ couplings were observed suggesting that the central domain of α S transiently populates the β -region in the Ramachandran plot. In addition, residues L38, H50, E61, T81 and E83, which had positive or only slightly negative secondary chemical shifts in α S fibrils indicating the ends of β -strands, showed positive values in the unfolded state.

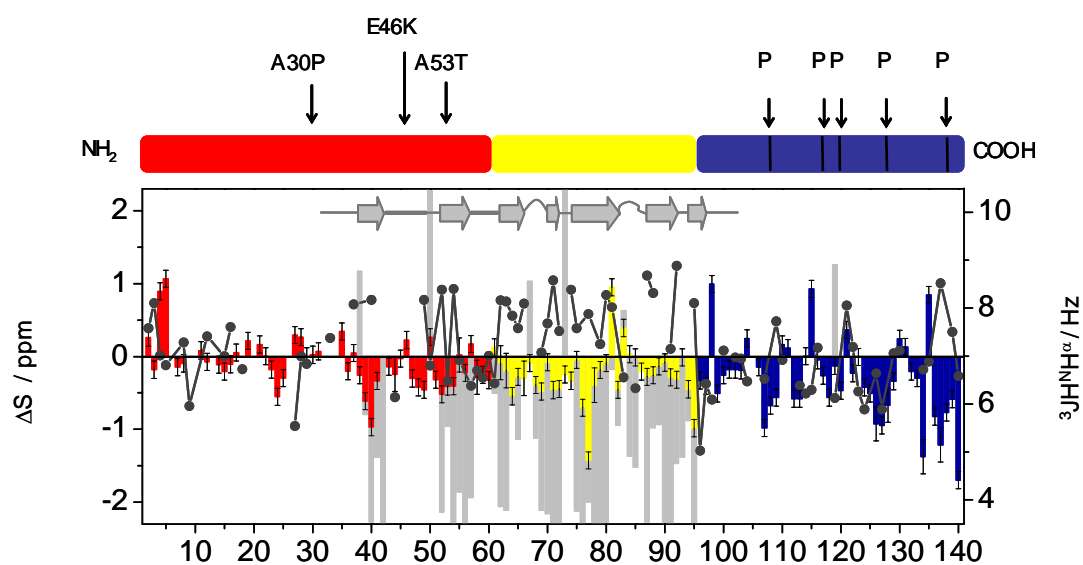


Figure 3.8: Comparison of averaged C^α and C' secondary chemical shifts in the unfolded state of α S (colored bars) with those observed in α S fibrils (grey bars). Continuous stretches of negative values indicate β -structure. $^3J_{H^N H^\alpha}$ scalar couplings observed at -15°C in solution are represented by black dots. $^3J_{H^N H^\alpha}$ couplings were measured using intensity modulated HSQC [94]. Missing values are due to overlap and glycines; β -strands and loops in the core of α S fibrils [59, 93] are indicated by grey arrows and curved line. Red, yellow and blue denote the basic N-terminal domain, the highly amyloidogenic non-A β component of Alzheimer's disease amyloid region, and the C-terminal domain, respectively.

$\Delta^{13}C^\alpha$ is the difference between the experimental $^{13}C^\alpha$ chemical shifts in α S and random coil values determined experimentally from Ac-GGXAGG-NH₂ peptides [87]. These values do not include any sequence-dependent corrections. Note that the correlation is comparable to the one observed when random-coil values were used, that were obtained from Ac-GGXGG-NH₂ peptides and included corrections for neighboring residues. Accordingly, secondary chemical shifts in the unfolded state in solution were found to correlate significantly with those in α S fibrils. A straight-line fit to the data resulted in a correlation coefficient of 0.67. The scatter in Figure 3.9 may be

attributed to inaccuracies in the random coil chemical shifts and the fact that in the unfolded state non-hydrogen bonded β -structure is populated only transiently.

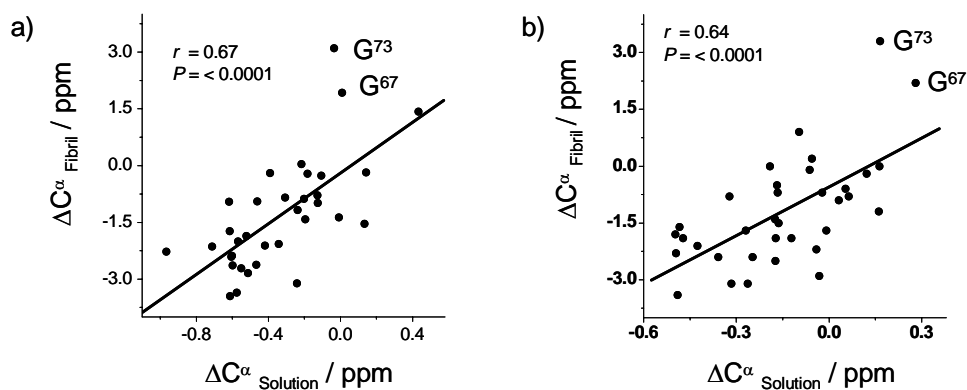


Figure 3.9: Correlation plot of C^α secondary chemical shifts in the unfolded state in solution versus values observed in the core of αS fibrils. a) Removal of the outlier G^{73} increases the correlation coefficient to 0.69. b) Non-sequence corrected random coil values were also tested and gave a comparable correlation of secondary chemical shifts in the unfolded and fibrillar state ($r = 0.64$).

Backbone torsion angles that directly report on secondary structure in proteins can be derived from NMR chemical shifts by the program TALOS [95]. In Figure 3.10 shows the φ/ϕ angles predicted by TALOS on the basis of NMR chemical shifts in solution at -15°C and on the basis of C^α/C' chemical shifts in amyloid fibrils. Even though the secondary chemical shifts in the unfolded state are far smaller, a significant number of torsion angles were obtained from TALOS. Dihedral angles were predicted by TALOS using experimental $^{13}\text{C}^\alpha$, $^{13}\text{C}'$ and ^{15}N chemical shifts and sequence corrected random coil values. Predictions with ten consistent matches labeled by TALOS as “good” were considered. Following the strategy that is used for the chemical shift index in globular proteins, predictions were only included when they were

3. Correlation of amyloid fibril β -structure with the unfolded state of α S

sequentially connected for at least two residues. The torsion angles predicted from the solution-state chemical shifts were characteristic of β -structure and agreed with values predicted by TALOS from the chemical shifts observed by solid-state NMR in α S fibrils (Fig.3.10.a).

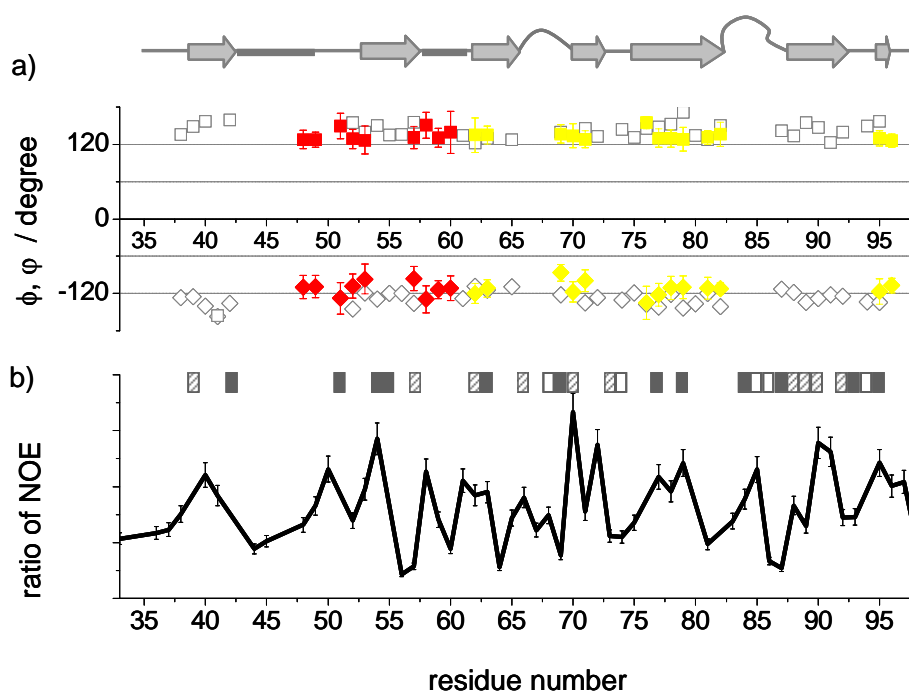


Figure 3.10: a) ϕ (diamonds) and φ (squares) torsion angles derived by TALOS ^[95] from $^{13}\text{C}/^{15}\text{N}$ chemical shifts observed by solution-state NMR in the unfolded state (colored) and observed by solid-state NMR in amyloid fibrils of α S (grey). b) Comparison of $(HN_iH^{\alpha}_{i-1})/(HN_i-HN_i)$ NOE intensity ratios in solution (black line) with $N_{i+1}H-HC^{\alpha}_i$ contacts (grey rectangles) in α S fibrils. Overlapped peaks and contacts that are clearly absent in the NHHC spectrum are marked by dashed and open rectangles, respectively.

For residues 38-40 and 87-92, no good predictions were obtained from the solution-state chemical shifts, although secondary chemical shifts were negative and chemical shifts in α S fibrils indicated the presence of a β -strand. This is most likely due to inaccuracies in the random coil chemical shifts and shortcomings of TALOS, which

on average can predict dihedral angles for 65 % of residues in globular proteins with an error rate of 3 % [95]. On the other hand, β -structure was predicted for residues 48, 49, 51 and 58-60 on the basis of solution-state chemical shifts, whereas no information is available for these residues in amyloid fibrils due to missing resonance.

Further support for the presence of amyloid seed structure in the unfolded state of α S was obtained by comparison of $H^N_i-H^{\alpha}_{i-1}$ nuclear Overhauser effect (NOE) intensities in solution with $N_{i+1}H-HC^{\alpha}_i$ contacts in the amyloid fibril. NOEs were extracted from a 3D ^{15}N - 1H NOESY-HSQC (mixing time = 50 ms). Solid-state NMR experiments on amyloid fibrils of α S have been reported previously [93]. $N_{i+1}H-HC^{\alpha}_i$ contacts indicated in Figure 3.10.b) were extracted from a NHHC correlation experiment with a (1H , 1H) mixing time of 80 μ s, bracketed by short 1H , X CP transfers for contact times of 90 μ s ($X = ^{13}C$) and 200 μ s ($X = ^{15}N$). The highest normalized NOE intensities between the amide proton of a residue and the H^{α} atom of the previous residue were detected in the NAC region (Fig.3.10.b). Many residues in the NAC region also showed $N_{i+1}H-HC^{\alpha}_i$ cross-peaks in a two-dimensional NHHC correlation experiment performed on α S fibrils under magic angle spinning conditions [96, 97]. Strong $H^N_i-H^{\alpha}_{i-1}$ NOEs in solution and $N_{i+1}H-HC^{\alpha}_i$ cross-peaks in the solid phase indicate the presence of β -structure (Fig.3.10.b).

3.4. Conclusion

In summary, the secondary structure of amyloid fibrils is directly encoded in the unfolded, monomeric state of misfolding proteins (Fig.3.11). This supports the idea that amyloid fibrils represent a general conformational state of a polypeptide chain, which

3. Correlation of amyloid fibril β -structure with the unfolded state of α S

reproduces the φ/ϕ -angle distribution that is most favorable to the main chain. The results also suggest that the fibrils assemble by association of unfolded polypeptide segments, which transiently populate non-hydrogen bonded β -structure. Additional polypeptides can bind in-register to preformed elements of amyloid structure only if they prefer a similar φ/ϕ -angle distribution along the chain that faithfully reproduces the conformational details of the previously established configuration.

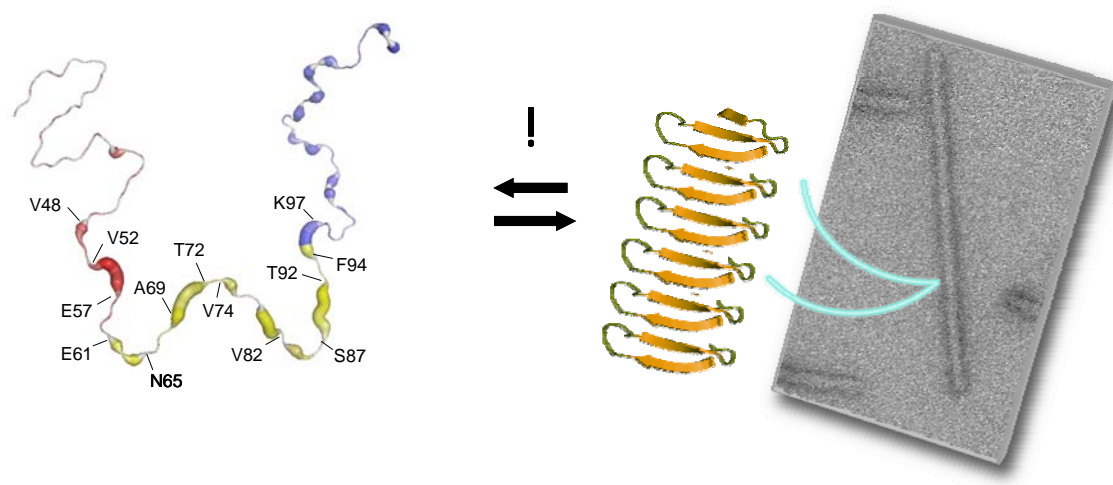


Figure 3.11: Schematic illustration of secondary beta-structure of fibrils encoded in the denatured state of monomer α S. Mapping of $\text{HN}_i\text{-H}^{\alpha}_{i-1}$ NOE intensities onto a three-dimensional coil model of α S at $-15\text{ }^\circ\text{C}$. The thickness of the coil corresponds to the relative NOE intensity. The structure of α S in amyloid fibrils was studied by various techniques, and these studies showed that the cores of α S fibrils are formed by residues ~ 34 to ~ 101 , comprising at least four β -strands, whereas the N- and C-terminal domains remain disordered ^[59, 93, 98].

4. Dissociation of amyloid fibrils of α -synuclein in supercooled water.

4.1. Introduction

Amyloid fibrils have a β -sheet rich molecular architecture called cross- β structure [99]. The β -sheet conformation imparts extremely high thermodynamic stability and remarkable physical properties to amyloid fibrils [100]. They are highly resistant to hydrostatic pressure and high temperature, while protofibrils and earlier aggregates are more sensitive to these extreme conditions [101, 102]. The stability of mature amyloid fibrils exceeds that of globular proteins, suggesting that they may represent the global minimum in free energy. In addition, they have strength comparable to that of steel [103]. Nature exploits these unusual properties of amyloidgenic structures for a variety of physiological functions [104]. Moreover, fibrillar peptide structures might have great potential as structural or structuring elements in nanotechnology applications [105].

The native state of proteins can be unfolded both by high temperature and by cooling. Cold denaturation is predicted by the Gibbs-Helmholtz equation and attributed to specific interactions of protein nonpolar groups with water; tightly packed structures unfold at sufficiently low temperature exposing internal nonpolar groups to water [36]. Direct observation of cold denaturation is generally hard to achieve in the absence of denaturant, extreme pH or mutations, as for most proteins the transition temperature is well below 0 °C. Freezing, however, can be avoided to temperatures as low as -20 °C with careful supercooling of small sample volumes [39, 106]. Nevertheless, this is generally not sufficiently cold to induce denaturation in stable, native proteins [36, 39]. In

this chapter, it is demonstrated that amyloid fibrils of the protein α S, which constitute the insoluble aggregates found in brains of patients suffering from PD, are highly sensitive to low temperature (Fig.4.1). Despite their remarkable stability to hydrostatic pressure and high temperatures, mature amyloid fibrils of α S are rapidly dissociated in supercooled water at $-15\text{ }^{\circ}\text{C}$.

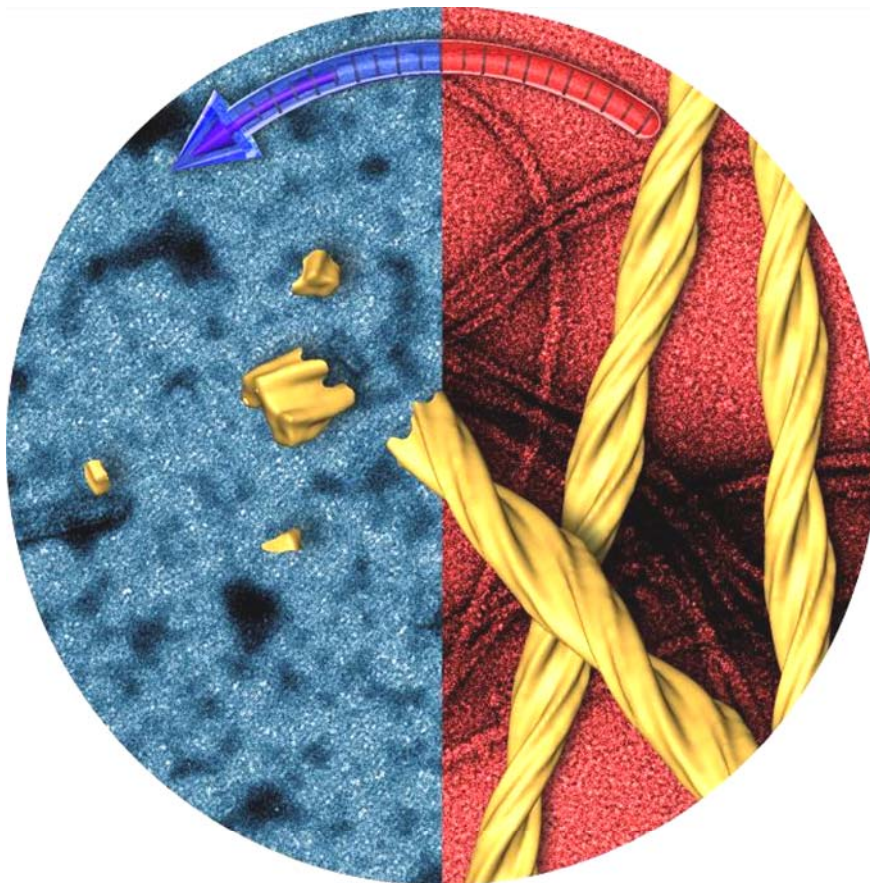


Figure 4.1: Schematic illustration of α S fibrils dissociated to monomeric state at $-15\text{ }^{\circ}\text{C}$. Amyloid fibrils formed by the protein α S, one of the key players in Parkinson's disease, are rapidly dissociated in supercooled water at $-15\text{ }^{\circ}\text{C}$, conditions in which many globular proteins remain folded.

4.2. Experimental procedure

Sample preparation for fibrillization and dissociation of α S fibrils: Recombinant α S was expressed and purified as described in 2.2.2.1. ^{15}N -labeled α S amyloid fibrils were prepared by incubating 100 μM freshly prepared ^{15}N -labeled α S in a solution of 20 mM Tris and 100 mM NaCl at pH 7.4 in the presence of 0.01 %sodium azide in glass vials. Incubation was carried out under continuous stirring with a micro-sized stir bar at 37 °C until a steady state was reached according to a stained ThT fluorescence assay (see 2.2.2.7). Matured fibrils were centrifuged at 215,000 x g with a TL 100 ultracentrifuge (Beckman Coulter). For measurements in supercooled water at -15 °C, monomeric α S (0.1 mM protein concentration) and fibrillar α S were suspended in 50 mM phosphate buffer (pH 7.4) and 300 mM NaCl, and injected into glass capillaries of 1.0 mm outer diameter (see 2.2.2.6). Prior to insertion of the sample into the NMR spectrometer, the temperature was set to -15 °C.

Preparation of spin-labeled α S: A single cysteine residue was introduced into α S at position 18 (A18C) and 140 (A140C) as described in 2.2.1.2.

NMR spectroscopy: NMR experiments were recorded on Bruker Avance 600 and 700 MHz NMR spectrometers. Dissociation of amyloid fibrils was followed by recording a series of 1D ^1H and 2D ^1H - ^{15}N HSQC spectra. Pulse field gradient NMR experiments were measured for the determination of the hydrodynamic radius (see 1.4.4 and 2.3.3.3). The ^{15}N $T_{1\rho}$ values were obtained by collecting five 2D spectra (see 2.2.3.4), and by collecting two 1D spectra using a delay of 2 and 100 ms for denatured fibrils. An on-resonance spin-lock pulse of 2.5 kHz was used. PRE profiles were derived from the

measurement of the ratios of the peak intensity between two 2D HSQC spectra in the presence (I_{para}) and absence (I_{dia}) of the nitroxide radical (see 1.4.3 and 2.2.3.2).

Transmission electron micrographs (TEM): Amyloid fibrils, resuspended from the pellet, were prepared on a glow-discharged carbon foil and stained with 1 % uranyl acetate (see 2.2.4.4).

Circular dichroism (CD): The average secondary structure of monomeric α S, fibrils and dissociated fibrils was determined as described in 2.2.4.3.

Immunoblotting (dot blotting): Amyloid fibrils, oligomers and wt α S were spotted onto nitrocellulose membrane as described in 2.2.2.8.

Lipid bilayer experiments: Lipid bilayer membranes were performed as described in 2.2.2.9.

4.3. Results and discussion

4.3.1. Dissociation of α -synuclein fibrils in supercooled water

After aggregation, TEM showed regular fibrils with a diameter of ~ 40 nm (Fig.4.2.a, right panel) and a strong ThT fluorescence signal was detected (Fig.4.3.b). 2D ^1H - ^{15}N HSQC spectra showed no visible cross peaks in agreement with the large molecular weight of amyloid fibrils that makes it beyond detection limit in solution-state NMR (Fig.4.2.a, left panel). To probe the stability of α S fibrils at the temperature below 0°C , we employed supercooled water. ^{15}N -labeled α S fibrils were injected into glass capillaries as described above (see 2.2.2.6).

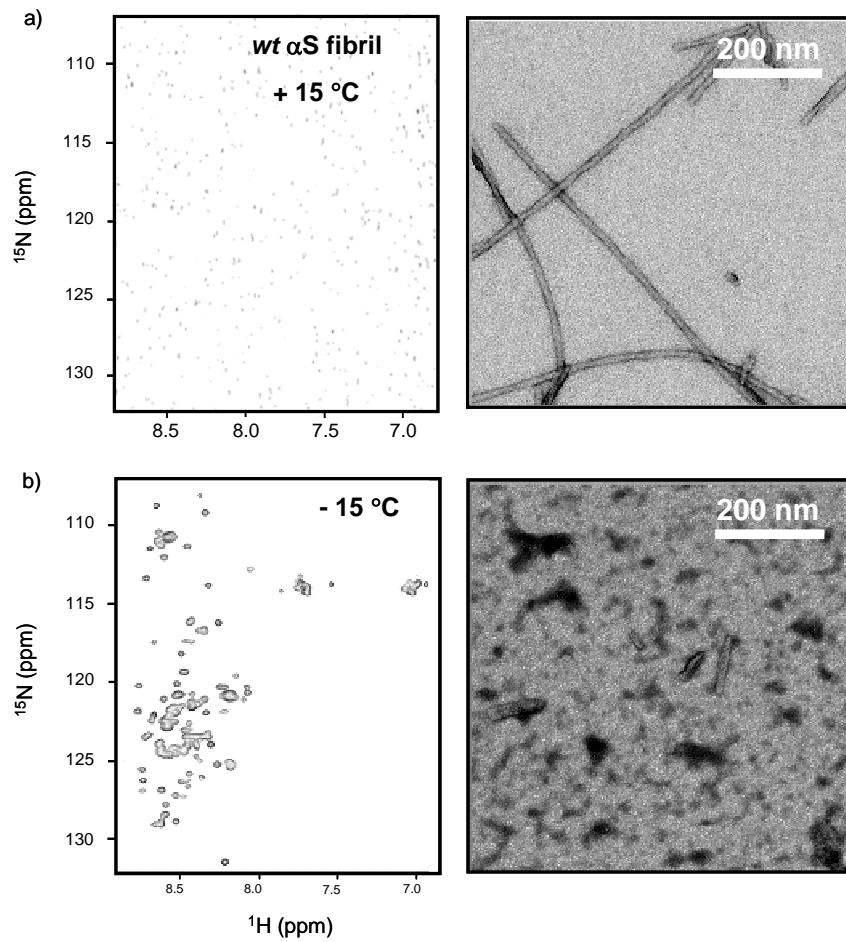


Figure 4.2: Cold dissociation of ^{15}N -labeled αS fibrils in supercooled water at $-15\text{ }^\circ\text{C}$. 2D ^1H - ^{15}N HSQC spectra and electron micrograph of a sample containing ^{15}N -labeled αS fibrils in physiological buffer, a) $+15\text{ }^\circ\text{C}$ and b) after keeping it at $-15\text{ }^\circ\text{C}$ for 1 day.

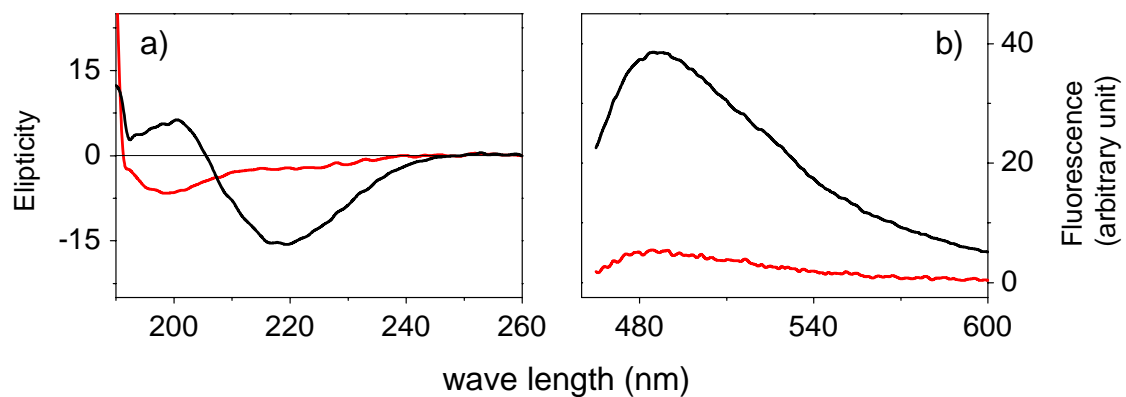


Figure 4.3: a) CD spectra and b) ThT fluorescence of αS fibrils (black) and after one day of incubation in supercooled water at $-15\text{ }^\circ\text{C}$ (red).

Subsequently, the NMR tube was incubated at $-15\text{ }^{\circ}\text{C}$ for 1 day in a vibration free environment of a NMR spectrometer. After incubation, TEM images, CD, ThT fluorescence and 2D ^{15}N - ^1H HSQC spectra were measured. TEM images showed disordered aggregates and rare fibrillar structures (Fig.4.2.b, right panel). CD spectra showed no β structural propensity and ThT no longer bound to the protein as monitored by fluorescence (Fig.4.3.a, b). In the HSQC spectrum, a large number of cross peaks appeared. The cross peak pattern of the spectrum was highly similar to that of freshly prepared ^{15}N -labeled monomeric αS under the same conditions (i.e. same buffer conditions at $-15\text{ }^{\circ}\text{C}$).

4.3.1.1. Dissociation followed by real-time 2D ^1H - ^{15}N HSQC NMR

To obtain insight into the dissociation kinetics of αS fibrils, real time NMR spectroscopy was employed. After incubations the fibrils at $-15\text{ }^{\circ}\text{C}$, a series of HSQCs were acquired for 30 hours (Fig.4.4.a). Residue specific changes in intensities of cross peaks were extracted and fit to a sigmoidal function of time. From the fit a half time dissociation of 3.3 hours averaged over all residues were obtained. The steady state was approached after more than 30 hours. Similar results were obtained when analysing the increase of aliphatic signals in 1D ^1H spectra.

A residue specific analysis of the time series of HSQCs revealed that signals of residues 96-140 increased rapidly than cross peaks of other residues (Fig.4.4.b, c). The difference may be caused by the fact that C-terminal residues, which were shown to be flexible in amyloid fibrils, are also flexible in species formed during cold dissociation. Thus, while residues 1-96 are still too immobile in multimeric forms of dissociation intermediates to be observed by solution-state NMR, residues in the C-terminal domain

can already contribute to the observed signal. Note that the kinetics as well as the temperature required for cold denaturation of amyloid fibrils is expected to depend on pH and buffer composition.

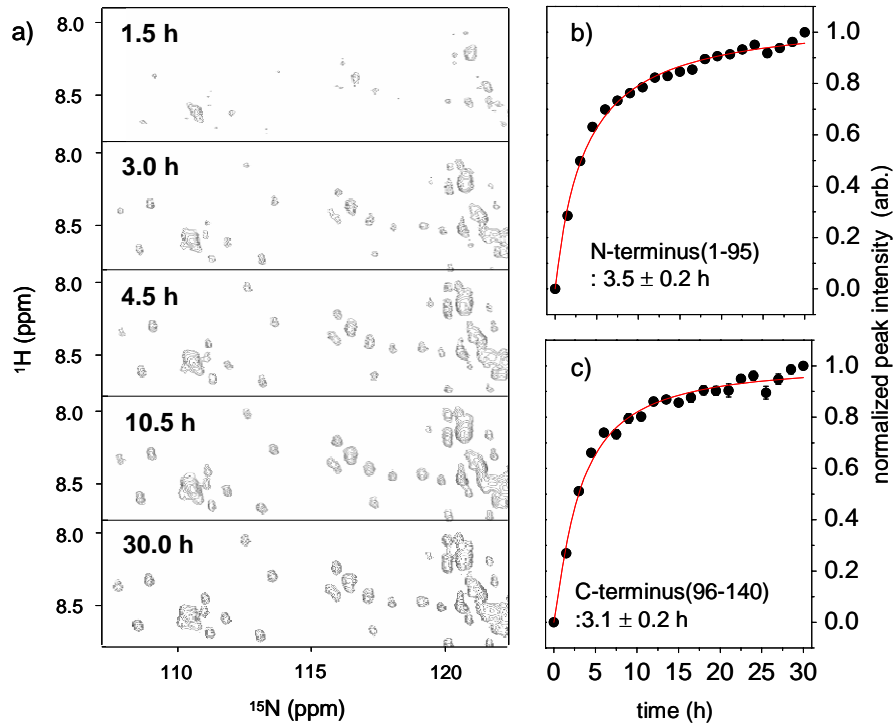


Figure 4.4: Dissociation followed by real-time NMR. a) 2D ^1H - ^{15}N HSQC spectra recorded during cold dissociation of ^{15}N -labeled αS fibrils in supercooled water at -15°C . Residue specific duration at which half of the final signal intensity was reached in 2D ^1H - ^{15}N HSQC spectra during cold dissociation of αS fibrils. b), c) Average increase in signal intensities of residues 1-95 and residues 96-140, respectively. The solid line indicates a sigmoidal function to the experimental data.

4.3.1.2. Comparisons of biophysical properties: dissociated and native monomer of α -synuclein

In Figure 4.5, superposition of ^1H - ^{15}N HSQC spectra of monomeric αS and of a sample that initially contained ^{15}N -labeled αS fibrils and had been incubated in

supercooled water $-15\text{ }^{\circ}\text{C}$ for one day are shown. Both spectra were acquired at $-15\text{ }^{\circ}\text{C}$ with a particular sequence of magnetic pulses and time delays which allows the transfer of magnetization between amide protons and the amide nitrogens of amino acids, and detects the resonances corresponding to the H-N amide bond of each residue in the polypeptide chain (including amino acids side chains and excepting Pro which does not contain any amide proton). No significant differences were observed indicating that the NMR signals detected after incubation of the amyloid fibrils at $-15\text{ }^{\circ}\text{C}$ originate from monomeric α S. Changes in the chemical environment surrounding a particular amino acid can thus be efficiently evaluated by means of intensities or chemical shifts perturbations on resonances of amide protons (Fig.4.6.a). The chemical shift differences and the relative signal intensity were analyzed between the monomeric protein and the sample that originally contained amyloid fibrils and had been incubated in supercooled water for one day (Fig.4.6.b).

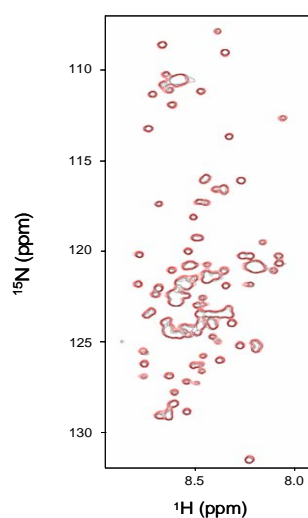


Figure 4.5: Superposition of ^1H - ^{15}N HSQC spectra. Monomeric α S (black) and of the sample (red) that initially contained ^{15}N -labeled α S fibrils and had been incubated in supercooled water at $-15\text{ }^{\circ}\text{C}$ for one day (red). Both spectra were recorded at $-15\text{ }^{\circ}\text{C}$.

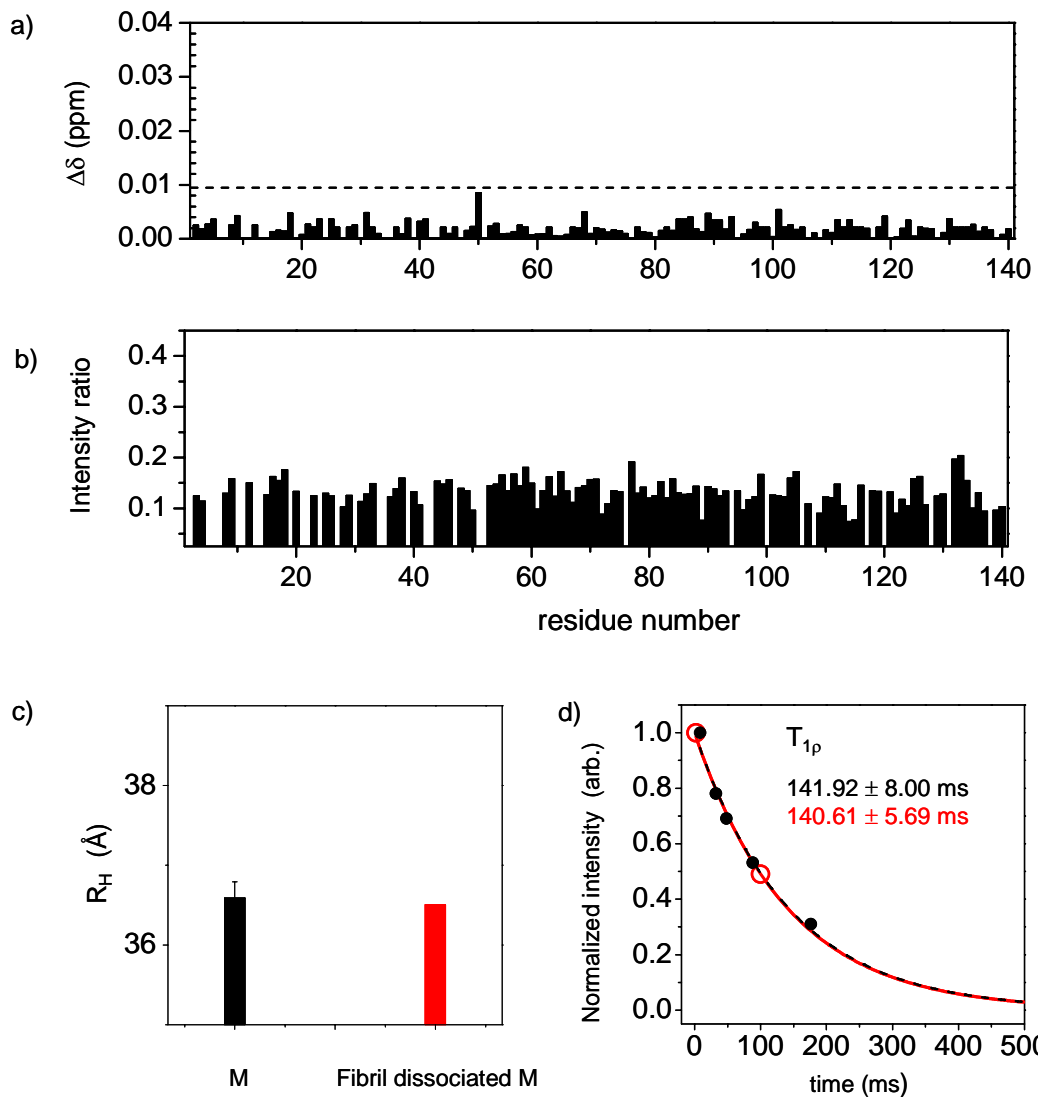


Figure 4.6: Comparison of the properties of α S signals observed after dissociation of ^{15}N -labeled fibrils in supercooled water (at $-15\text{ }^\circ\text{C}$ for 1 day) with those of freshly prepared monomeric α S at $-15\text{ }^\circ\text{C}$. a) Hydrodynamic radius values of monomeric α S (black) and of the NMR signals observed after cold dissociation of α S fibrils (red). b) Average decay of amide proton signals in ^{15}N $T_{1\rho}$ relaxation time experiments (red: signals observed after cold dissociation of fibrils, black: monomeric). Solid lines represent exponential fits to the data. c) Normalized average ^{15}N and ^1HN chemical shift differences calculated according to $\Delta_{\text{av}}(\text{NH}) = [(\Delta\text{H}^2 + (\Delta\text{N}/5)^2)/2]^{1/2}$. d) Ratio of peak intensities between NMR signals obtained from cold dissociation of ^{15}N -labeled fibrils and monomeric α S.

In addition, ^{15}N $T_{1\rho}$ relaxation times measurement and pulse field gradient NMR experiments were performed to further characterize the protein in the two samples of both samples. For both monomer and monomer dissociated from fibrils, a hydrodynamic radius of 36.6 Å, 36.5 Å were obtained respectively, at $-15\text{ }^\circ\text{C}$ (Fig.4.6.c). Average decay of amide proton signals in ^{15}N $T_{1\rho}$ relaxation time experiments showed very similar for both samples (Fig.4.6.d), indicating that monomer dissociated from α S fibrils has comparable time. Thus, monomer dissociated form α S fibrils has highly similar structural properties as the native monomer α S.

4.3.1.3. Which interactions hold α -synuclein fibrils together?

Analyses of amyloidgenic peptides demonstrated that amyloid fibril structures are highly hydrogen bonded, nearly anhydrous and densely packed β -sheets^[101, 107]. In addition, hydrophobic and electrostatic interactions can contribute to the stability of amyloid fibrils^[108]. All of these interactions are strongly temperature dependent: protonation of protein groups increases at decreasing temperature (ionization of essential groups with decreasing temperature) and hydrophobic interactions decrease with decreasing temperature^[36]. Additionally, the properties of water itself and the way it interacts with polypeptides are strongly temperature dependent^[109].

Why do low temperatures destabilize amyloid fibrils? To obtain evidence for the attenuation of electrostatic and hydrophobic interactions at low temperatures, we investigated the conformational properties of monomeric α S in supercooled water using NMR paramagnetic relaxation enhancement (PRE)^[110]. By incorporation of paramagnetic spin labels in different regions of the sequence, it was previously shown

that the ensemble of conformations populated by monomeric α S at +15 °C is stabilized by intramolecular long-range interactions [53, 111].

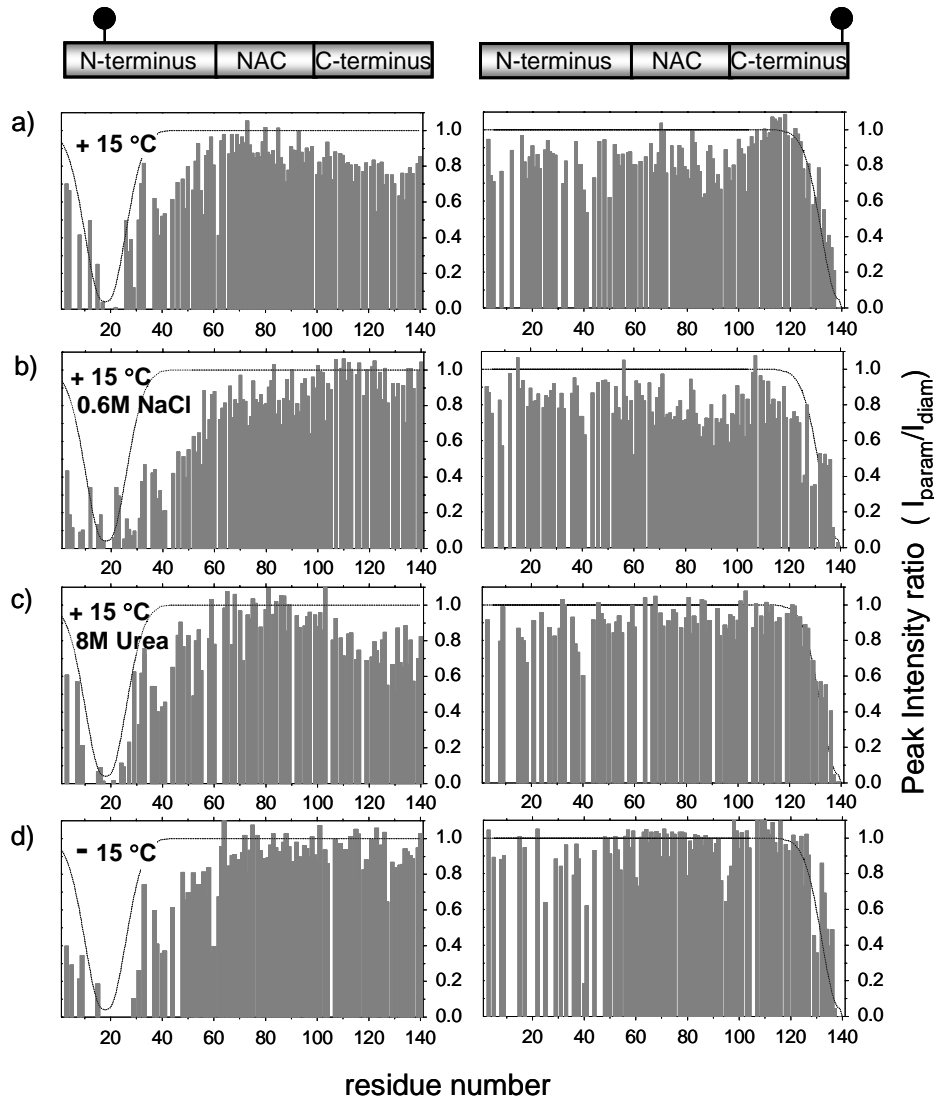


Figure 4.7: PRE of α S. Intensity ratios ($I_{\text{param}}/I_{\text{diam}}$) of cross peaks in ^1H - ^{15}N HSQC spectra recorded in the presence (paramagnetic) and the absence (diamagnetic) of the spin label MTSL attached to position A18C or A140C in buffer at a) +15 °C, b) in the presence of 0.6 M NaCl at +15 °C, c) upon addition of 8 M urea at +15 °C and d) in buffer at -15 °C. Dotted lines indicate intensity ratios expected for a fully extended structure.

In particular, transient long-range interactions exist between the positively charged N-terminus and the negatively charged C-terminus (Fig.4.7.a, left panel). Moreover, signal broadening was observed in the hydrophobic central domain between residues 70-105 when a spin label was attached to residue 140 (Fig.4.7.a, right panel). Changes in the PRE profile upon addition of 0.6 M NaCl (Fig.4.7.b), addition of 8 M urea (Fig.4.7.c) and decrease of temperature to $-15\text{ }^{\circ}\text{C}$ (Fig.4.7.d) was then studied. In the presence of 0.6 M NaCl, the spin label at position 18 no longer caused signal broadening in the C-terminus (Fig.4.7.b, left panel) suggesting that the interaction between the N- and C-terminal domains is electrostatically driven.

On the other hand, the broadening that was observed for residues 70-105 when the spin label was attached to residue 140 was not reduced (Fig.4.7.b, right panel). The opposite effect was observed when 8 M urea was added: the PRE profile observed for A18C was not changed, whereas signals in the central domain were no longer broadened (Fig.4.7.c, right panel). This suggests that long-range interactions probed by the A140C-MTSL protein are mainly related to hydrophobic interactions. At $-15\text{ }^{\circ}\text{C}$, both long-range broadening effects were removed indicating that hydrophobic and electrostatic interactions were attenuated (Fig.4.7.d).

To gain insight into the importance of hydrophobic and electrostatic interactions for the stability of α S fibrils, ^{15}N -labeled fibrils was exposed to 8 M urea and 0.6 M NaCl. TEM and NMR spectroscopy showed that α S fibrils are fully dissociated into monomeric protein in 8 M urea (Fig.4.8.a). In 0.6 M NaCl, the morphology of fibrils was changed as observed by TEM. Fibrils were fragmented and less regular. Also, cross peaks of some residues (mainly C-terminus, e.g. N122, E137, E139 and A140) appeared in the HSQC spectrum, indicating that α S fibrils are destabilized by increased ionic

strength (Fig.4.8.b). Noteworthy, exposure of α S fibrils for 16 hours to +95 °C did not reduce ThT fluorescence and TEM images showed a comparable amount of fibrils before and after incubation (Fig.4.9), indicating that mature amyloid fibrils of α S are highly resistance to high temperatures ^[101, 102].

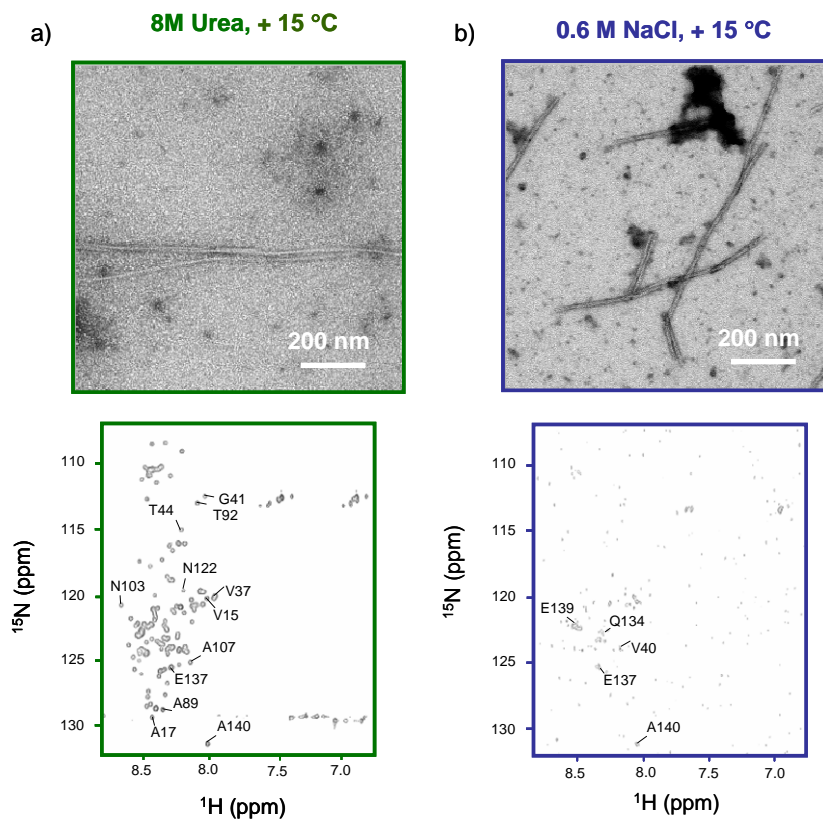
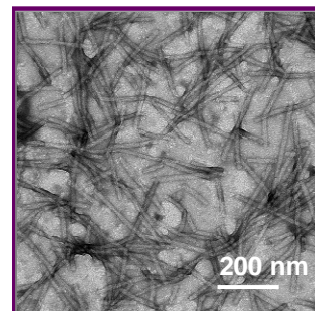


Figure 4.8: TEM and HSQCs. Electron micrographs and 2D ^1H - ^{15}N HSQC spectra of a sample that contained initially α S fibrils (see Fig.4.1) after a) addition of 8 M urea and b) 0.6M NaCl (both at +15 °C). Selected cross peaks are labeled with their assignment.

Figure 4.9: TEM image of α S fibrils incubated overnight at +95 °C. Buffer conditions were identical to those used for cold dissociation.



4.3.2. Characterization of α -synuclein oligomers derived from amyloid fibrils through supercooled water

Real-time aggregation by NMR and AFM experiments were done by Min-Kyu Cho, amyloid fibrils dissociation by NMR, ThT fluorescence emission, native gel electrophoresis and antibody assay were performed by myself.

4.3.2.1. Quantification of oligomers

The dissociation was confirmed by TEM, NMR, and ThT fluorescence. Intriguingly, TEM of the dissociation shows dark and crowded background that was not observed in TEM of amyloid fibrils (Fig.4.2.b, right panel). The amount of the dissociated monomer was determined as ~15 % by NMR together with ~30 % remaining of fibril, indicated that there must be another species which remains undetected by NMR and ThT. This species with high molecular weight probably oligomers, and further characterization has been performed.

Quantitative analysis for the oligomers derived from cold-induced dissociation of amyloid fibrils is shown in Figure 4.10. After one week of amyloid fibril aggregation of ^{15}N -labeled wt α S, the intensity of the cross-peaks in 2D ^1H - ^{15}N HSQC spectra showed that ~15 % of monomers remain in the solution (I) compared to the initial intensity. The remaining monomers were removed and then the collected amyloid fibrils were used for the dissociation. After two days of dissociation in supercooled water, (II) the signal intensity of the dissociated monomer in ^1H - ^{15}N HSQC was compared with that of the initial monomer sample prior to aggregation and (III) ThT signal of the remaining amyloid fibril was compared with that of the initial fibril before the dissociation. Based on both quantifications (II, III), it is revealed that ~15 % of ^{15}N α S

exist as monomer after cold dissociation (II), ~20-30 % as amyloid fibril, and the remaining 50-60 % as oligomers (IV).

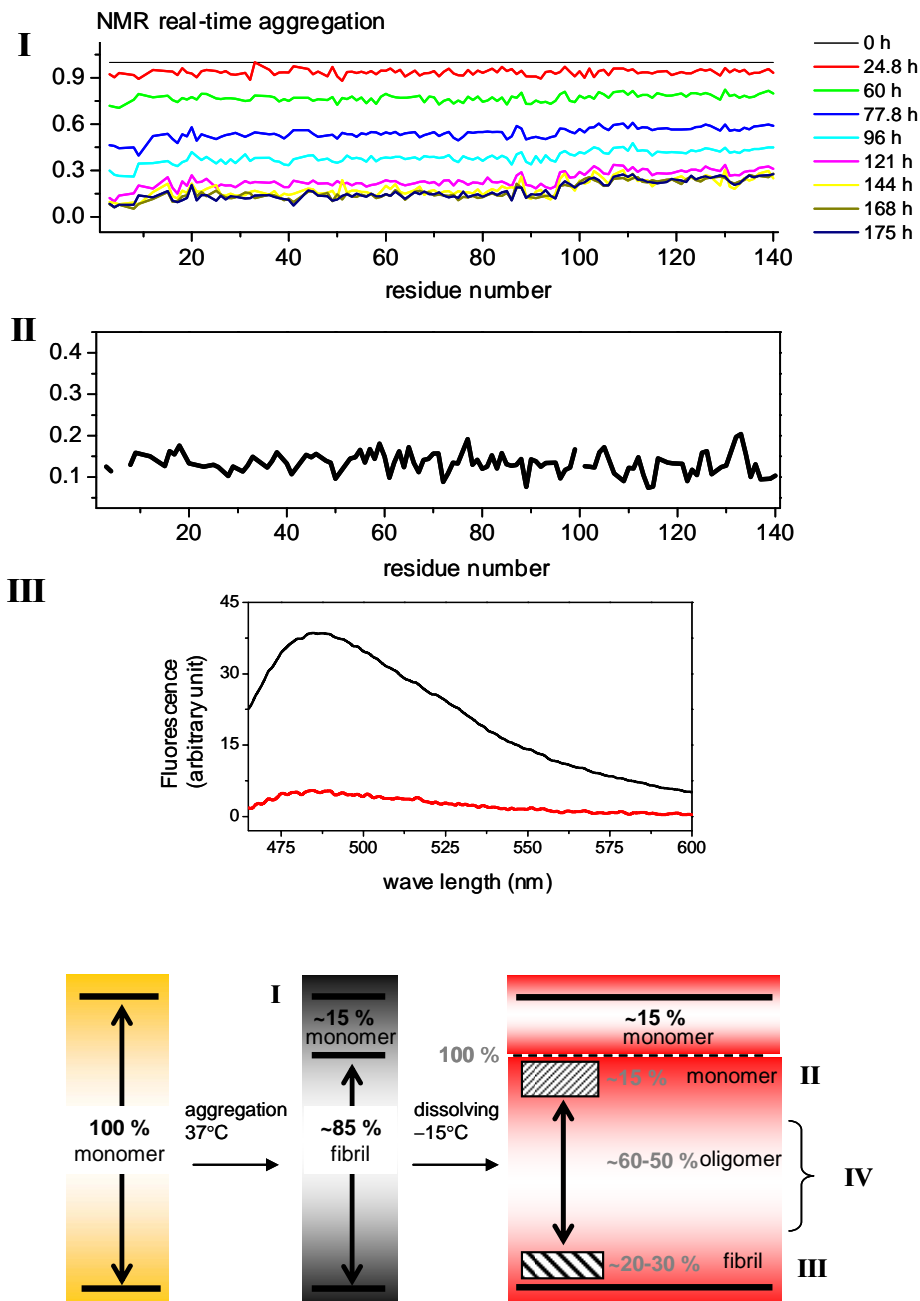
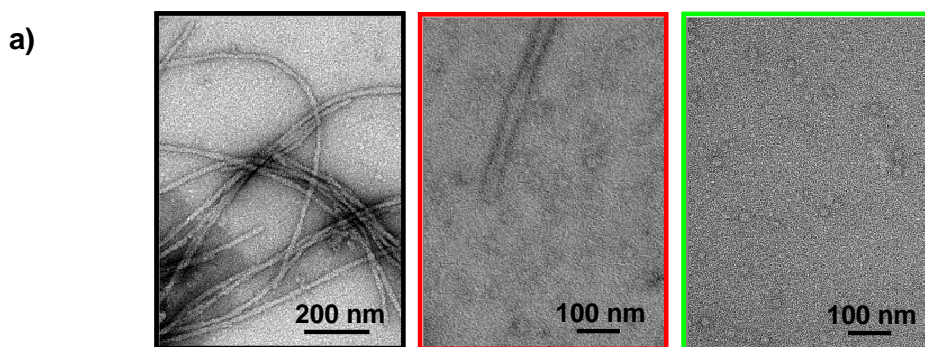


Figure 4.10: Quantitative analysis of the dissociated oligomer (O_{cold}). The overall changes of the amount of all species are described in top panel. The quantification was done by: I, the remaining monomer signal intensity in NMR; II, the dissociated monomer intensity in NMR; III, ThT fluorescence of the remaining fibril after dissociation.

4.3.2.2. Morphology of the oligomers

To define the structural properties of the oligomers, obtained by cold dissociation, microscopic images were acquired. Prior to the characterization, the oligomers had to be separated from the fibril that hampers clear view of smaller species. Centrifugation for 15 min at 13,200 g and careful aliquot of the upper 50 % of the supernatant was sufficient to make an oligomer sample free from protofibrils. TEM images and ThT fluorescence of fibrils, dissociated fibrils and oligomers are shown in Figure 4.11.

The fibrils has typical morphology of amyloid fibril (left in Fig.4.11.a) while TEM of the cold dissociated fibril sample shows a mixture of protofibrils and spherical oligomers (middle in Fig.4.11.a). After purification, a clearer image of spherical oligomers was obtained (right in Fig.4.11.a). The spherical species are categorized into two types based on their diameter, 15-20 nm and 20-30 nm, which were earlier observed as the diameter of oligomers ^[112, 113]. ThT fluorescence emission has been used to detect the cross- β structure content in amyloid fibril. ThT emission decreased down to ~ 20 % of the initial values after the incubation at -15 °C and there was no ThT fluorescence signal from the purified oligomers implying that oligomers have no cross- β structure (Fig.4.11.b).



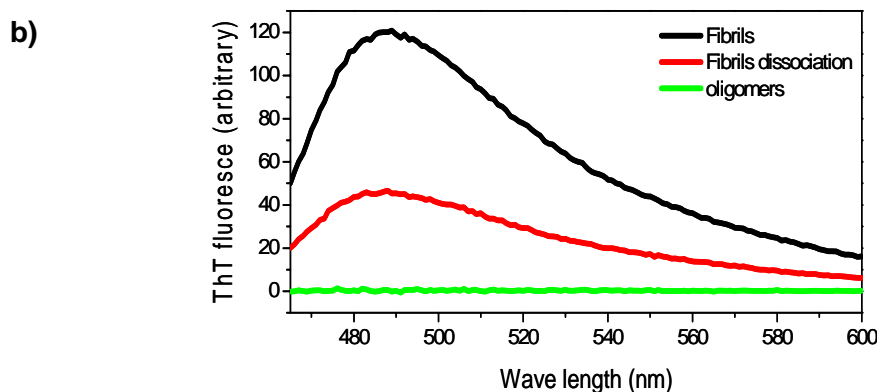


Figure 4.11: TEM images and ThT fluorescence of α S fibrils and α S oligomers. a) TEM images of α S fibrils (black), after one day of incubation in supercooled water at -15 °C (red) and of the supernatants after centrifugation for 15 min at 13,200 g (green) in 50 mM Naphosphate buffer, pH 7.4, 300 mM NaCl. b) Thioflavin-T fluorescence signals.

4.3.2.3. α -synuclein oligomers are on-pathway to fibril formation

The finding of the oligomers in supercooled water led us to explore the role of the oligomers in protein aggregation and pathology of PD. First, we verified whether the dissociated fibrils are able to reassemble into amyloid fibrils. Figure 4.12 shows the overall procedure consisting of aggregation, dissociation, and re-aggregation. During the normal aggregation assay, there was a reduction in the half time for α S monomer due to the higher salt concentration (left panel in Fig.4.12). After dissociation in supercooled aqueous solution for 1 day, ThT fluorescence signal intensity dropped down to ~ 20 % (middle panel in Fig.4.12). The solution was collected and incubated again at 37 °C with stirring. Notably, the lag time was nearly diminished in re-aggregation step, and ThT fluorescence reached to saturation point faster than the normal aggregation step (right panel in Fig.4.12), which implies that the mixture derived from the amyloid fibrils in supercooled solution can aggregate into amyloid fibril more rapidly than monomer does.

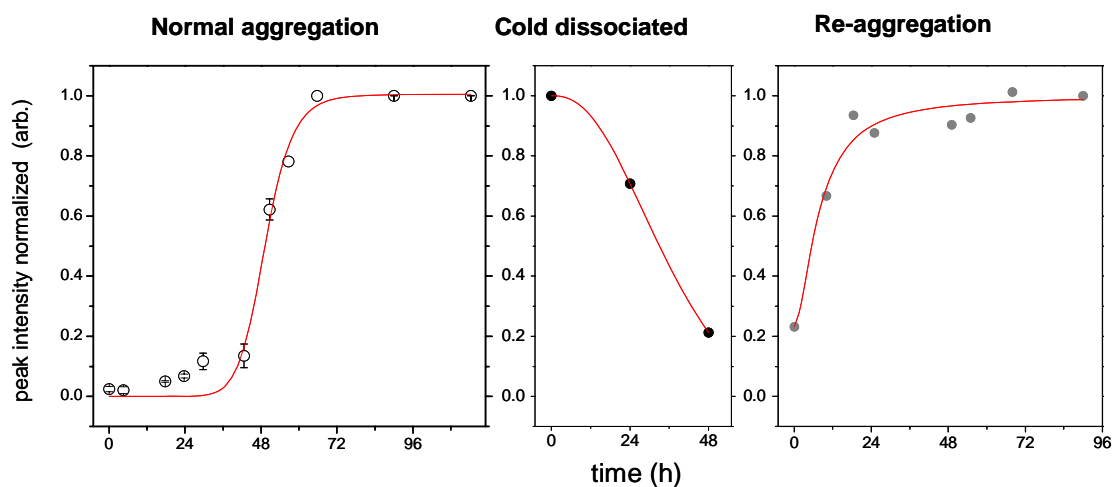


Figure 4.12: α S aggregation and re-aggregation procedure. Aggregation assay for α S. All experiments were done in 50 mM Na-phosphate buffer pH 7.3, 300 mM NaCl. Normalized ThT traces for the monomer (left), increased salt concentration reduces half time for aggregation. After 1 day incubation at -15 °C, ThT intensity drops due to the dissociation of the fibril (middle). When the solution containing the mixture which promotes fibril formation faster than normal aggregation (right).

Since this mixture contained monomers, oligomers and protofibrils, further purification was needed to verify the effect of the oligomers on aggregation. The purification of the oligomers was performed with a series of centrifugation steps (Fig.4.13). First, fibril fragments or protofibrils were removed by centrifugation at 5,000 rpm for 15 min in a table-top centrifuge. Upper 50 % of supernatant was taken and further centrifuged 65,000 rpm for 3 hours. After removing 70 % of upper supernatant in order to reduce the monomer concentration, the remaining 15 % of solution in the centrifuge tube was stored for the seeding experiment. The amount of the oligomers in the final solution, terms of monomer concentration was, expected to maximum ~ 500 μ M with an assumption that the oligomers remained without any loss during the purification.

The purified oligomer solution was added into the freshly prepared α S monomer solution: 13 μ l of the oligomer solution into 500 μ l of 100 μ M α S monomer solution. The total amount of α S in monomer concentration should be maximum \sim 113 μ M in 513 μ l. The aggregation profile of the oligomers-seeded α S solution was recorded with time-course of ThT fluorescence emission. As a reference, 100 μ M α S monomer solution without the oligomers was prepared and incubated in the same way.

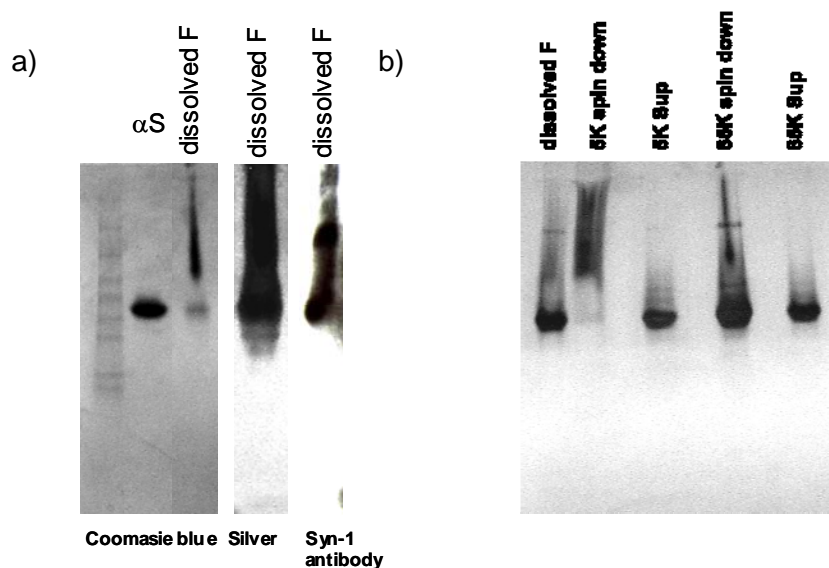


Figure 4.13: Purification of oligomers derived from fibril dissociation. a) Native gel result of the upper 50 % of supernatant after 5,000 rpm centrifugation. Gel is stained with Coomassie blue and silver. Syn-1 antibody stained after Western blot. b) Native gel result of 65,000 rpm centrifugation (F: fibril, Sup: supernatant, spin down: remains part after removing supernatant).

ThT intensities increased in a sigmoidal manner after a lag phase indicating the formation of fibrils. The overall comparison of both profiles is shown in Figure 4.14. The oligomer-seeded α S monomer aggregated to amyloid fibril 2-fold faster, and in

particular, the lag time was considerably shorter than the control. As the α S fibrillization is proposed to occur in a sequence of nucleation, elongation and maturation [17, 84], the short lag time suggests that the role of the oligomers should be an on-pathway intermediate that promotes protein fibrillization. The seeding capacity of the oligomers is extremely high as the oligomer and monomer mixture solution rapidly formed fibrils even at 4 °C without stirring as probed by ThT fluorescence emission in Figure 4.15.

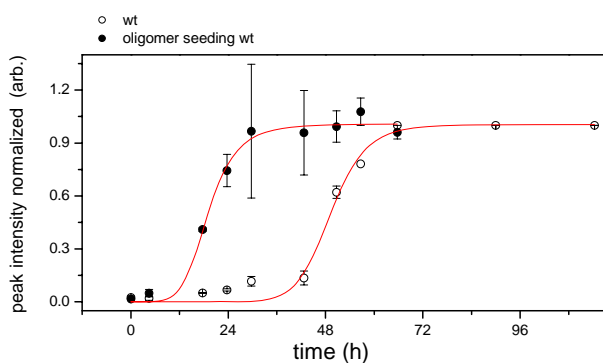


Figure 4.14: Kinetic properties of the oligomers seeding experiments. The purified oligomer 13 μ l added to 100 μ M α S monomer solution. The oligomer accelerates α S fibrillization. The half time in seeding (~24 h) is substantially shorter than without seeding (~48 h). The purified oligomers promote fibrils formation. .

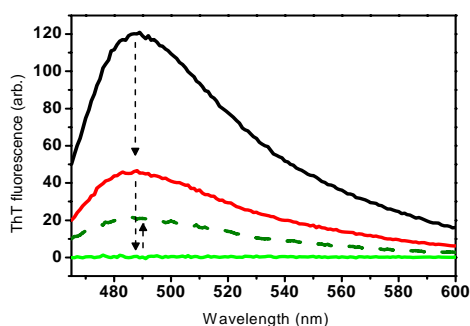


Figure 4.15: ThT fluorescence emission change of α S in different conformations. The highest ThT intensity of α S fibril (black) goes down after 1 day incubation in supercooled solution (red). Centrifugation at 5,000 rpm removes remaining fibril and leave monomer and the oligomers (green). After stored three days at 4 °C, ThT signal arises (dark green).

4.3.2.4. Toxicity induced by membrane pore formation

Pathogenic role of protein oligomers in neurodegenerative diseases has been studied and proposed that it interacts with membrane and develops membrane pores with non-selective leakage of compounds [19, 114, 115]. Membrane permeabilization by α S oligomers also has been considered to be a ubiquitous example of the action of an amyloid pore which has been proposed to underlie a mechanism common to neurodegenerative disease pathogenesis [115-117]. With the knowledge of the oligomers shape with TEM and AFM, we extended the functional study of the oligomers *in vitro*.

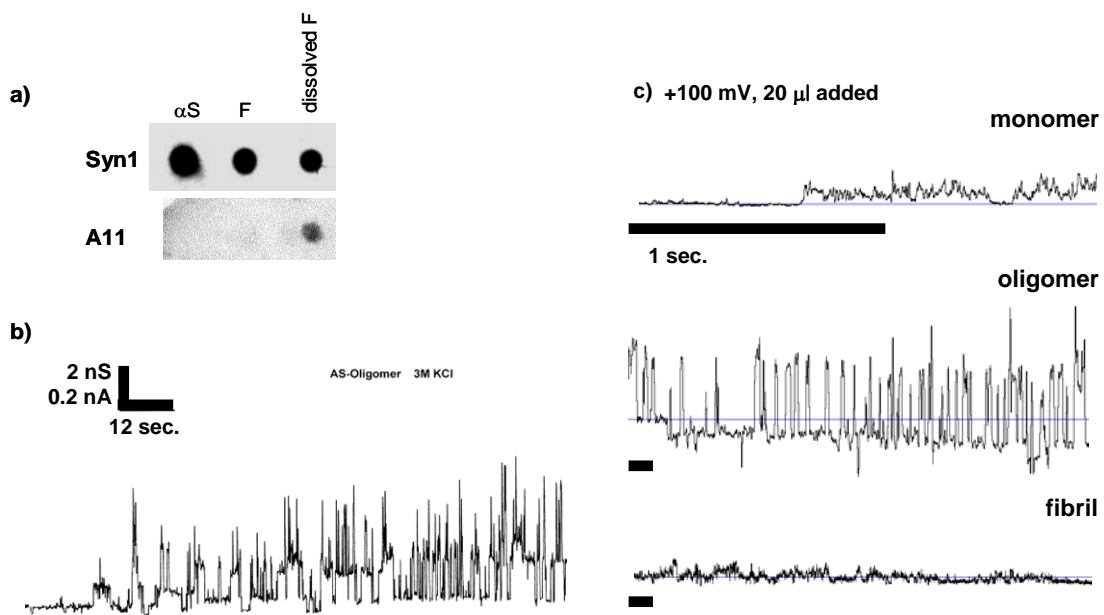


Figure 4.16: A11 antibody assay and black lipid bilayer membrane (BLM) experiment. a) α S monomer, fibrils and the oligomers derived from supercooled water are deposited on to a nitrocellulose membrane and probed with the oligomer-specific antibody-A11 and the α S-specific antibody, Syn1. b) The oligomers induce conductance through the lipid bilayer with 3 M KCl, 1 % DiphPC, +100 mV. The oligomers were added to the cis compartment to a final concentration of 2-10 μ g/ml. Bilayer currents were recorded as described [63]. c) Only the oligomer solution shows channel-like conductance through BLM.

Previous studies suggested that A11-antibody developed to target the earlier-stage spherical intermediate of A β , recognizes subfibrillar aggregates of various amyloid proteins, which induce membrane permeabilization [62]. Dot-blotting results of the oligomer with A11 antibody showed that the oligomers are recognized by A11 antibody (Fig.4.16.a) implying that the structures of the oligomers share the common conformation with those intermediates and the function in neurotoxicity of amyloidogenic misfolding proteins.

Together with the conformational characterization by A11 antibody, the membrane permeability of the oligomers was investigated with physiology experiment with black lipid bilayer membrane system [63]. Figure 4.16.b shows the conductance of planar lipid bilayer membranes containing 3 M KCl, 1 % DiphPC, which reveals that the oligomers are able to induce leakage of electrolytes through the bilayer membrane. The conductance of the pore induced by the oligomers exhibited, like channel protein, several conductance states with well defined amplitude in every trial, but the absolute size of the channels varied in different trials. The major conductance state of the oligomers was averaged to 600 pS (the net conductance of the larger channels was 1400-1700 pS). Intriguingly, Zakharov *et al.* reported that monomeric α S can produce ion channels in membranes containing an optimum anionic lipid content and proposed that the formation of α -helical channels provide an alternative mechanism for membrane permeabilization [117]. Together with the channel formation by oligomer species, those physiological data show a potential mechanism of toxicity induced by misfolding proteins, *in vivo*.

4.4. Conclusion

Taken together, our data suggests that –although we currently cannot estimate the relative importance of the various contributions– the temperature dependence of hydrophobic and electrostatic interactions contribute to the cold denaturation of α S fibrils. We have demonstrated that amyloid fibrils formed by the protein α S are rapidly denatured, that is, dissociate and lose the conformation of its constituent proteins molecules, in supercooled water at -15 °C. Thus, the stability of α S fibrils towards low temperature is low compared to the transition temperatures commonly found for globular proteins. This resembles the situation found for other supramolecular assemblies such as microtubules that dissociate upon cooling^[118].

In addition, the incubation of amyloid fibrils in supercooled solution appeared to be an effective tool to get a high amount of oligomers even though the oligomers are heterogeneous mixture. Together with the morphology study, the role of the oligomers both in amyloid fibrils formation and in membrane physiology was investigated. It was revealed that the oligomers promote fibril formation suggesting that the oligomers are on-pathway intermediates in fibrillization. The intermediate role and the heterogeneity of the oligomers support the mechanism of the oligomer-based concerted amyloid fibril formation. Also, the potential toxicology of the oligomers, known to be related with channel activities (membrane permeabilization), was demonstrated by BLM physiology experiment.

4.5. Outlook

For a better understanding of the cold denaturation of amyloid fibril, we are extending our study to other systems including A β , lysozyme, β 2microglobulin and C-terminus truncated α S (108). In parallel, to extend our knowledge about the oligomers in atomic resolution, study of oligomers by solid-state NMR, electron paramagnetic resonance (EPR) spectroscopy, and hydrogen/deuterium exchange coupled with NMR is in progress. Furthermore, the toxicity of the oligomers is being assayed with primary neuronal culture. All these information would provide a conceptual framework for which therapeutic strategies could be developed to take care of various amyloidosis-related diseases.

5. Biophysical studies of α -synuclein phosphorylation and its aggregation

5.1. Introduction

Increasing evidence suggests that phosphorylation may play an important role in the oligomerization and fibrillogenesis^[119], LBs formation^[119, 120] and neurotoxicity of α S *in vivo*^[121]. Immunohistochemical and biochemical studies revealed that the majority of α S within LBs from patients with PD and other synucleinopathies like multiple system atrophy (MSA)^[119, 120, 122, 123] is phosphorylated at S129 (S129-P). Proteinaceous inclusions formed in cellular and animal models overexpressing wt or mutant α S^[121, 123-125] can also be stained with an antibody against S129-P. A study by Fujiwara *et al.* reported that *in vitro* phosphorylated α S, at S129 using Casein Kinase II (CK2), forms fibrils more readily than unmodified α S^[119]. Phosphorylation at S129 was also reported to promote the formation of cytoplasmic inclusions in some cell culture models of synucleinopathies^[126]. Together, these findings suggested that phosphorylation at S129 plays an important role in modulating α S aggregation, LBs formation and toxicity *in vivo*. However, whether phosphorylation promotes or inhibits α S aggregation and neurotoxicity *in vivo* remains unknown. This understanding is critical for elucidating the role of α S in the pathogenesis of PD and for development of therapeutic strategies for PD.

Furthermore, the kinases and phosphatases responsible for regulating α S phosphorylation *in vivo* are still not known. A series of *in vitro* and cell culture-based

studies have identified a number of kinases, which phosphorylated α S at S129 and/or S87. Okochi *et al.* [127] demonstrated that α S undergoes constitutive phosphorylation by casein kinase 1 (CK1) and CK2 *in vitro*. The same study also revealed that CK2 phosphorylates α S at S129, whereas CK1 phosphorylates at S129 and S87, with S129 being the major phosphorylation site. Similarly, Pronin *et al.* [128] showed that the G-protein coupled receptor kinases (GRKs), like GRK1, GRK2 and GRK5 and GRK6 can phosphorylate α S *in vitro*, with a preference for phosphorylation at S129.

A comparison of the amino acid sequences of all synucleins from humans and other species shows that the majority of potential α S phosphorylation sites, including Y125, S129, Y133 and Y136 are highly conserved in all species. Considering all the *in vitro* and tissue culture identified phosphorylation sites of α S, S87 [127, 129], S129 [119, 121, 123, 127-129], Y125 [123, 130-133], Y133 [130, 133] and Y136 [130, 133], it is striking that only S87 lies in the hydrophobic NAC region of α S, which is thought to drive the association and aggregation of α S [134]. S87 is also one of the few phosphorylation sites that are characteristic of human α S and distinguish it from mouse and rat α S, which have the PD associated mutation A53T, but do not cause PD-like pathology and symptoms in mice and rats. Therefore, phosphorylation at S87 potentially distinguishes the human α S from all other members of the synuclein family, which share a conserved Asparagine residue at this position and may contribute to the PD-like pathology and symptoms in human, but not mouse and rat α S.

5.2. Experimental procedure

During this work, protein aggregation assay *in vitro* and TEM were performed by Katrina E. Paleologou and Hilal A. Lashuel, at the Brain Mind Institute in Lausanne, Switzerland.

Cloning, expression, and purification of α S mutants: S129E, S129A and S87A α S mutants were generated using site-directed mutagenesis employing complementary internal mutagenic primers (see 2.1.3). Recombinant α S was expressed and purified as described in 2.2.2.1. except those used for SDS-micell condition NMR studies (see below).

Preparation of spin-labeled α S: A single cysteine residue was introduced into α S at position 18 (A18C) as described in 2.2.1.2 and 2.2.2.2.

NMR spectroscopy: NMR experiments were recorded on Bruker Avance 600 and 700 MHz NMR spectrometers. Pulse field gradient NMR experiments were measured for the determination of the hydrodynamic radius (see 1.4.4 and 2.3.3.3). The ^{15}N $T_{1\rho}$, ^1H $\{^{15}\text{N}\}$ -NOEs values were obtained by collecting five 2D spectra (see 2.2.3.4). An on-resonance spin-lock pulse of 2.5 kHz was used. PRE profiles were derived from the measurement of the ratios of the peak intensity between two 2D HSQC spectra in the presence (I_{para}) and absence (I_{dia}) of the nitroxide radical (see 1.4.3 and 2.2.3.2).

Phosphorylation of α S *in vitro*: wt or mutants α S was phosphorylated by CK1 (NEB) at concentrations of 1.446 mg/ml in the presence of 1.09 mM ATP (Sigma), 1x reaction solution supplied with the enzyme. The phosphorylation reaction was incubated at 30 °C for the stated time points and the reaction was stopped with ethylenediaminetetraacetic

acid (EDTA) disodium salt (5 mM final concentration) (Axon Lab). The progress of the reaction was monitored by RP-HPLC and mass spectrometry (see 2.2.2.3 and 2.2.2.5).

Fibrillization studies: To probe the effect of CK1 phosphorylation on the aggregation of α S, wt α S was phosphorylated for 24 h at 30 °C and the reaction was stopped with EDTA disodium salt before the samples were subjected to fibrillization conditions, at 37 °C with continuous shaking. The unphosphorylated controls were subjected to the same conditions, but in the absence of CK1. For fibrillization studies the proteins were dissolved in 20 mM Tris, 100 mM lithium chloride (Aldrich), pH 7.4, at a concentration of 70 μ M and fibril formation was monitored by ThT fluorescence.

Circular dichroism (CD): The average secondary structure of monomeric α S in the presence and absence of 1-Palmitoyl-2-Oleoyl-*sn*-Glycero-3-[Phospho-*rac*-(1-glycerol)] (Sodium salt) (POPG) (Avanti Polar Lipids Inc.) vesicles was determined by CD spectroscopy using a Jasco 810 Spectrometer. The Far UV-CD spectra (190-250 nm, integration time of 2 seconds for 0.2 nm) were collected at RT in a 1 mm path length quartz cuvette containing 0.1 mg/ml of α S in PBS or sodium phosphate buffer and vesicles were prepared as described in Paleologu *et al.* ^[135].

TEM: wt or mutant α S samples were deposited on Formvar-coated 200 mesh copper grids (Electron Microscopy Sciences) at a concentration of 25 μ M. Grids were washed with two drops of water and stained with two drops of freshly prepared 0.75 % (w/v) uranyl acetate (Electron microscopy sciences). Specimens were inspected on a Philip CIME 12 electron microscope, operated at 80 kV. Digitized photographs were recorded with a slow scan CCD camera (Gatan, Model 679).

5.3. Results and discussion

5.3.1. α -synuclein phosphorylation at S129

α S phosphorylation at serine129 (S129) is characteristic of PD and related α -synucleinopathies. Phosphorylation at S129 was also reported to promote the formation of cytoplasmic inclusions in some cell culture models of synucleinopathies^[126]. These findings suggested that phosphorylation at S129 play an important role in modulating α S aggregation, LBs formation and toxicity *in vivo*. However, whether phosphorylation promotes or inhibits α S aggregation and neurotoxicity *in vivo* remains poorly understood.

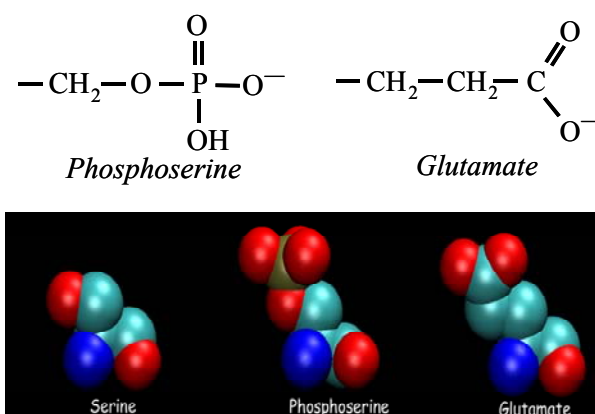


Figure 5.1: The atomic structures of the side chains of Glu and phospho-Ser demonstrate the structural and electrostatic similarities between the two moieties.

To understand better the role of the phosphate group in modulating α S aggregation, the structural and molecular properties of wt α S was compared to those of the phosphorylation mimics (S129E/D) and phosphorylation null mutants (S129A) as well. The structural and electrostatic similarities between Glu/Asp and phospho-Ser suggest that this type of substitution represents a reasonable approach to estimate

constitutive phosphorylation at a specific Serine residue (Fig.5.1). The phosphate moiety at pH 7 exists predominately in the fully deprotonated state, resulting in a net charge of -2, in contrast to the single negative charge contributed by Glu/Asp.

5.3.1.1. α -synuclein is disordered independent of phosphorylation

To elucidate the consequences of phosphorylation on the structure and dynamics of monomeric α S, high-resolution NMR studies were performed. For all proteins, the resonances in ^1H - ^{15}N HSQC spectra were sharp and showed only a limited dispersion of chemical shifts, reflecting a high degree of backbone mobility. Upon phosphorylation of wt α S by CK1, the resonances of S87 and S129 were strongly attenuated at the position seen in the HSQC of the unphosphorylated protein. Three-dimensional NMR spectra assigned the new signals to S87 and S129.

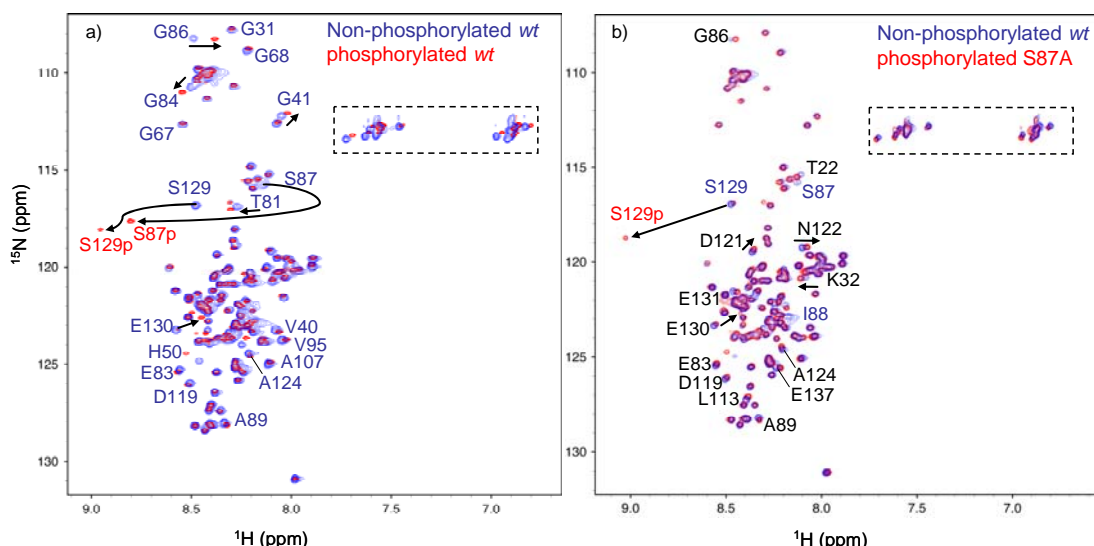


Figure 5.2: 2D ^1H - ^{15}N HSQC spectra. a) Comparison of ^1H - ^{15}N HSQC spectra of unphosphorylated wt (blue) and phosphorylated wt (red) α S. b) unphosphorylated S87A (blue) and phosphorylated S87A (red) α S. Resonance assignments are indicated with residue numbers. A dashed rectangle marks Gln and Asn side chain resonances.

At the same time, new signals appeared in the region, in which resonances of phosphorylated amino acids are usually found (Fig.5.2.a). It is known that CK1 phosphorylates α S at S87 and S129 [127, 128]. To block CK1-mediated phosphorylation at S87, the S87A mutant of α S was prepared as described in methods (see 2.2.2). NMR resonances in 2D ^1H - ^{15}N HSQC spectrum of phosphorylated S87A (S87A-P) α S were recorded at +15 °C. Chemical shifts in wt and S87A α S in the unphosphorylated form were highly similar except in direct vicinity of the mutation site. For S87A α S, phosphorylation at S87 was blocked such that only the resonance of S129 was attenuated at its original position and appeared at its phosphorylated position (Fig.5.2.b).

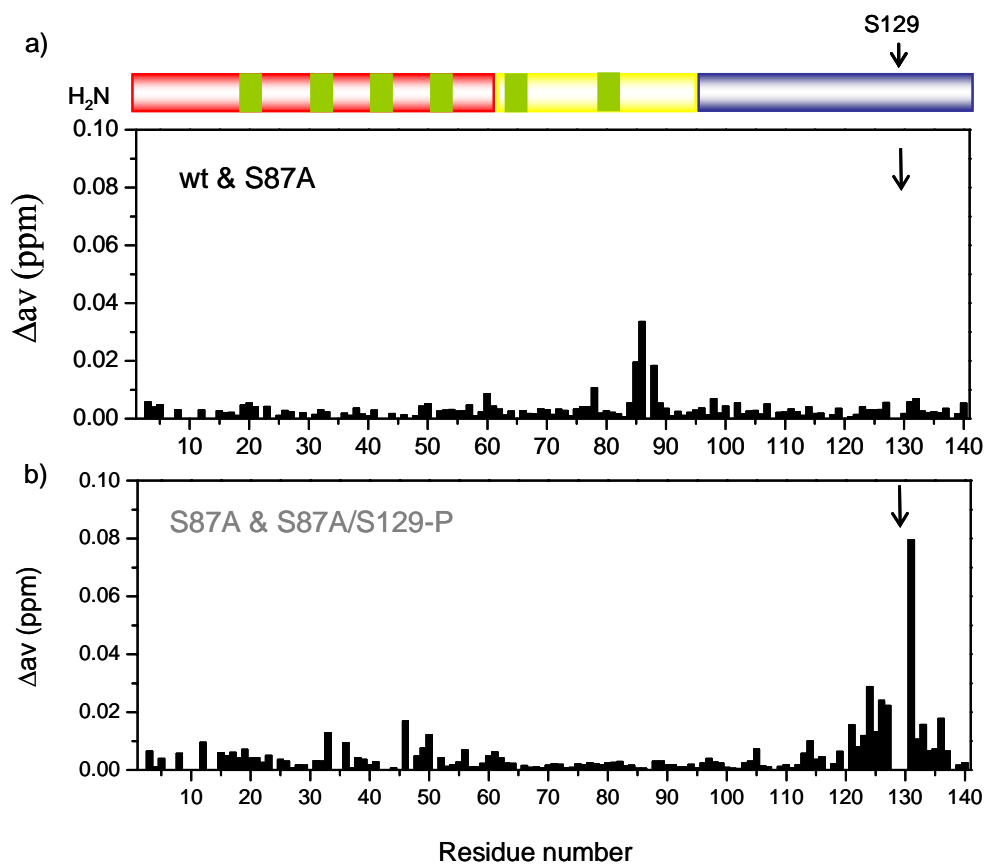


Figure 5.3: Normalized weighted average $^1\text{H}/^{15}\text{N}$ chemical shift differences a) between wt α S and S87A α S. b) between unphosphorylated and phosphorylated S87A α S.

Other chemical shift changes induced by phosphorylation were generally small. Detailed analysis, however, showed that the chemical shifts of residues down to residue 90 were influenced by phosphorylation of S129 in S87A α S (Fig.5.3.a). In addition, weak but significant chemical shift changes were observed for the 60 N-terminal residues in S87A α S (Fig.5.3.b), in agreement with recently reported by Sasakawa *et al.* [136].

5.3.1.2. Phosphorylation expands the ensemble of conformations populated by wt α -synuclein

Pulsed field gradient NMR experiments allow accurate determination of the diffusion coefficient of a molecule [57]. From the diffusion coefficient, a hydrodynamic radius R_H can be calculated that provides an estimation of the overall dimensions of a biomolecule. For wt α S, a hydrodynamic radius of 28.2 Å was obtained (Fig.5.4).

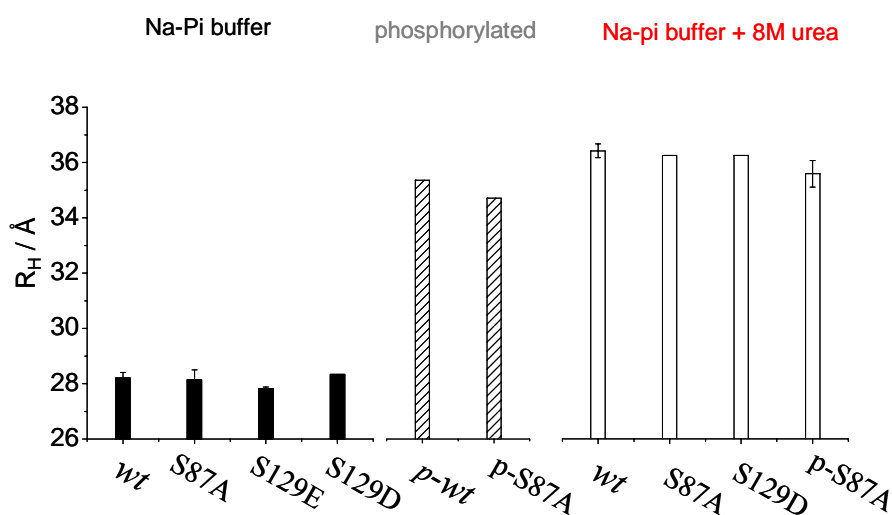


Figure 5.4: Phosphorylation expands the ensemble of conformation in monomeric α S. Hydrodynamic radii of various α S mutants in phosphate buffer at +15 °C with and without 8M urea.

Upon addition of 8M urea, it increased to 36.4 Å. For S87A αS, the corresponding values were 28.1 Å and 36.2 Å, respectively. If αS were a random coil, a hydrodynamic radius of 36.9 Å would be expected^[88]. When wt αS was phosphorylated, the hydrodynamic radius increased by 7.1 Å to 35.3 Å. Similarly, phosphorylation of S87A αS at S129 increased R_H by 6.6 Å to 34.7 Å (Fig.5.4). Addition of 8 M urea to phosphorylated S87A αS only slightly further increased the R_H value to 35.6 Å, indicating that phosphorylation extends the ensemble of conformations populated by αS close to its fully random coil-like dimensions.

5.3.1.3. S129E/D do not reproduce the structural consequences of phosphorylation

To evaluate if mutation into a charged residue can mimic the effect of phosphorylation on the conformation of αS, we characterized monomeric S129D and S129E αS by NMR spectroscopy. The ^1H - ^{15}N HSQC spectra of S129D/E αS was highly similar to that observed for the wt protein. Chemical shift changes were restricted to the direct vicinity of the mutation site and $^3\text{J}_{\text{H}^{\text{N}}\text{H}^{\alpha}}$ were largely unchanged (Fig.5.5.a, b). Pulsed field gradient NMR experiments determined a hydrodynamic radius of 28.3 Å and 27.8 Å for S129D and S129E αS (Fig.5.4), respectively, values very similar to wt αS ($R_H = 28.2$ Å) but significantly smaller than that observed for phosphorylated αS ($R_H = 35.3$ Å).

Thus, mutation of S129 into aspartate or glutamate does not disrupt the long-range interactions that stabilize wt αS. This suggests that mutation of Ser or Thr residues to Asp or Glu cannot fully mimic the effect of phosphorylation on the structure and dynamics of αS and potentially other intrinsically disordered proteins.

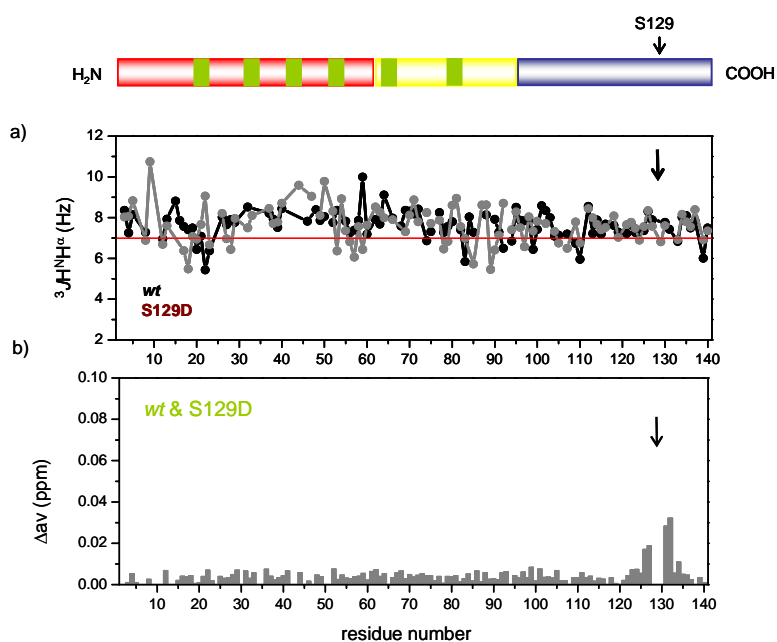


Figure 5.5: a) Comparison of $^3J_{H^N H^\alpha}$ scalar couplings observed in S129D α S (grey) and in wt α S (black). b) Normalized weighted average 1H - ^{15}N chemical shift differences between wt and S129D α S.

5.3.1.4. Phosphorylation disrupts transient intramolecular long-range interactions.

To probe the effect of phosphorylation on transient long-range interactions, Paramagnetic resonance enhancement of NMR was measured. The interactions between a specifically attached paramagnetic nitroxide radical and nearby (less than 25 Å) protons cause broadening of their NMR signals because of an increase in transverse relaxation rate ^[137]. This effect has an r^{-6} dependence on the electron-proton distance and thus allows the measurement of long-range distances between the spin label and the affected amide protons in proteins ^[138]. Because the primary sequence of α S lacks Cys, A18 was mutated into a Cys to provide an attachment point for the nitroxide radical MTSL. Neither the mere introduction of the mutation nor the addition of the MTSL radical modified the hydrodynamic radius or altered the time course of aggregation for α S ^[53].

Figure 5.6 compares the PRE profile observed for unphosphorylated wt and phosphorylated S87A α S. In unphosphorylated wt α S, the profile of intensity ratios showed a broad paramagnetic effect extending to residue 60 and long-range interactions with C-terminal residues 115-140, in agreement with previous measurements^[53]. In phosphorylated S87A α S, the paramagnetic broadening was largely restricted to the vicinity of the spin label; signal intensity ratios for residues 45 to 60 and for C-terminal residues 120 to 135 approached values close to one. PRE of amide protons showed that long-range interactions between the N- and the C-terminal domain of α S were attenuated upon phosphorylation at S129.

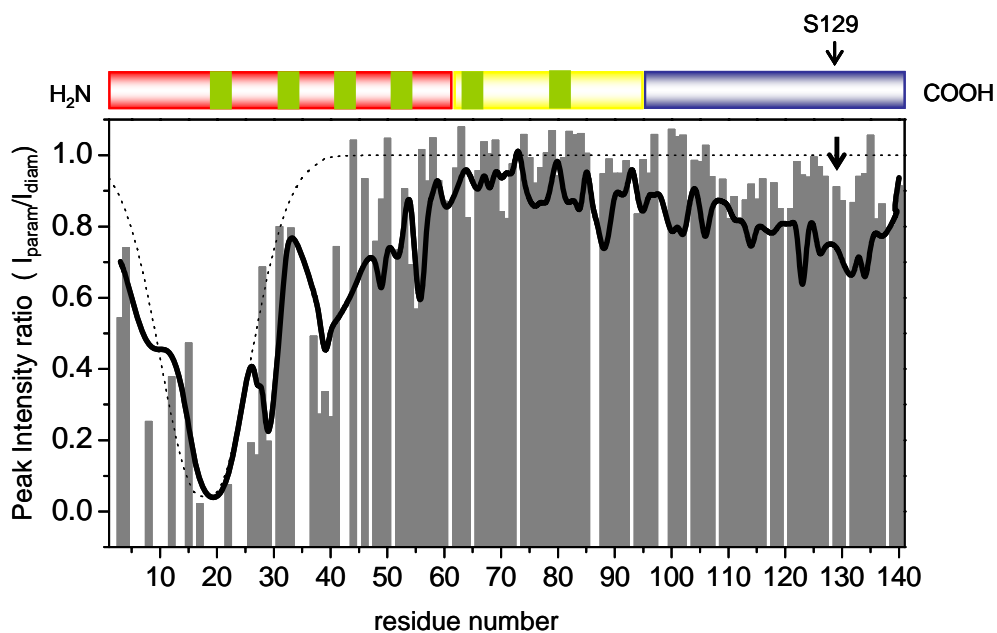


Figure 5.6: Comparison of paramagnetic broadening of amide protons between unphosphorylated wt α S (black) and phosphorylated S87A α S (grey). In both cases the paramagnetic MTSL spin label was attached to residue 18, which was mutated from Ala to Cys. HSQC spectra in the presence (paramagnetic) and absence (diamagnetic) of spin label were recorded at 15°C, and the intensity ratio of the resonance peaks was determined. Dashed lines indicate paramagnetic effects expected for a random coil polypeptide.

5.3.1.5. S129E exhibits similar *in vitro* aggregation properties as wt α -synuclein

To determine the effect of the phospho-mimicking mutations on the aggregation properties of α S, we compared the aggregation propensity of S129E and S129A to that of the wt protein as a function of time using the ThT binding assay and TEM (Fig.5.7). In a few experiments, the S129E variant formed slightly more fibrils than wt protein, but these differences are not statistically significant, and in other experiments there were no differences in amyloid formation between the two proteins (wt and S129E).

In contrast, we consistently observed that the S129A fibrillizes more rapidly and forms significantly more fibrils than both the wt and the phosphorylation mimic, S129E. Both S129A and S129E α S formed classical amyloid like fibrils with morphological features similar to that of wt α S.

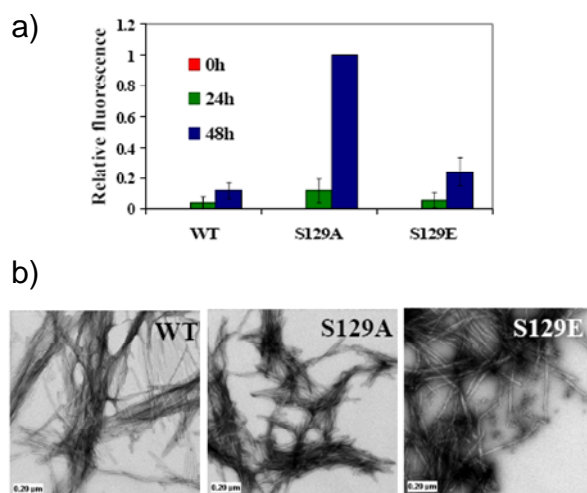


Figure 5.7: a) ThT fluorescence was monitored at indicated time-points from samples of 100 μ M solutions of wt, S129A and S129E α S incubated at 37 $^{\circ}$ C. The error bars represent the standard deviation of 4 independent experiments. b) TEM images of the same samples after 4 days (scale bar 200 nm).

5.3.1.6. Phosphorylation at S129 is sufficient to inhibit the aggregation of wt α -synuclein

To determine the relative contribution of phosphorylation at S129 to the CK1-induced inhibition of α S fibril formation, the effect of CK1-mediated phosphorylation on the fibrillization of S87A mutant of α S was examined. Prephosphorylation of S87A with CK1 resulted in significant inhibition of α S fibrillization relative to the unphosphorylated forms of the protein.

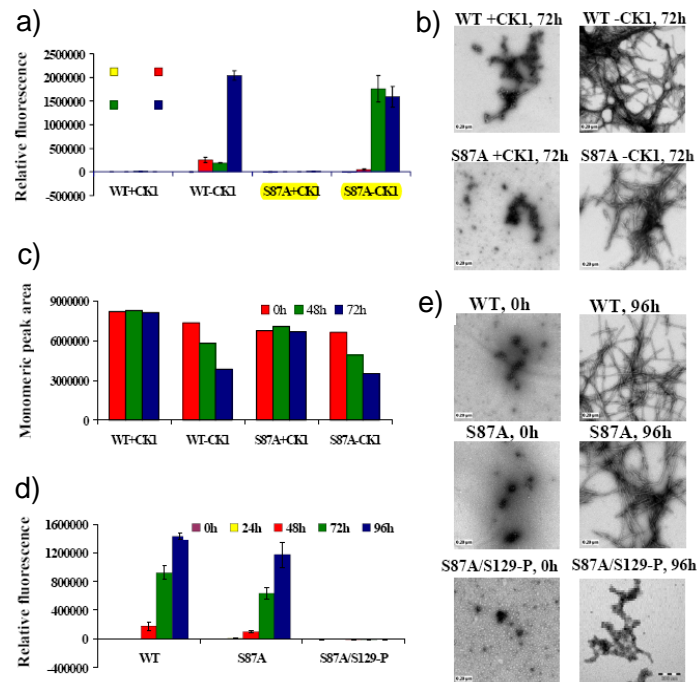


Figure 5.8: CK1-mediated phosphorylation at S129 inhibits the fibrillization of wt and S87A α S. a) ThT fluorescence measurements of CK1 phosphorylated wt and S87A α S and their unphosphorylated controls (100 μ M), average of 3 readings \pm s.d. b) TEM images of phosphorylated and unphosphorylated S87A α S after 72 h of aggregation at 37 $^{\circ}$ C (scale bar 200 nm) c) Graph representing the area of monomeric peak after 0, 48 and 72 h of aggregation at 37 $^{\circ}$ C. d) ThT fluorescence measurement of wt, S87A and S87A/S129-P α S as a function of time (average of 3 readings \pm s.d.). e) TEM images of wt, S87A and S87A/S129-P α S at 0 h and after 96 h of aggregation at 37 $^{\circ}$ C (scale bar 200 nm).

After 72 h of incubation under agitation conditions, S87A formed significant amount of amyloid fibrils, whereas the prephosphorylated form of S87A showed predominantly soluble α S species (Fig.5.8.a, b). Consistent with the TEM and ThT results, the amount of monomeric prephosphorylated S87A remained unchanged during the course of the aggregation experiment (72 h), whereas the amount of monomeric unphosphorylated S87A decreased significantly with time.

To further demonstrate that inhibition of α S fibrillogenesis is due to phosphorylation at S129, we purified the phosphorylated form of S87A and compared its aggregation properties to that of S87A and wt α S. When purified wt, S87A and S87A/S129-P α S were subjected to aggregation conditions at 37 °C with continuous agitation, S87A/S129-P did not form any fibrils and remained in a predominantly monomeric state even after 96 h of incubation, whereas the unphosphorylated S87A and wt α S exhibited high levels of fibrillization as demonstrated by the increased ThT fluorescence (Fig.5.8.d) and detection of fibrillar structures by TEM (Fig.5.8.e).

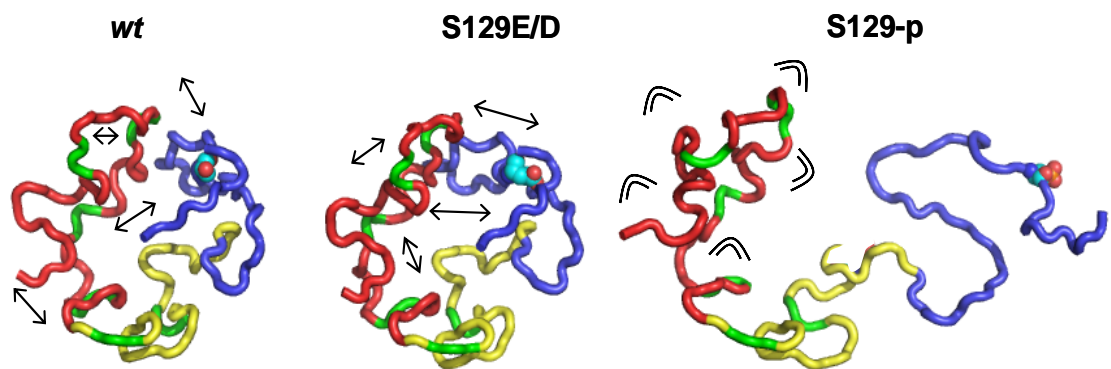


Figure 5.9: Schematic illustration of the disruption of long-range interactions in α S upon phosphorylation at S129. Red indicates the positively charged N-terminus, yellow indicates the aggregation prone-mainly hydrophobic NAC region and blue indicates the negatively charged C-terminus domain. **wt:** Representative member of the native state ensemble of conformations populated by α S^[53]. The side chain of S129 is shown. Long-range interactions are indicated by arrows. **S129E/D:** Phosphomimetic do not mimic the structural consequences of phosphorylation; the side chain at position 129 was replaced by a Glu, Asp. **S129-P:** upon phosphorylation at S129 long-range interactions are disrupted and the ensemble of conformations is extended. The higher flexibility of the N-terminal domain is indicated.

On the basis of the our NMR data, we concluded that the phosphorylation of α S at S129 increases the conformational flexibility (Fig.5.9) and converts α S into more unfolded forms that self-associate readily, resulting in aggregation *in vitro*^[53]. It is nicely matched with recent NMR study using casein kinase 2 (CK2)-mediated phosphorylation α S at S129^[136]. As shown in TEM images (Fig.5.8), however, the S129-P of α S rather inhibits the fibrillization than promotes. The TEM images clearly shows rare fibrils even after 72 hours incubation, but exhibits small aggregates and protofibrils. Recently, Sugeno *et al.*^[139] reported that S129-P appears to facilitate aggregate formation in mammalian cells and S129-P is required not only for aggregate

formation but also for the induction of α S toxicity. Taken together, the S129-P does not produce the fibril but the small aggregates which may be important for the toxic effect of α S, called protofibrils.

5.3.2. α -synuclein phosphorylation at S87

The pathological role of S87 phosphorylation *in vivo* and its relevance with the structural and aggregation properties of α S *in vitro* is not clearly reported. Toward to this goal, an array of biochemical and biophysical methods, including ThT binding, TEM and NMR spectroscopy were applied to phosphomimic S87E, *in vitro* phosphorylated S87 (S87-P), S87A and wt α S. It is demonstrated that phosphorylation at S87 slightly expands the structure of α S, increases its conformational flexibility and blocks its fibrillization *in vitro*.

5.3.2.1. Phosphorylation at S87 is sufficient to block α -synuclein fibrillization and phosphomimic S87E aggregates slower than wt and S87A

To determine the relative contribution of phosphorylation at S87 to the CK1-induced inhibition of α S fibril formation, the effect of CK1-mediated phosphorylation on the fibrillization of the S129A and S129E, both of which cannot be phosphorylated at S129, were examined. The S87-P phosphorylated forms of S129A and S129E α S were prepared and their aggregation properties were compared to prove that inhibition of α S fibrillogenesis is due to phosphorylation at S87. These observations were confirmed by TEM studies, which revealed the absence of any fibrillar aggregates in the S129A/S87-P and S129E/S87-P (Fig.5.10). Interestingly, monophosphorylated S129E/S87-P appears to form significantly less oligomeric/protofibrillar-like aggregates than S129A/S87-P, suggesting that the presence of both phosphate and Glu substitutions at S87 and S129, respectively results in a greater inhibition of α S fibrillization (Fig.5.10).

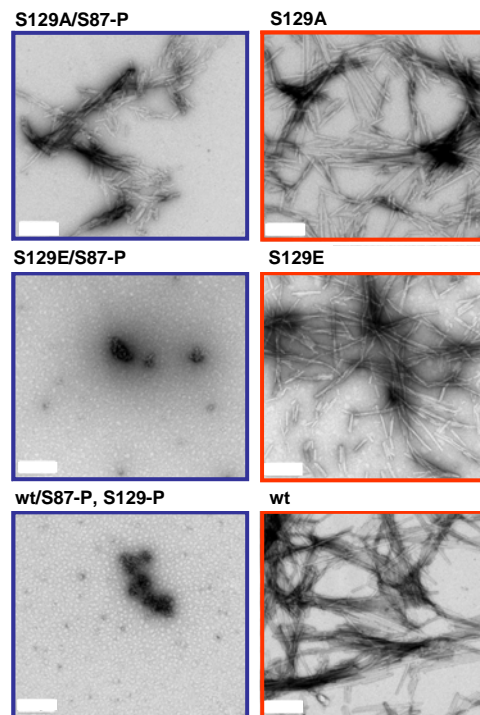


Figure 5.10: CK1-mediated phosphorylation inhibits the fibrillization of S129A, S129E and wt α S. TEM images of S129A, S129E and wt α S phosphorylated for 24 h with CK1 and then aggregated. Negatively stained TEM images of phosphorylated S129A and S129E and their unphosphorylated control after 12 h of incubation at 37 °C under agitating conditions (scales bar 200 nm).

Selective phosphorylation and/or overexpression of S87-P *in vivo* are currently not possible. Therefore, future efforts to assess the role of S87 phosphorylation in modulating the normal biology and aggregation of α S *in vivo* are likely to rely on the use of the phosphomimics S87E and S87A. Having established that S87-P is sufficient to inhibit α S oligomerization and fibrillogenesis, the 87 mutants (S87A and S87E) were generated to assess whether the phosphorylation mimic S87E is likely to mimic S87 phosphorylation *in vivo*. Comparison of the fibrillization of wt, S87A and S87E α S showed that S87A aggregated at a similar rate and to similar levels as wt α S, whereas for S87E the observed aggregation rate was slower than those of the wt and S87A

proteins. TEM images further confirmed these findings, as both wt and S87A formed dense networks of fibrils as opposed to S87E, which formed a few short fibrils after 72 h of aggregation (Fig.5.11).

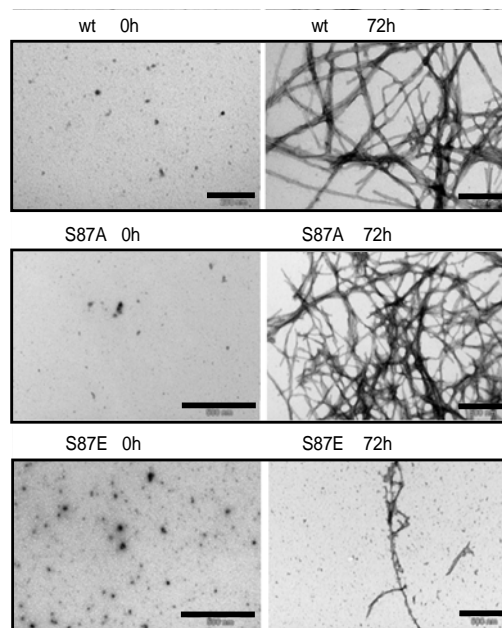


Figure 5.11: TEM images of wt, S87A and S87E α S after 0 h and 72 h of incubation at 37 °C under agitating conditions (Scales bar 500 nm).

5.3.2.2. α -synuclein S→A and S→E mutations can mimic S87, but not S129, phosphorylation

Studies on the potential role of S129 phosphorylation in modulating α S aggregation and toxicity in cell culture and animal models of synucleinopathies have relied primarily on the overexpression of S129D and S129A α S mutants to mimic and abolish phosphorylation *in vivo*, respectively, and have yielded contradictory results. Feany *et al.*^[121] reported that overexpression of the phosphomimic S129D or coexpression of the wt and Grpk2 does not affect inclusion formation, but results in

enhanced loss of dopaminergic neurons, whereas overexpression of S129A results in increased aggregation (4-5 times more than wt α S), yet protects against α S toxicity. However, recent studies by two independent research groups demonstrated that AAV mediated overexpression of the S129A in the substantia nigra of rats results in both increased aggregation and loss of dopaminergic neurons relative to overexpression of wt and S129D α S^[140].

Thus it appears that the increased *in vivo* aggregation caused by the S129A mutation (which also promotes α S aggregation *in vitro*) may lead to toxicity that is unrelated to its effect in blocking phosphorylation at S129. To properly probe the role of phosphorylation *in vivo*, it is essential that mutants designed to abolish phosphorylation should exhibit aggregation properties similar to that of the wt protein. Similarly, phosphorylation mimicking mutations should reproduce the structural and functional consequences of α S phosphorylation. Neither the S129A nor S129D/E mutants fulfill these criteria as demonstrated by both the *in vivo* studies cited above and our own recent *in vitro* studies.

In contrast, as shown above, the S87A and S87E mutants fulfill these criteria to a greater extent. Figure 5.11 demonstrates that S87A exhibits similar fibrillization properties as the wt protein, whereas S87E does not form amyloid fibrils, suggesting S \rightarrow E substitution at S87 reproduces the effect of phosphorylation on α S aggregation. Together these findings suggest that overexpression of S87E and S87A mutants should facilitate in the elucidation of the role of phosphorylating this residue on the normal physiology and pathogenesis of α S. In the case of blocking phosphorylation at S129, this could in principle be achieved by identifying S129x mutant that, like S129A, cannot

be phosphorylated at this residue, but that unlike S129A, exhibits similar aggregation properties as wt α S.

5.3.2.3. α -synuclein is disordered independent of phosphorylation at S87

2D ^1H - ^{15}N HSQC spectra were sharp and showed only a limited dispersion of chemical shifts, reflecting a high degree of backbone mobility. For S129D α S, phosphorylation at S129 was blocked such that only the resonance of S87 was attenuated at its original position and appeared at its phosphorylated position (Fig.5.12). Other chemical shift changes induced by phosphorylation were generally small.

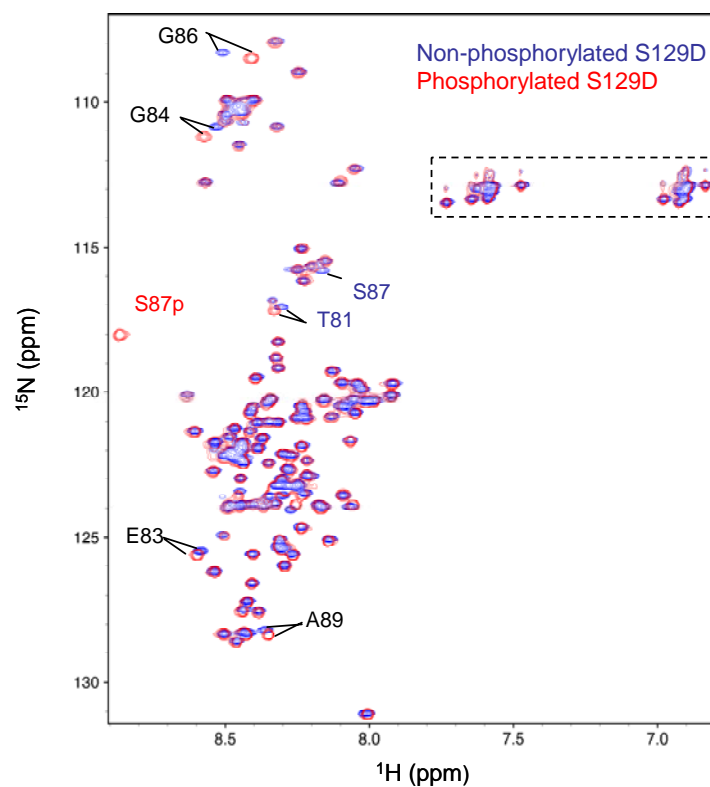


Figure 5.12: Comparison of 2D ^1H - ^{15}N HSQC spectra of non-phosphorylated S129D α S (blue) and phosphorylated S129D α S (red). Resonance assignments are indicated with residue numbers. A dashed rectangle marks Glutamine and Asparagine side chain resonances.

In addition, steady-state heteronuclear $^{15}\text{N}\{^1\text{H}\}$ -NOEs, ^{15}N $R_{1\rho}$ relaxation rates and $^3\text{J}_{\text{H}^{\text{N}}\text{H}^{\alpha}}$ couplings were very similar for unphosphorylated and phosphorylated αS (Fig.5.13), indicating that phosphorylation at S87 has no apparent effect on the secondary structure of αS . Thus, mutation of S129 into aspartate or glutamate does not disrupt the long-range interactions that stabilize wt αS .

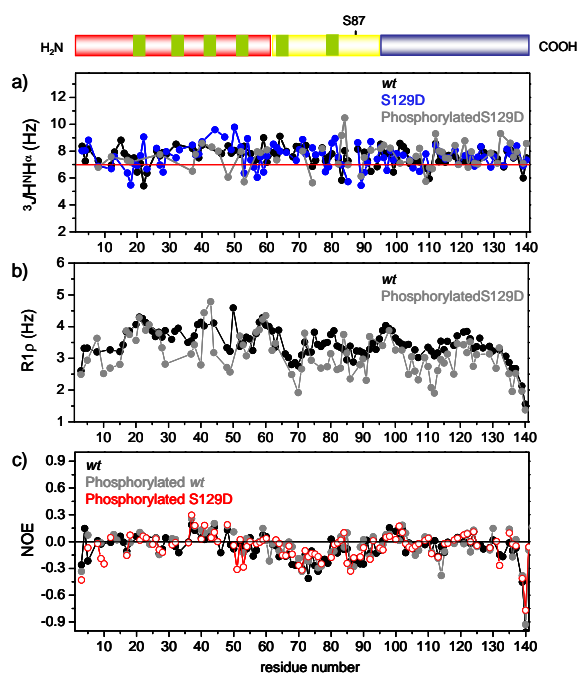


Figure 5.13: a) Comparison of $^3\text{J}_{\text{H}^{\text{N}}\text{H}^{\alpha}}$ scalar couplings observed in wt (black), S129D (blue) and phosphorylated S129D (grey) αS at +15 °C. b) Comparison of ^{15}N $R_{1\rho}$ spin relaxation rates in wt (black) and phosphorylated S129D (grey). c) Heteronuclear $^{15}\text{N}\{^1\text{H}\}$ -NOEs in wt αS (black), phosphorylated wt αS (grey) and phosphorylated S129D αS (red).

For wt and S129D αS , we determined hydrodynamic radii of 28.2 Å and 28.1 Å, respectively (Fig.5.14). The phosphorylation mimic S87E did not change the hydrodynamic radius of αS . On the other hand, phosphorylation of S129A and S129D αS at S87 increased R_{H} by 2.6 and 1.9 Å (Fig.5.14). Addition of 8 M urea to

phosphorylated S87A α S further increased the R_H value to 36.2 Å. If α S were a true random coil, a hydrodynamic radius of 36.9 Å would be expected [88].

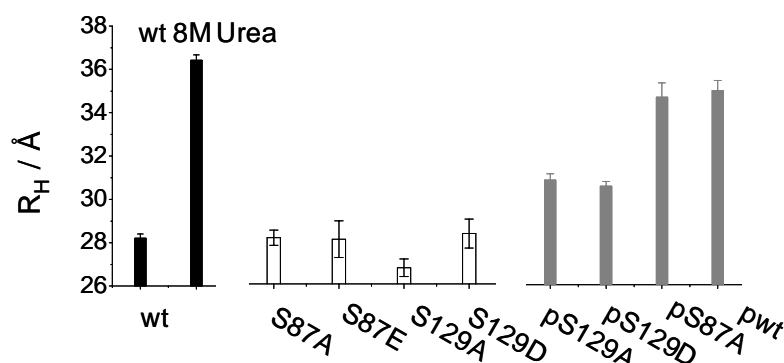


Figure 5.14: Hydrodynamic radius of various α S mutants in phosphate buffer at 15 °C with and without 8 M urea. In phosphorylated S129A/D α S, only S87 was phosphorylated.

5.3.2.4. Kinetics of wt and mutants α -synuclein phosphorylation

NMR spectroscopy on ^{15}N -labeled protein allows identification of all phosphorylation sites in the protein, measures their level of phosphate integration, and yields kinetic data for the enzymatic modification of the individual at selected sites [141]. To probe the kinetics of phosphorylation by CK1, a series of 2D ^1H - ^{15}N HSQC spectra of ^{15}N -labeled α S in the presence of the phosphorylation mixture were measured. Filtering through the ^{15}N label discards the necessity of sample purification and allows the *in situ* monitoring of kinase activity at selected sites [141]. CK1 phosphorylation of wt α S followed by tryptic digestion and mapping of phosphorylation sites revealed that CK1 phosphorylates α S at multiple sites (S87, T92 and S129), with S87 and S129 being the major phosphorylation site. T92 is not phosphorylated by CK1 in S87A α S, indicating that it is a follow up of phosphorylation at S87.

Figure 5.15 shows 1D ^1H slices through the center of the S87-P cross peak observed in ^1H - ^{15}N HSQC spectra of wt αS . The intensity of the S87-P cross peak increased rapidly and started to saturate at a phosphate integration level of about 85-90 % after 2000 to 3000 minutes. A similar behavior was observed for the S87-P cross peak of S129A and S129D αS (Fig.5.15.c). Detailed comparison of the time dependence of phosphorylation at S87 in wt, S129A and S129D αS shows that the kinetics of *in vitro* phosphorylation by CK1 at S87 is identical for all the three mutants. A similar approach was applied to study the kinetics of *in vitro* phosphorylation at S129. The intensity of the S129-P crosspeak continuously increased in both wt and S87A αS with increasing exposure time to the phosphorylation mixture (Fig.5.15.b, d). However, the rate of phosphorylation and the level of phosphate integration were different for wt, S87E and S87A αS . In wt αS , 75 % of the protein molecules had a phosphate group attached to S129 after 2000 minutes. In contrast, phosphorylation by CK1 was significantly slowed down in S87A αS such that only 40 % of protein molecules were phosphorylated at S129 after 2000 minutes. Interestingly, when S87 was mutated into S87E the rate of phosphorylation was intermediate to that of wt and S87A αS .

In vitro phosphorylation by CK1 was highly efficient resulting in phosphate integration of more than 90 % at position S87. Both the levels of phosphate integration at S87 and its kinetics were not influenced by the state of S129 phosphorylation (Fig.5.15.c). In contrast, *in vitro* phosphorylation at S129 is influenced by the phosphorylation state of S87. When phosphorylation at S87 was blocked by mutation of this residue into alanine, attachment of a phosphate group to the side chain of S129 was slowed down dramatically (Fig.5.15.d).

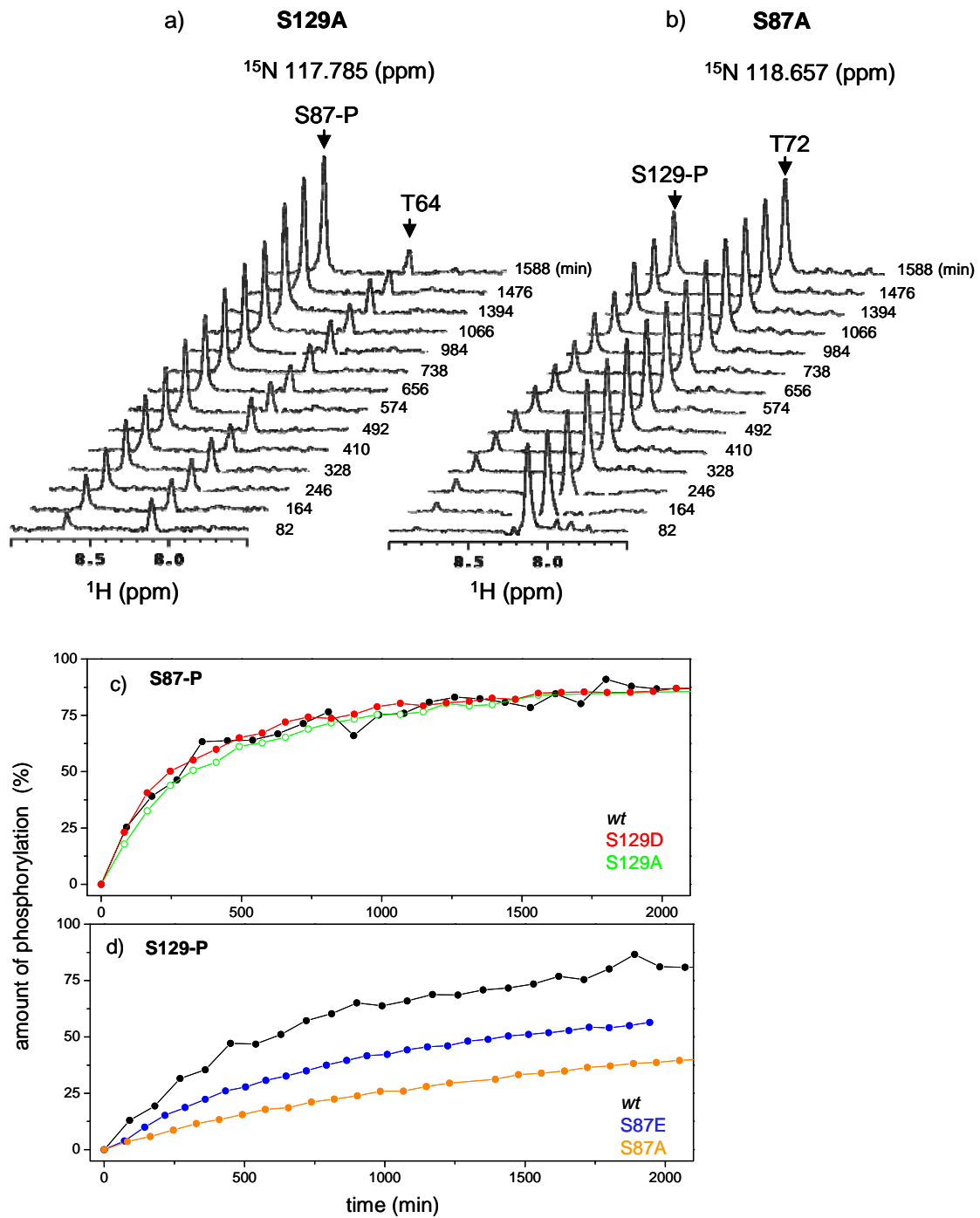


Figure 5.15: Phosphorylation at S87 by CK1 enhances phosphorylation at S129. a) 1D ^1H -slices through the center of the S87-P cross peak of ^1H - ^{15}N HSQC spectra of S129A and b) through the center of the S129-P crosspeak of S87A αS . c) Time dependence of phosphorylation at S87 by CK1 at +15 °C in buffer in wt (black), S129D (red) and S129A (green) αS . d) Time dependence of phosphorylation at S129 by CK1 at +15 °C in buffer in wt (black), S87E (blue) and S87A (orange) αS .

For S87E α S, the rate of phosphorylation is intermediate between wt and S87A α S. This suggests that the increased efficiency of *in vitro* phosphorylation at S129 in the presence of a phosphate group at position S87 is most likely due to an electrostatic effect: the two introduced negative charges result in an improved targeting of CK1 to S129. In addition, our hydrodynamic radius measurements showed that phosphorylation at S87 slightly expands the ensemble of conformations populated by α S in solution. Thus, the side chain of S129 might be more accessible to CK1, further enhancing the targeting of CK1 to S129. As signaling events as well as aggregation critically depend on the number of phosphorylation sites and the level of modification of any individual site ^[142], our data provide support for the importance of S87 for phosphorylation at S129 and its associated effects on aggregation and signaling.

5.3.2.5. Neither S87 nor S129 phosphorylation is required for LBs formation

The finding that majority of α S species within LBs are phosphorylated at S129 gave rise to the hypothesis that phosphorylation at this residue enhances α S fibrillization and promotes inclusions and LBs formation ^[119]. However, S129 lies in the highly negatively charged region of α S, which is disordered and remains accessible to kinases during the various stages of α S fibrillization including the mature fibrils (Fig.5.16.a). The co-localization of several kinases and α S within LBs, also the recent studies by Waxman and Giasson ^[134], which demonstrated that aggregated α S species are better substrate for CK1 and CK2 suggest that S129 phosphorylation could easily occur subsequent to LBs formation. These observations provide strong support for the hypothesis that phosphorylation at S129 is in fact not a prerequisite for LBs formation

but more likely occurs after α S fibrillization (Fig.5.16.b). In contrast, residue S87 lies in the hydrophobic NAC region of α S, which plays a critical role in the initiation and propagation of its aggregation and fibrillogenesis. Accordingly, negatively charged phosphorylate group at S87 blocks α S fibrillization. In addition, aggregated α S species cannot be phosphorylated at S87 because this residue is buried in the core of fibrils and is inaccessible to kinases (Fig.5.16.c), thus it explains the lack of S87-P immunoreactivity within LBs and fibrillar inclusions.

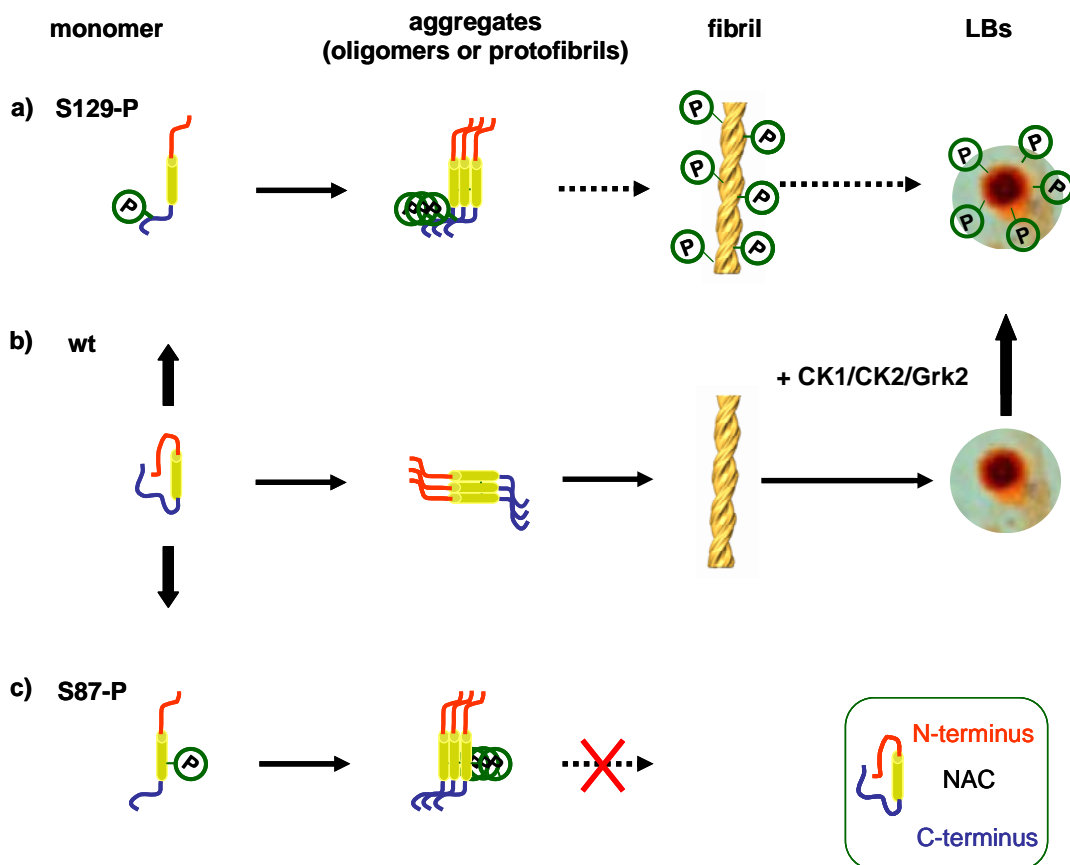


Figure 5.16: A schematic diagram of the aggregation and the phosphorylation of α S. a) S129-P^[136, 139], b) wt^[134] and c) S87-P of α S. The process which dashed arrows are not clearly confirmed yet.

5.4. Conclusion

In summary, above results have demonstrated that phosphorylation at S129 and S87 increases the conformational flexibility of α S and inhibits, rather than promotes, α S fibril formation *in vitro*. The C-terminal region of α S has been implicated in the majority of α S interactions with proteins^[84, 143, 144] and metal ions^[145, 146]. Therefore, phosphorylation at S129 is likely to influence α S affinity to proteins, metals and other ligands (e.g. dopamine) and alter the biochemical and biological processes regulated by these interactions. Equally important is our finding that the phosphorylation mimics (S129E/D) do not reproduce the effect of phosphorylation at this site in α S structure and aggregation properties *in vitro*. However, the phosphorylation mimic S87E is able to mimic the effect of phosphorylation on the aggregation properties of α S *in vitro*.

These findings highlight the critical importance of the increased negative charge and/or bulkiness of the phosphate group, relative to the carboxylate of Glu and Asp, in mediating the structural and functional consequences of phosphorylation. Several studies have reported that protein-protein interactions mediated by phospho-serines are abolished when serine is replaced by glutamate. In some of these studies it was shown that the bulkiness, steric hindrance^[147], or conformational changes^[148] induced by the phosphate group, rather than its negative charge, is responsible for the observed effects of phosphorylation. On this basis, one can speculate that phosphorylation of α S may constitute an important and specific regulator of α S aggregation and interactions with other proteins.

Taken all together, these observations have important implications for use of phosphomimics to elucidate the role of phosphorylation in modulating biological processes *in vivo* and underscore the importance of exercising caution when interpreting results obtained using phospho-mimicking mutants.

6. Bibliography

- [1] F. H. Crick, On protein synthesis, *Symp Soc Exp Biol* **1958**, *12*, 138.
- [2] F. Crick, Central dogma of molecular biology, *Nature* **1970**, *227*, 561.
- [3] C. M. Dobson, Protein folding and misfolding, *Nature* **2003**, *426*, 884.
- [4] C. B. Anfinsen, Principles that govern the folding of protein chains, *Science* **1973**, *181*, 223.
- [5] C. M. Dobson, M. Karplus, The fundamentals of protein folding: bringing together theory and experiment, *Curr Opin Struct Biol* **1999**, *9*, 92.
- [6] A. Fersht, *Structure and Mechanism in Protein Science: A Guide to Enzyme Catalysis and Protein Folding*, New York: W H Freeman & Co., **1999**.
- [7] M. Vendruscolo, E. Paci, M. Karplus, C. M. Dobson, Structures and relative free energies of partially folded states of proteins, *Proc Natl Acad Sci U S A* **2003**, *100*, 14817.
- [8] J. N. Onuchic, P. G. Wolynes, Theory of protein folding, *Curr Opin Struct Biol* **2004**, *14*, 70.
- [9] R. Winter, D. Ropes, S. Grudzielanek, K. Vogtt, Towards an Understanding of the Temperature/Pressure Configurational and Free-Energy Landscape of Biomolecules, *J Non-Equilib Thermodyn* **2007**, *32*, 41.
- [10] R. Mishra, R. Winter, Cold- and Pressure-Induced Dissociation of Protein Aggregates and Amyloid Fibrils, *Angew Chem Int Ed Engl* **2008**, *47*, 6518.
- [11] F. Chiti, C. M. Dobson, Protein misfolding, functional amyloid, and human disease, *Annu Rev Biochem* **2006**, *75*, 333.
- [12] L. C. Serpell, Alzheimer's amyloid fibrils: structure and assembly, *Biochim Biophys Acta* **2000**, *1502*, 16.

-
- [13] E. H. Koo, P. T. Lansbury, Jr., J. W. Kelly, Amyloid diseases: abnormal protein aggregation in neurodegeneration, *Proc Natl Acad Sci U S A* **1999**, *96*, 9989.
- [14] D. J. Selkoe, Folding proteins in fatal ways, *Nature* **2003**, *426*, 900.
- [15] A. Lomakin, D. B. Teplow, D. A. Kirschner, G. B. Benedek, Kinetic theory of fibrillogenesis of amyloid beta-protein, *Proc Natl Acad Sci U S A* **1997**, *94*, 7942.
- [16] R. Sabate, J. Estelrich, Evidence of the existence of micelles in the fibrillogenesis of beta-amyloid peptide, *J Phys Chem B* **2005**, *109*, 11027.
- [17] R. M. Murphy, Peptide aggregation in neurodegenerative disease, *Annu Rev Biomed Eng* **2002**, *4*, 155.
- [18] O. S. Makin, E. Atkins, P. Sikorski, J. Johansson, L. C. Serpell, Molecular basis for amyloid fibril formation and stability, *Proc Natl Acad Sci U S A* **2005**, *102*, 315.
- [19] H. A. Lashuel, B. M. Petre, J. Wall, M. Simon, R. J. Nowak, T. Walz, P. T. Lansbury, Jr., Alpha-synuclein, especially the Parkinson's disease-associated mutants, forms pore-like annular and tubular protofibrils, *J Mol Biol* **2002**, *322*, 1089.
- [20] H. A. Lashuel, Membrane permeabilization: a common mechanism in protein-misfolding diseases, *Sci Aging Knowledge Environ* **2005**, *2005*, pe28.
- [21] M. Goedert, Parkinson's disease and other alpha-synucleinopathies, *Clin Chem Lab Med* **2001**, *39*, 308.
- [22] J. E. Galvin, K. Uryu, V. M. Lee, J. Q. Trojanowski, Axon pathology in Parkinson's disease and Lewy body dementia hippocampus contains alpha-, beta-, and gamma-synuclein, *Proc Natl Acad Sci U S A* **1999**, *96*, 13450.
- [23] M. G. Spillantini, M. L. Schmidt, V. M. Lee, J. Q. Trojanowski, R. Jakes, M. Goedert, Alpha-synuclein in Lewy bodies, *Nature* **1997**, *388*, 839.
- [24] T. M. Dawson, V. L. Dawson, Molecular pathways of neurodegeneration in Parkinson's disease, *Science* **2003**, *302*, 819.

- [25] M. H. Polymeropoulos, C. Lavedan, E. Leroy, S. E. Ide, A. Dehejia, A. Dutra, B. Pike, H. Root, J. Rubenstein, R. Boyer, E. S. Stenroos, S. Chandrasekharappa, A. Athanassiadou, T. Papapetropoulos, W. G. Johnson, A. M. Lazzarini, R. C. Duvoisin, G. Di Iorio, L. I. Golbe, R. L. Nussbaum, Mutation in the alpha-synuclein gene identified in families with Parkinson's disease, *Science* **1997**, *276*, 2045.
- [26] R. Kruger, W. Kuhn, T. Muller, D. Woitalla, M. Graeber, S. Kosel, H. Przuntek, J. T. Epplen, L. Schols, O. Riess, Ala30Pro mutation in the gene encoding alpha-synuclein in Parkinson's disease, *Nat Genet* **1998**, *18*, 106.
- [27] A. B. Singleton, M. Farrer, J. Johnson, A. Singleton, S. Hague, J. Kachergus, M. Hulihan, T. Peuralinna, A. Dutra, R. Nussbaum, S. Lincoln, A. Crawley, M. Hanson, D. Maraganore, C. Adler, M. R. Cookson, M. Muentert, M. Baptista, D. Miller, J. Blancato, J. Hardy, K. Gwinn-Hardy, alpha-Synuclein locus triplication causes Parkinson's disease, *Science* **2003**, *302*, 841.
- [28] J. J. Zarranz, J. Alegre, J. C. Gomez-Esteban, E. Lezcano, R. Ros, I. Ampuero, L. Vidal, J. Hoenicka, O. Rodriguez, B. Atares, V. Llorens, E. Gomez Tortosa, T. del Ser, D. G. Munoz, J. G. de Yebenes, The new mutation, E46K, of alpha-synuclein causes Parkinson and Lewy body dementia, *Ann Neurol* **2004**, *55*, 164.
- [29] K. A. Conway, S. J. Lee, J. C. Rochet, T. T. Ding, R. E. Williamson, P. T. Lansbury, Jr., Acceleration of oligomerization, not fibrillization, is a shared property of both alpha-synuclein mutations linked to early-onset Parkinson's disease: implications for pathogenesis and therapy, *Proc Natl Acad Sci U S A* **2000**, *97*, 571.
- [30] S. J. Wood, J. Wypych, S. Steavenson, J. C. Louis, M. Citron, A. L. Biere, alpha-synuclein fibrillogenesis is nucleation-dependent. Implications for the pathogenesis of Parkinson's disease, *J Biol Chem* **1999**, *274*, 19509.
- [31] O. M. El-Agnaf, R. Jakes, M. D. Curran, D. Middleton, R. Ingenito, E. Bianchi, A. Pessi, D. Neill, A. Wallace, Aggregates from mutant and wild-type alpha-synuclein

- proteins and NAC peptide induce apoptotic cell death in human neuroblastoma cells by formation of beta-sheet and amyloid-like filaments, *FEBS Lett* **1998**, *440*, 71.
- [32] B. I. Giasson, I. V. Murray, J. Q. Trojanowski, V. M. Lee, A hydrophobic stretch of 12 amino acid residues in the middle of alpha-synuclein is essential for filament assembly, *J Biol Chem* **2001**, *276*, 2380.
- [33] J. C. Rochet, K. A. Conway, P. T. Lansbury, Jr., Inhibition of fibrillization and accumulation of prefibrillar oligomers in mixtures of human and mouse alpha-synuclein, *Biochemistry* **2000**, *39*, 10619.
- [34] M. M. Mouradian, Recent advances in the genetics and pathogenesis of Parkinson disease, *Neurology* **2002**, *58*, 179.
- [35] F. Meersman, C. M. Dobson, K. Heremans, Protein unfolding, amyloid fibril formation and configurational energy landscapes under high pressure conditions, *Chem Soc Rev* **2006**, *35*, 908.
- [36] P. L. Privalov, Cold denaturation of proteins, *Crit Rev Biochem Mol Biol* **1990**, *25*, 281.
- [37] G. S. Huang, T. G. Oas, Heat and cold denatured states of monomeric lambda repressor are thermodynamically and conformationally equivalent, *Biochemistry* **1996**, *35*, 6173.
- [38] P. L. Privalov, V. Griko Yu, S. Venyaminov, V. P. Kutysenko, Cold denaturation of myoglobin, *J Mol Biol* **1986**, *190*, 487.
- [39] J. J. Skalicky, D. K. Sukumaran, J. L. Mills, T. Szyperski, Toward Structural Biology in Supercooled Water, *J. Am. Chem. Soc.* **2000**, *122*, 3230.
- [40] H. Y. Kim, M. K. Cho, D. Riedel, C. O. Fernandez, M. Zweckstetter, Dissociation of amyloid fibrils of alpha-synuclein in supercooled water, *Angew Chem Int Ed Engl* **2008**, *47*, 5046.
- [41] Y. Li, B. Shan, D. P. Raleigh, The cold denatured state is compact but expands at low temperatures: hydrodynamic properties of the cold denatured state of the C-terminal domain of L9, *J Mol Biol* **2007**, *368*, 256.

6. Bibliography

- [42] C. R. Babu, V. J. Hilser, A. J. Wand, Direct access to the cooperative substructure of proteins and the protein ensemble via cold denaturation, *Nat Struct Mol Biol* **2004**, *11*, 352.
- [43] F. Bloch, Nuclear Induction, *Physical Review* **1946**, *70*, 460.
- [44] E. M. Purcell, H. C. Torrey, R. V. Pound, Resonance Absorption by Nuclear Magnetic Moments in a Solid, *Physical Review* **1946**, *69*, 37.
- [45] M. Sattler, J. g. Schleucher, C. Griesinger, Heteronuclear multidimensional NMR experiments for the structure determination of proteins in solution employing pulsed field gradients, *Progress in Nuclear Magnetic Resonance Spectroscopy* **1999**, *34*, 93.
- [46] M. Karplus, Vicinal proton coupling in nuclear magnetic resonance, *Journal of the American Chemical Society* **1963**, *85*, 2870.
- [47] H. Schwalbe, K. M. Fiebig, M. Buck, J. A. Jones, S. B. Grimshaw, A. Spencer, S. J. Glaser, L. J. Smith, C. M. Dobson, Structural and dynamical properties of a denatured protein. Heteronuclear 3D NMR experiments and theoretical simulations of lysozyme in 8 M urea, *Biochemistry* **1997**, *36*, 8977.
- [48] D. S. Wishart, B. D. Sykes, Chemical shifts as a tool for structure determination, *Methods Enzymol* **1994**, *239*, 363.
- [49] J. Jeener, B. H. Meier, P. Bachmann, R. R. Ernst, Investigation of exchange processes by two-dimensional NMR spectroscopy, *The Journal of Chemical Physics* **1979**, *71*, 4546.
- [50] K. Wütrich, *NMR of proteins and nucleic acids*, Wiley-Interscience, New York, **1986**.
- [51] J. L. Battiste, G. Wagner, Utilization of site-directed spin labeling and high-resolution heteronuclear nuclear magnetic resonance for global fold determination of large proteins with limited nuclear overhauser effect data, *Biochemistry* **2000**, *39*, 5355.
- [52] P. A. Kosen, Spin labeling of proteins, *Methods Enzymol* **1989**, *177*, 86.

- [53] C. W. Bertoncini, Y. S. Jung, C. O. Fernandez, W. Hoyer, C. Griesinger, T. M. Jovin, M. Zweckstetter, Release of long-range tertiary interactions potentiates aggregation of natively unstructured alpha-synuclein, *Proc Natl Acad Sci U S A* **2005**, *102*, 1430.
- [54] E. O. Stejskal, J. E. Tanner, Spin Diffusion Measurements - Spin Echoes In Presence Of A Time-Dependent Field Gradient, *J Chem Phys* **1965**, *42*, 288.
- [55] P. Bernado, J. Garcia de la Torre, M. Pons, Macromolecular crowding in biological systems: hydrodynamics and NMR methods, *J Mol Recognit* **2004**, *17*, 397.
- [56] J. A. Jones, D. K. Wilkins, L. J. Smith, C. M. Dobson, Characterisation of protein unfolding by NMR diffusion measurements, *J Biomol NMR* **1997**, *10*, 199.
- [57] D. K. Wilkins, S. B. Grimshaw, V. Receveur, C. M. Dobson, J. A. Jones, L. J. Smith, Hydrodynamic radii of native and denatured proteins measured by pulse field gradient NMR techniques, *Biochemistry* **1999**, *38*, 16424.
- [58] M. Masuda, N. Dohmae, T. Nonaka, T. Oikawa, S. Hisanaga, M. Goedert, M. Hasegawa, Cysteine misincorporation in bacterially expressed human alpha-synuclein, *FEBS Lett* **2006**, *580*, 1775.
- [59] S. Der Sarkissian, E. L. Marchand, D. Duguay, P. Hamet, D. deBlois, Reversal of interstitial fibroblast hyperplasia via apoptosis in hypertensive rat heart with valsartan or enalapril, *Cardiovasc Res* **2003**, *57*, 775.
- [60] D. M. Walsh, D. M. Hartley, Y. Kusumoto, Y. Fezoui, M. M. Condron, A. Lomakin, G. B. Benedek, D. J. Selkoe, D. B. Teplow, Amyloid beta-protein fibrillogenesis. Structure and biological activity of protofibrillar intermediates, *J Biol Chem* **1999**, *274*, 25945.
- [61] H. LeVine, 3rd, Thioflavine T interaction with synthetic Alzheimer's disease beta-amyloid peptides: detection of amyloid aggregation in solution, *Protein Sci* **1993**, *2*, 404.
- [62] R. Kaye, E. Head, J. L. Thompson, T. M. McIntire, S. C. Milton, C. W. Cotman, C. G. Glabe, Common structure of soluble amyloid oligomers implies common mechanism of pathogenesis, *Science* **2003**, *300*, 486.

- [63] R. Benz, K. Janko, W. Boos, P. Lauger, Formation of large, ion-permeable membrane channels by the matrix protein (porin) of *Escherichia coli*, *Biochim Biophys Acta* **1978**, 511, 305.
- [64] R. Benz, K. Janko, P. Lauger, Ionic selectivity of pores formed by the matrix protein (porin) of *Escherichia coli*, *Biochim Biophys Acta* **1979**, 551, 238.
- [65] R. Benz, E. Maier, D. Ladant, A. Ullmann, P. Sebo, Adenylate cyclase toxin (CyaA) of *Bordetella pertussis*. Evidence for the formation of small ion-permeable channels and comparison with HlyA of *Escherichia coli*, *J Biol Chem* **1994**, 269, 27231.
- [66] F. Delaglio, S. Grzesiek, G. W. Vuister, G. Zhu, J. Pfeifer, A. Bax, NMRPipe: a multidimensional spectral processing system based on UNIX pipes, *J Biomol NMR* **1995**, 6, 277.
- [67] B. A. Johnson, R. A. Blevins, NMRView: A computer program for the visualization and analysis of NMR data, *J. Biomolecular NMR* **1994**, 4, 603.
- [68] G. Bodenhausen, D. J. Ruben, Natural abundance ^{15}N NMR by enhanced heteronuclear spectroscopy, *Chem. Phys. Lett.* **1980**, 69, 185.
- [69] P. K. Mandal, A. Majumdar, A comprehensive discussion of HSQC and HMQC pulse sequences, *Conc Mag Res* **2004**, A, 1.
- [70] J. W. Peng, G. Wagner, Investigation of protein motions via relaxation measurements, *Methods Enzymol* **1994**, 239, 563.
- [71] N. A. Farrow, R. Muhandiram, A. U. Singer, S. M. Pascal, C. M. Kay, G. Gish, S. E. Shoelson, T. Pawson, J. D. Forman-Kay, L. E. Kay, Backbone dynamics of a free and phosphopeptide-complexed Src homology 2 domain studied by ^{15}N NMR relaxation, *Biochemistry* **1994**, 33, 5984.
- [72] J. Cavanagh, *Protein NMR spectroscopy : principles and practice*, 2nd ed., Academic Press, Amsterdam ; Boston, **2007**.

-
- [73] D. S. Wishart, C. G. Bigam, J. Yao, F. Abildgaard, H. J. Dyson, E. Oldfield, J. L. Markley, B. D. Sykes, ^1H , ^{13}C and ^{15}N chemical shift referencing in biomolecular NMR, *J Biomol NMR* **1995**, *6*, 135.
- [74] D. J. Craik, J. A. Wilce, Studies of protein-ligand interactions by NMR, *Methods Mol Biol* **1997**, *60*, 195.
- [75] J. Hardy, D. J. Selkoe, The amyloid hypothesis of Alzheimer's disease: progress and problems on the road to therapeutics, *Science* **2002**, *297*, 353.
- [76] J. C. Rochet, P. T. Lansbury, Jr., Amyloid fibrillogenesis: themes and variations, *Curr Opin Struct Biol* **2000**, *10*, 60.
- [77] M. Sunde, L. C. Serpell, M. Bartlam, P. E. Fraser, M. B. Pepys, C. C. Blake, Common core structure of amyloid fibrils by synchrotron X-ray diffraction, *J Mol Biol* **1997**, *273*, 729.
- [78] J. W. Kelly, The alternative conformations of amyloidogenic proteins and their multi-step assembly pathways, *Curr Opin Struct Biol* **1998**, *8*, 101.
- [79] V. N. Uversky, A. L. Fink, Conformational constraints for amyloid fibrillation: the importance of being unfolded, *Biochim Biophys Acta* **2004**, *1698*, 131.
- [80] M. Fandrich, V. Forge, K. Buder, M. Kittler, C. M. Dobson, S. Diekmann, Myoglobin forms amyloid fibrils by association of unfolded polypeptide segments, *Proc Natl Acad Sci U S A* **2003**, *100*, 15463.
- [81] R. Tycko, Molecular structure of amyloid fibrils: insights from solid-state NMR, *Q Rev Biophys* **2006**, *39*, 1.
- [82] F. Chiti, M. Stefani, N. Taddei, G. Ramponi, C. M. Dobson, Rationalization of the effects of mutations on peptide and protein aggregation rates, *Nature* **2003**, *424*, 805.
- [83] A. M. Fernandez-Escamilla, F. Rousseau, J. Schymkowitz, L. Serrano, Prediction of sequence-dependent and mutational effects on the aggregation of peptides and proteins, *Nat Biotechnol* **2004**, *22*, 1302.

- [84] C. O. Fernandez, W. Hoyer, M. Zweckstetter, E. A. Jares-Erijman, V. Subramaniam, C. Griesinger, T. M. Jovin, NMR of alpha-synuclein-polyamine complexes elucidates the mechanism and kinetics of induced aggregation, *Embo J* **2004**, *23*, 2039.
- [85] M. Zweckstetter, A. Bax, Single-step determination of protein substructures using dipolar couplings: aid to structural genomics, *J Am Chem Soc* **2001**, *123*, 9490.
- [86] R. Bussell, Jr., D. Eliezer, Residual structure and dynamics in Parkinson's disease-associated mutants of alpha-synuclein, *J Biol Chem* **2001**, *276*, 45996.
- [87] S. Schwarzingler, G. J. Kroon, T. R. Foss, J. Chung, P. E. Wright, H. J. Dyson, Sequence-dependent correction of random coil NMR chemical shifts, *J Am Chem Soc* **2001**, *123*, 2970.
- [88] J. E. Kohn, I. S. Millett, J. Jacob, B. Zagrovic, T. M. Dillon, N. Cingel, R. S. Dothager, S. Seifert, P. Thiyagarajan, T. R. Sosnick, M. Z. Hasan, V. S. Pande, I. Ruczinski, S. Doniach, K. W. Plaxco, Random-coil behavior and the dimensions of chemically unfolded proteins, *Proc Natl Acad Sci U S A* **2004**, *101*, 12491.
- [89] M. D. Mukrasch, J. Biernat, M. von Bergen, C. Griesinger, E. Mandelkow, M. Zweckstetter, Sites of tau important for aggregation populate {beta}-structure and bind to microtubules and polyanions, *J Biol Chem* **2005**, *280*, 24978.
- [90] J. Wirmer, C. Schlorb, J. Klein-Seetharaman, R. Hirano, T. Ueda, T. Imoto, H. Schwalbe, Modulation of compactness and long-range interactions of unfolded lysozyme by single point mutations, *Angew Chem Int Ed Engl* **2004**, *43*, 5780.
- [91] L. Hou, H. Shao, Y. Zhang, H. Li, N. K. Menon, E. B. Neuhaus, J. M. Brewer, I. J. Byeon, D. G. Ray, M. P. Vitek, T. Iwashita, R. A. Makula, A. B. Przybyla, M. G. Zagorski, Solution NMR studies of the A beta(1-40) and A beta(1-42) peptides establish that the Met35 oxidation state affects the mechanism of amyloid formation, *J Am Chem Soc* **2004**, *126*, 1992.

- [92] J. Danielsson, A. Andersson, J. Jarvet, A. Graslund, 15N relaxation study of the amyloid beta-peptide: structural propensities and persistence length, *Magn Reson Chem* **2006**, *44 Spec No*, S114.
- [93] H. Heise, W. Hoyer, S. Becker, O. C. Andronesi, D. Riedel, M. Baldus, Molecular-level secondary structure, polymorphism, and dynamics of full-length alpha-synuclein fibrils studied by solid-state NMR, *Proc Natl Acad Sci U S A* **2005**, *102*, 15871.
- [94] P. Permi, I. Kilpelainen, A. Annala, S. Heikkinen, Intensity modulated HSQC and HMQC: two simple methods to measure 3J(HNH)alpha in proteins, *J Biomol NMR* **2000**, *16*, 29.
- [95] G. Cornilescu, F. Delaglio, A. Bax, Protein backbone angle restraints from searching a database for chemical shift and sequence homology, *J Biomol NMR* **1999**, *13*, 289.
- [96] A. Lange, S. Luca, M. Baldus, Structural constraints from proton-mediated rare-spin correlation spectroscopy in rotating solids, *J Am Chem Soc* **2002**, *124*, 9704.
- [97] A. Lange, K. Seidel, L. Verdier, S. Luca, M. Baldus, Analysis of proton-proton transfer dynamics in rotating solids and their use for 3D structure determination, *J Am Chem Soc* **2003**, *125*, 12640.
- [98] M. Vilar, H. T. Chou, T. Luhrs, S. K. Maji, D. Riek-Loher, R. Verel, G. Manning, H. Stahlberg, R. Riek, The fold of alpha-synuclein fibrils, *Proc Natl Acad Sci U S A* **2008**, *105*, 8637.
- [99] M. Sunde, C. Blake, The structure of amyloid fibrils by electron microscopy and X-ray diffraction, *Adv Protein Chem* **1997**, *50*, 123.
- [100] T. P. Knowles, A. W. Fitzpatrick, S. Meehan, H. R. Mott, M. Vendruscolo, C. M. Dobson, M. E. Welland, Role of intermolecular forces in defining material properties of protein nanofibrils, *Science* **2007**, *318*, 1900.

- [101] F. Meersman, C. M. Dobson, Probing the pressure-temperature stability of amyloid fibrils provides new insights into their molecular properties, *Biochim Biophys Acta* **2006**, *1764*, 452.
- [102] D. Foguel, M. C. Suarez, A. D. Ferrao-Gonzales, T. C. Porto, L. Palmieri, C. M. Einsiedler, L. R. Andrade, H. A. Lashuel, P. T. Lansbury, J. W. Kelly, J. L. Silva, Dissociation of amyloid fibrils of alpha-synuclein and transthyretin by pressure reveals their reversible nature and the formation of water-excluded cavities, *Proc Natl Acad Sci U S A* **2003**, *100*, 9831.
- [103] J. F. Smith, T. P. Knowles, C. M. Dobson, C. E. Macphee, M. E. Welland, Characterization of the nanoscale properties of individual amyloid fibrils, *Proc Natl Acad Sci U S A* **2006**, *103*, 15806.
- [104] V. A. Iconomidou, G. Vriend, S. J. Hamodrakas, Amyloids protect the silkworm oocyte and embryo, *FEBS Lett* **2000**, *479*, 141.
- [105] I. W. Hamley, Peptide fibrillization, *Angew Chem Int Ed Engl* **2007**, *46*, 8128.
- [106] L. Poppe, H. van Halbeek, NMR spectroscopy of hydroxyl protons in supercooled carbohydrates, *Nat Struct Biol* **1994**, *1*, 215.
- [107] R. Nelson, M. R. Sawaya, M. Balbirnie, A. O. Madsen, C. Riekel, R. Grothe, D. Eisenberg, Structure of the cross-beta spine of amyloid-like fibrils, *Nature* **2005**, *435*, 773.
- [108] P. Picotti, G. De Franceschi, E. Frare, B. Spolaore, M. Zambonin, F. Chiti, P. P. de Laureto, A. Fontana, Amyloid fibril formation and disaggregation of fragment 1-29 of apomyoglobin: insights into the effect of pH on protein fibrillogenesis, *J Mol Biol* **2007**, *367*, 1237.
- [109] F. Mallamace, M. Broccio, C. Corsaro, A. Faraone, D. Majolino, V. Venuti, L. Liu, C. Y. Mou, S. H. Chen, Evidence of the existence of the low-density liquid phase in supercooled, confined water, *Proc Natl Acad Sci U S A* **2007**, *104*, 424.

-
- [110] H. J. Dyson, P. E. Wright, Unfolded proteins and protein folding studied by NMR, *Chem Rev* **2004**, *104*, 3607.
- [111] H. Y. Kim, H. Heise, C. O. Fernandez, M. Baldus, M. Zweckstetter, Correlation of amyloid fibril beta-structure with the unfolded state of alpha-synuclein, *Chembiochem* **2007**, *8*, 1671.
- [112] S. Chimon, M. A. Shaibat, C. R. Jones, D. C. Calero, B. Aizezi, Y. Ishii, Evidence of fibril-like beta-sheet structures in a neurotoxic amyloid intermediate of Alzheimer's beta-amyloid, *Nat Struct Mol Biol* **2007**.
- [113] D. E. Ehrnhoefer, J. Bieschke, A. Boeddrich, M. Herbst, L. Masino, R. Lurz, S. Engemann, A. Pastore, E. E. Wanker, EGCG redirects amyloidogenic polypeptides into unstructured, off-pathway oligomers, *Nat Struct Mol Biol* **2008**, *15*, 558.
- [114] C. G. Glabe, Common mechanisms of amyloid oligomer pathogenesis in degenerative disease, *Neurobiol Aging* **2006**, *27*, 570.
- [115] M. J. Volles, P. T. Lansbury, Jr., Zeroing in on the pathogenic form of alpha-synuclein and its mechanism of neurotoxicity in Parkinson's disease, *Biochemistry* **2003**, *42*, 7871.
- [116] T. T. Ding, S. J. Lee, J. C. Rochet, P. T. Lansbury, Jr., Annular alpha-synuclein protofibrils are produced when spherical protofibrils are incubated in solution or bound to brain-derived membranes, *Biochemistry* **2002**, *41*, 10209.
- [117] S. D. Zakharov, J. D. Hulleman, E. A. Dutseva, Y. N. Antonenko, J. C. Rochet, W. A. Cramer, Helical alpha-synuclein forms highly conductive ion channels, *Biochemistry* **2007**, *46*, 14369.
- [118] P. Dustin, *Microtubules*, Springer, Berlin, **1984**.
- [119] H. Fujiwara, M. Hasegawa, N. Dohmae, A. Kawashima, E. Masliah, M. S. Goldberg, J. Shen, K. Takio, T. Iwatsubo, alpha-Synuclein is phosphorylated in synucleinopathy lesions, *Nat Cell Biol* **2002**, *4*, 160.

- [120] J. P. Anderson, D. E. Walker, J. M. Goldstein, R. de Laat, K. Banducci, R. J. Caccavello, R. Barbour, J. Huang, K. Kling, M. Lee, L. Diep, P. S. Keim, X. Shen, T. Chataway, M. G. Schlossmacher, P. Seubert, D. Schenk, S. Sinha, W. P. Gai, T. J. Chilcote, Phosphorylation of Ser-129 is the dominant pathological modification of alpha-synuclein in familial and sporadic Lewy body disease, *J Biol Chem* **2006**, *281*, 29739.
- [121] L. Chen, M. B. Feany, Alpha-synuclein phosphorylation controls neurotoxicity and inclusion formation in a Drosophila model of Parkinson disease, *Nat Neurosci* **2005**, *8*, 657.
- [122] P. J. Kahle, M. Neumann, L. Ozmen, V. Muller, H. Jacobsen, W. Spooren, B. Fuss, B. Mallon, W. B. Macklin, H. Fujiwara, M. Hasegawa, T. Iwatsubo, H. A. Kretschmar, C. Haass, Hyperphosphorylation and insolubility of alpha-synuclein in transgenic mouse oligodendrocytes, *EMBO Rep* **2002**, *3*, 583.
- [123] M. Takahashi, H. Kanuka, H. Fujiwara, A. Koyama, M. Hasegawa, M. Miura, T. Iwatsubo, Phosphorylation of alpha-synuclein characteristic of synucleinopathy lesions is recapitulated in alpha-synuclein transgenic Drosophila, *Neurosci Lett* **2003**, *336*, 155.
- [124] C. Lo Bianco, J. L. Ridet, B. L. Schneider, N. Deglon, P. Aebischer, alpha - Synucleinopathy and selective dopaminergic neuron loss in a rat lentiviral-based model of Parkinson's disease, *Proc Natl Acad Sci U S A* **2002**, *99*, 10813.
- [125] M. Yamada, T. Iwatsubo, Y. Mizuno, H. Mochizuki, Overexpression of alpha-synuclein in rat substantia nigra results in loss of dopaminergic neurons, phosphorylation of alpha-synuclein and activation of caspase-9: resemblance to pathogenetic changes in Parkinson's disease, *J Neurochem* **2004**, *91*, 451.
- [126] W. W. Smith, R. L. Margolis, X. Li, J. C. Troncoso, M. K. Lee, V. L. Dawson, T. M. Dawson, T. Iwatsubo, C. A. Ross, Alpha-synuclein phosphorylation enhances

- eosinophilic cytoplasmic inclusion formation in SH-SY5Y cells, *J Neurosci* **2005**, *25*, 5544.
- [127] M. Okochi, J. Walter, A. Koyama, S. Nakajo, M. Baba, T. Iwatsubo, L. Meijer, P. J. Kahle, C. Haass, Constitutive phosphorylation of the Parkinson's disease associated alpha-synuclein, *J Biol Chem* **2000**, *275*, 390.
- [128] A. N. Pronin, A. J. Morris, A. Surguchov, J. L. Benovic, Synucleins are a novel class of substrates for G protein-coupled receptor kinases, *J Biol Chem* **2000**, *275*, 26515.
- [129] E. J. Kim, J. Y. Sung, H. J. Lee, H. Rhim, M. Hasegawa, T. Iwatsubo, S. Min do, J. Kim, S. R. Paik, K. C. Chung, Dyrk1A phosphorylates alpha-synuclein and enhances intracellular inclusion formation, *J Biol Chem* **2006**, *281*, 33250.
- [130] C. E. Ellis, P. L. Schwartzberg, T. L. Grider, D. W. Fink, R. L. Nussbaum, alpha-synuclein is phosphorylated by members of the Src family of protein-tyrosine kinases, *J Biol Chem* **2001**, *276*, 3879.
- [131] B. H. Ahn, H. Rhim, S. Y. Kim, Y. M. Sung, M. Y. Lee, J. Y. Choi, B. Wolozin, J. S. Chang, Y. H. Lee, T. K. Kwon, K. C. Chung, S. H. Yoon, S. J. Hahn, M. S. Kim, Y. H. Jo, D. S. Min, alpha-Synuclein interacts with phospholipase D isozymes and inhibits pervanadate-induced phospholipase D activation in human embryonic kidney-293 cells, *J Biol Chem* **2002**, *277*, 12334.
- [132] T. Nakamura, H. Yamashita, T. Takahashi, S. Nakamura, Activated Fyn phosphorylates alpha-synuclein at tyrosine residue 125, *Biochem Biophys Res Commun* **2001**, *280*, 1085.
- [133] A. Negro, A. M. Brunati, A. Donella-Deana, M. L. Massimino, L. A. Pinna, Multiple phosphorylation of alpha-synuclein by protein tyrosine kinase Syk prevents eosin-induced aggregation, *Faseb J* **2002**, *16*, 210.
- [134] E. A. Waxman, B. I. Giasson, Specificity and regulation of casein kinase-mediated phosphorylation of alpha-synuclein, *J Neuropathol Exp Neurol* **2008**, *67*, 402.

- [135] K. E. Paleologou, A. W. Schmid, C. C. Rospigliosi, H. Y. Kim, G. R. Lamberto, R. A. Fredenburg, P. T. Lansbury, Jr., C. O. Fernandez, D. Eliezer, M. Zweckstetter, H. A. Lashuel, Phosphorylation at Ser-129 but not the phosphomimics S129E/D inhibits the fibrillation of alpha-synuclein, *J Biol Chem* **2008**, 283, 16895.
- [136] H. Sasakawa, E. Sakata, Y. Yamaguchi, M. Masuda, T. Mori, E. Kurimoto, T. Iguchi, S. Hisanaga, T. Iwatsubo, M. Hasegawa, K. Kato, Ultra-high field NMR studies of antibody binding and site-specific phosphorylation of alpha-synuclein, *Biochem Biophys Res Commun* **2007**, 363, 795.
- [137] J. R. Gillespie, D. Shortle, Characterization of long-range structure in the denatured state of staphylococcal nuclease. I. Paramagnetic relaxation enhancement by nitroxide spin labels, *J Mol Biol* **1997**, 268, 158.
- [138] P. A. Kosen, R. M. Scheek, H. Naderi, V. J. Basus, S. Manogaran, P. G. Schmidt, N. J. Oppenheimer, I. D. Kuntz, Two-dimensional ¹H NMR of three spin-labeled derivatives of bovine pancreatic trypsin inhibitor, *Biochemistry* **1986**, 25, 2356.
- [139] N. Sugeno, A. Takeda, T. Hasegawa, M. Kobayashi, A. Kikuchi, F. Mori, K. Wakabayashi, Y. Itoyama, Serine 129 phosphorylation of alpha-synuclein induces unfolded protein response-mediated cell death, *J Biol Chem* **2008**, 283, 23179.
- [140] O. S. Gorbatyuk, S. Li, L. F. Sullivan, W. Chen, G. Kondrikova, F. P. Manfredsson, R. J. Mandel, N. Muzyczka, The phosphorylation state of Ser-129 in human alpha-synuclein determines neurodegeneration in a rat model of Parkinson disease, *Proc Natl Acad Sci U S A* **2008**, 105, 763.
- [141] I. Landrieu, L. Lacosse, A. Leroy, J. M. Wieruszeski, X. Trivelli, A. Sillen, N. Sibille, H. Schwalbe, K. Saxena, T. Langer, G. Lippens, NMR analysis of a Tau phosphorylation pattern, *J Am Chem Soc* **2006**, 128, 3575.
- [142] R. J. Deshaies, J. E. Ferrell, Jr., Multisite phosphorylation and the countdown to S phase, *Cell* **2001**, 107, 819.

- [143] B. I. Giasson, M. S. Forman, M. Higuchi, L. I. Golbe, C. L. Graves, P. T. Kotzbauer, J. Q. Trojanowski, V. M. Lee, Initiation and synergistic fibrillization of tau and alpha-synuclein, *Science* **2003**, *300*, 636.
- [144] P. H. Jensen, H. Hager, M. S. Nielsen, P. Hojrup, J. Gliemann, R. Jakes, alpha-synuclein binds to Tau and stimulates the protein kinase A-catalyzed tau phosphorylation of serine residues 262 and 356, *J Biol Chem* **1999**, *274*, 25481.
- [145] S. R. Paik, H. J. Shin, J. H. Lee, C. S. Chang, J. Kim, Copper(II)-induced self-oligomerization of alpha-synuclein, *Biochem J* **1999**, *340 (Pt 3)*, 821.
- [146] D. R. Brown, Interactions between metals and alpha-synuclein--function or artefact?, *Febs J* **2007**, *274*, 3766.
- [147] K. C. Corbit, N. Trakul, E. M. Eves, B. Diaz, M. Marshall, M. R. Rosner, Activation of Raf-1 signaling by protein kinase C through a mechanism involving Raf kinase inhibitory protein, *J Biol Chem* **2003**, *278*, 13061.
- [148] S. Tabor, C. C. Richardson, A bacteriophage T7 RNA polymerase/promoter system for controlled exclusive expression of specific genes, *Proc Natl Acad Sci U S A* **1985**, *82*, 1074.
- [149] Y. S. Jung, M. Zweckstetter, Backbone assignment of proteins with known structure using residual dipolar couplings, *J Biomol NMR* **2004**, *30*, 25.

7. Appendix

7.1. Backbone assignment of wt α -synuclein at $-15\text{ }^{\circ}\text{C}$

In the following table, assigned ^1H , $^{13}\text{C}^{\alpha}$, $^{13}\text{C}'$ and ^{15}N resonances in ppm were shown.

	Residue	$^{13}\text{C}^{\alpha}$	$^{13}\text{C}'$	^1H	^{15}N
1	M	--	--	--	--
2	D	--	175.8	8.865	124.9
3	V	62.58	175.8	8.453	121.3
4	F	--	177.9	8.536	124.6
5	M	--	--	8.342	123.2
6	K	--	--	--	--
7	G	--	174	--	--
8	L	--	177.7	8.235	121.8
9	S	--	--	8.497	117.3
10	K	--	--	--	--
11	A	--	178	--	--
12	K	--	--	8.516	121.4
13	E	--	--	--	--
14	G	--	174	--	--
15	V	62.57	176	8.133	121
16	V	62.49	176	8.494	126.5
17	A	52.43	--	8.638	129.1
18	A	--	--	--	--
19	A	--	178.4	--	--
20	E	56.66	--	8.469	120.9
21	K	--	177.4	--	--
22	T	62.4	174.5	8.352	116.7
23	K	-	--	8.617	124.6
24	Q	--	175.6	--	--
25	G	-	173.7	8.639	111.1
26	V	61.84	-	8.209	120.7
27	A	54.85	178.5	8.605	128.3

28	E	55.53	176.6	8.548	121.2
29	A	54.72	--	8.474	126.3
30	A	--	178.5	--	--
31	G	45.48	--	8.412	108.1
32	K	--	173.7	--	--
33	T	-	--	8.459	116
34	K	--	-	--	--
35	E	56.67	176.8	8.607	110.8
36	G	45.26	173.8	8.611	110.7
37	V	-	176.7	8.085	120.4
38	L	56.95	-	8.508	127.3
39	Y	57.81	175.2	8.236	125.1
40	V	61.8	175.8	8.192	125.1
41	G	45.26	--	8.091	112.8
43	K	--	176.8	--	--
44	E	56.52	--	8.608	122.8
45	K	-	176.8	8.645	124.6
48	V	62.17	175.9	8.085	120.7
49	V	62.06	175.8	8.518	126.5
50	H	56.43	--	8.711	125.9
51	G	--	173.6	--	--
52	V	61.83	175.9	8.212	120.4
53	A	52.28	177.8	8.678	129.1
54	T	61.79	174.3	8.456	116.1
55	V	62.14	176.3	8.531	124.3
56	A	52.31	177.8	8.624	129.1
57	E	56.27	176.6	8.558	121.6
58	K	56.22	177	8.646	124.2
59	T	61.9	174.5	8.409	116.7
60	K	56.5	176.5	8.579	124.4
61	E	55.58	176.5	8.608	122.5
62	Q	-	175.9	8.596	122.3
63	V	62.29	176.7	8.488	123.1
64	T	61.84	173.9	8.514	118.2
65	N	52.88	175.2	8.697	122.3
66	V	62.37	176.9	8.444	121.6

7. Appendix

67	G	45.48	174.5	8.742	113.4
68	G	45.14	173.5	8.367	109.2
69	A	52.1	177.5	8.326	124.1
70	V	-	176.3	8.402	121.3
71	V	62.04	176.3	8.631	126.9
72	T	61.83	174.8	8.515	119.3
73	G	45.37	173.8	8.617	112.1
74	V	62.12	176.7	8.269	120.3
75	T	61.73	--	8.511	119.5
76	A	--	-	--	--
77	V	62.03	173.9	8.391	121.4
78	A	52.24	177.6	8.599	128.5
79	Q	56.73	175.9	8.598	121.1
80	K	56.26	176.9	8.536	120.7
81	T	62.02	176.6	8.444	117.3
82	V	62.13	176.1	8.628	124.9
83	E	56.6	176.9	8.762	126.3
84	G	45.36	174	8.717	111.4
128	P	62.82	176.7	8.697	117.7
129	S	58.14	174.7	8.691	117.5
130	E	56.23	176.6	8.756	123.7
131	E	-	176.8	8.587	122.7
132	G	-	173.5	8.566	110.6
133	Y	-	175.7	8.23	120.8
134	Q	55	174.6	8.396	123.6
135	D	54	175.5	8.367	122.1
136	Y	57.47	175	8.223	121.3
133	Y	-	175.7	8.23	120.8
134	Q	55	174.6	8.396	123.6
135	D	54	175.5	8.367	122.1
137	E	53.33	-	8.404	126.1
138	P	62.62	176.7	8.698	122.3
139	E	56.33	175.4	8.69	122.2
140	A	53.71		8.232	131.6

7.2. Backbone assignment of the C2A domain of Rabphilin-3A using the automatic assignment program MARS

The gene coding for the C2A domain of mouse rabphilin3A (E371-I510) was cloned into the *Bam*HI and *Eco*RI restriction sites of pGex2T (Novagen, Madison, USA) in order to produce GST-tagged recombinant protein in *E. coli* BL21. The protein was purified by affinity chromatography on a Glutathione sepharose resin (Amersham Biosciences) and the GST tag was removed on column by a thrombin-protease cleavage. The protein was further purified by anion exchange chromatography on a HiTrap SP-Sepharose column (Amersham Biosciences). ¹⁵N/¹³C labeled protein sample was prepared from cells grown in M9-based minimal medium containing ¹⁵NH₄Cl and ¹³C₆-glucose. NMR samples contained approximately 1 mM rabphilin3A C2A domain in 20 mM sodium acetate pH 5.0, 150 mM NaCl, 1 mM DTT, 20 mM calcium chloride and 10 % D₂O (v/v).

NMR spectra were acquired at 301 K on Bruker AVANCE 600, 700 and 900 spectrometers, processed using NMRPipe/NMRDraw^[66] and analyzed using Sparky (T. D. Goddard and D. G. Kneller, University of California, San Francisco). Assignments were derived from standard versions of 2D ¹⁵N-¹H HSQC, 3D HNCA, 3D HN(CO)CA, 3D CBCA(CO)NH, 3D HNCACB, 3D HNCO experiments. Chemical shifts of all proton, carbon and nitrogen nuclei were referenced externally to that of DSS at 0 ppm. The backbone resonance assignment was largely performed by using the automatic assignment program MARS^[149].

The chemical shift data have been deposited in the BioMagResBank (BMRB) <http://www.bmrb.wisc.edu> under accession number 6787. In the following table,

7. Appendix

assigned ^1H , ^{15}N , $^{13}\text{C}^\alpha$, $^{13}\text{C}^\beta$ and $^{13}\text{C}'$ backbone resonances were shown of the 139 amino acids of the mouse rabphilin-3A C2A domain (C2A₃₇₁₋₅₁₀).

Residue	$^{13}\text{C}'$	$^{13}\text{C}^\alpha$	^1H	^{15}N	$^{13}\text{C}^\beta$
E	176.6	54.18	8.68	122.95	27.14
A	177.75	50.93	8.28	124.66	16.39
N	175.44	50.5	8.29	117.66	36.53
S	174.49	55.67	8.12	115.98	61.07
Y	175.79	55.24	8.13	121.76	36.02
D	176.42	51.52	8.19	122	38.48
S	174.84	55.87	8.13	116.16	61.29
D	176.89	52.02	8.38	122.32	38.32
E	176.91	54.21	8.22	120.86	27.33
A	178.39	50.33	8.25	124.08	16.4
T	175.3	59.09	8	112.08	67.38
T	174.76	59.35	8.03	116.65	67.18
L	176.23	53.44	8.41	122.33	41.05
G	172.75	41.32	7.39	103.36	-
A	175.95	47.98	8.25	121.21	19.91
L	173.91	51.3	9.08	122.16	45.76
E	176.14	51.81	9.23	125.31	29.95
F	172.17	52.85	8.56	119.85	38.91
S	173.98	53.69	9.55	114.71	64.04
L	175.25	50.71	9	122.66	46.11
L	174.38	52.18	8.43	119.91	43.92
Y	173.17	52.07	9.97	129.17	36.21
D	175.91	48.89	8.72	129.15	37.81
Q	178.82	56.1	7.24	125.69	26.98
D	177.69	54.67	8.68	119.76	37.37
N	173.7	50.26	7.1	113.67	37.3
S	173.47	56.04	7.8	114.85	59.02
N	173.75	48.62	7.68	115.54	40.31
L	174.27	51.1	8.73	125.49	42.8

Q	175.43	52.18	9.48	125.95	28.01
C	174.07	53.58	9.25	125.63	26.14
T	174.03	59.64	9.51	126.19	66.8
I	175.15	56.23	9.29	129.15	31.98
I	176.41	63.01	8.35	128.67	36.24
R	172.86	51.99	8.09	110.85	30.57
A	175.97	47.52	8.89	120.31	20.07
K	177.44	51.76	8.74	118.87	33.87
G	174.96	44.54	8.64	112.66	-
L	176.94	52.11	8.27	116.11	39.76
K	176.42	51.81	6.97	123.73	31.89
P	178.46	-	-	-	-
M	176.13	50.35	8.08	119.98	31.14
D	-	49.98	7.64	123.09	42.7
S	174.47	-	-	-	60.13
N	176.25	50.06	7.65	118.65	34.52
G	174	42.7	8.2	107.4	-
L	173.3	49.85	7.94	120.13	39.83
A	174.31	48.78	7.28	120.23	18.33
D	176.97	49.28	8.5	117.95	39.77
P	177.11	60.29	-	-	31.42
Y	171.77	53.81	8.79	116.55	39.26
V	174.7	57.73	7.98	120	30.81
K	174.81	52.23	9.06	124.85	33.61
L	176.44	50.94	8.74	123.57	42.14
H	173.51	52.02	8.77	119.91	31.58
L	175.09	51.68	8.1	127.11	40.6
L	175.29	-	8.98	124.85	41.51
P	176.82	60.27	-	-	32.15
G	174.04	43.41	8.51	109.25	-
A	178.53	50.07	8.48	126.16	16.77
S	176.17	57.21	8.26	115.15	61.15
K	177.94	55.89	8.58	123.06	29.8
S	174.83	56.55	8.07	114.05	60.93

7. Appendix

N	175.68	51.64	8.16	119	36.42
K	175.4	53.62	8.15	123.71	31.04
L	175.7	51.15	8.34	123.43	43.64
R	175.95	52.34	8.35	117.28	30.74
T	175.84	58.42	8.57	110.43	70.41
K	177.61	54.59	9.94	121.21	30.39
T	175.1	59.87	8.86	121.16	67.75
L	174.95	50.45	8.51	130.82	40.48
R	177.57	52.24	7.93	116.15	28.9
N	175.7	51.36	9.27	118.93	34.48
T	180.98	58.21	8.89	112.23	66.27
R	174.69	52.2	8.69	122.19	28.99
N	175.31	48.98	8.6	117.74	38.69
P	174.98	59.95	-	-	30.54
V	175.26	59.29	7.38	119.46	30.12
W	176.63	59.67	8.01	124.34	27.1
N	174.42	51.86	8.94	117.83	35.58
E	175.26	53.31	8.19	118.37	32.01
T	173.27	61.52	9.07	122.54	66.76
L	175.36	50.59	9.07	131.25	41
Q	174.11	51.95	8.42	119.59	31.53
Y	175.68	55.1	8.79	121.15	38.27
H	174.66	51.35	8.92	120.76	27.97
G	174.49	43.98	8.9	112.09	-
I	176.23	55.42	7.88	121.07	34.78
T	175.67	58.46	9.01	120.56	70.03
E	179.34	57	9.02	120.49	26.31
E	179.22	56.97	8.1	118.67	26.65
D	178.71	54.93	7.59	120.07	38.69
M	177.62	53.02	7.55	117.16	26.82
Q	178.31	54.27	7.29	112.13	26.57
R	177.96	54.24	7.51	115.36	30.68
K	176.45	54.91	8.07	117.77	32.44
T	172.13	59.6	9.1	117.66	69.97

L	174.35	50.79	9.04	126.31	42.56
R	174.65	52.73	9.25	129.25	30.03
I	174.81	58.55	8.78	129.86	36.4
S	172.61	54.96	9.01	120.2	62.42
V	175.21	58.81	9.13	124.42	28.89
C	180.98	54.93	8.75	125.69	29.29
D	174.73	48.82	9.16	119.2	42.33
E	-	54.89	9.49	128.05	29
D	174.73	49.9	8.5	117.79	39.45
K	177.32	54.67	8.03	118.81	30.6
F	176.72	56.33	8.61	116.36	34.05
G	174.71	43.17	8.4	106.9	-
H	173.47	52.31	7.56	118.97	26.9
N	174.42	50.33	8.48	120.23	40.01
E	175.88	52.41	8.93	118.77	31.69
F	175.08	56.4	8.97	123.96	38.05
I	175.55	61.57	8.78	124.25	36.06
G	180.65	43.82	7.13	99.82	-
E	174.99	51.77	9.69	117.48	32.28
T	171.44	59.03	8.83	113.05	67.27
R	175.48	52.01	8.21	123.1	30.46
F	174.28	54.98	9.07	123.94	40.06
S	173.58	56.26	8.23	125.62	60.09
L	177.74	55.31	7.42	127.15	37.65
K	177.31	55.4	8.02	119.2	28.9
K	177.21	54.13	7.49	117.21	30.18
L	175.92	51.73	7.75	121.85	41.04
K	177.18	52.45	8.82	125.47	30.75
A	177.69	51.44	8.92	126.53	16.69
N	173.89	52.54	9.33	114.05	34.47
Q	175.14	52.14	7.7	117.85	28.08
R	175.8	54.2	9.08	131.25	27.61
K	173.64	52.09	8.8	128.51	33.45
N	174.09	50.03	8.3	123.31	37.85

F	175.09	54.59	8.82	119.08	40.07
N	174.93	50.51	8.5	121.88	36.74
I	175.85	55.79	8.83	120.29	40.58
C	174.94	56.73	8.73	122.83	25.12
L	175.8	52.63	8.47	124.31	40.67
E	176.11	51.95	9.15	118.85	30.79
R	175.9	53.63	8.48	119.73	28.63
V	176.12	59.77	8.38	121.97	29.62
I	176.2	58.3	8.1	126.31	36.25

7.3. Protocol of the automatic assignment program MARS

MARS is a program for robust automatic backbone assignment of $^{13}\text{C}/^{15}\text{N}$ labeled proteins. MARS simultaneously optimizes the local and global quality of assignment to minimize propagation of initial assignment errors and to extract reliable assignments ^[149]. More detail information and program can find following link:

http://www.mpibpc.mpg.de/groups/griesinger/zweckstetter/links/software_mars.htm

◆ How to run MARS

1. Prepare your chemical shift table.
2. Get your primary sequence in FASTA format.
3. Get a secondary structure prediction using the Psipred web server.
4. Adjust the parameter setup file (mars.inp).
5. Type 'runmars mars.inp'



◆ Input

MARS is a program for backbone assignment of $^{13}\text{C}/^{15}\text{N}$ labeled proteins. Following input is required:

1. Parameter setup file (mars.inp)
2. Chemical shift table (SPARKY format)
3. Primary sequence (FASTA format)
4. Secondary structure prediction file (PSIPRED format)
5. PDB file

◆ **Output**

1. Assignment result filtered for high, medium and low reliability ('assignment_AA.out').
2. Assignment result including alternative assignments that show up with a 10 % probability ('assignment_AAs.out').
3. The most likely assignment for each pseudo residue ('assignment_PR.out').
4. Summary of all possible connectivities ('connectivity.out').
5. Summary of reduced possible connectivities ('connectivity_reduced.out').
6. Chemical shift table with updated assignments that can be read into Sparky ('sparky_all,out').
7. Detailed information about predicted chemical shifts, number of reliable assignments, number of constraints for each pseudo residue, matrices matching experimental and back-calculated chemical shifts and/or RDCs and pseudoenergy matrices at each iteration step ('mars.log').

◆ **C2A input files to run MARS**

1. A Mars run is controlled by the parameter setup file (mars.inp). This has to be adjusted to the available experimental data. Please see below for a detailed description

of the parameters. Lines with a '#' sign as first character as well as empty line are ignored. Do not change the variable names such as nIter.

mars.inp

```
# Input file for the assignment program MARS
fragSize:      5                # Maximum length of pseudoresidue fragments
cutoffCO:      0.2              # Connectivity cutoff (ppm) of CO [0.25]
cutoffCA:      0.3              # Connectivity cutoff (ppm) of CA [0.5]
cutoffCB:      0.5              # Connectivity cutoff (ppm) of CB [0.5]
cutoffHA:      0.2              # Connectivity cutoff (ppm) of HA [0.25]
fixConn:       NO               # Table for fixing sequential connectivity
fixAss:        NO               # Table for fixing residue type and(or) assignment
pdb:           0                # 3D structure available [0/1]
resolution:    NO               # Resolution of 3D structure [Angstrom]
pdbName:       NO               # Name of PDB file (protons required!)
tensor:        4                # Method for obtaining alignment tensor [0/1/2/3/4]
nIter:         2                # Number of iterations [2/3/4]
dObsExh:       NO               # Name of RDC table for exhaustive SVD (PALES
format)
dcTab:         NO               # Name of RDC table (PALES format)
deuterated:    0                # Protonated proteins [0]; perdeuterated proteins [1]
sequence:      c2a.fasta        # Primary sequence (FASTA format)
secondary:     c2a.pspred       # Secondary structure (PSIPRED format)
csTab:         c2a.tab          # Chemical shift table
```

2. The chemical shift table follows the SPARKY format. It consists of a header, pseudo residues and chemical shifts. The header has to be defined before the listing of chemical shift values starts and includes the variable names for the chemical shifts. Currently 10 different chemical shifts are supported and should be indicated by 'CA', 'CA-1', 'CB', 'CB-1', 'CO', 'CO-1', 'HA', 'HA-1', 'H' and 'N'. These variable names have to be in the same order as the columns for the different chemical shifts.

C2A.tab

	CA	CA-1	CB	CB-1	CO-1	HN	N
1	51.87	59.68	35.52	27.12	176.7	8.939	117.8
g1	56.08	56.11	37.85	37.74	175.1	8.787	124.1
2	54.46	49.74	40.02	37.62	174.1	8.824	119.1
g2	56.35	55.41	60.91	29.56	177.8	8.069	113.9
3	49.52	-	33.83	20.22	176	8.742	118.8
g3	56.39	49.78	61.1	16.95	178.4	8.253	115
4	48.74	48.44	39.73	18.31	174.4	8.506	117.8
5	52.04	51	30.85	43.49	175.7	8.341	117.2
g5	54.83	54.56	34.03	30.34	177.4	8.609	116.3
6	50.35	49.93	36.32	16.52	177.8	8.284	117.6
g6	52.05	50.33	28.87	40.39	175	7.929	116.1
7	51.99	44.33	39.68	-	175	8.266	116
g7	48.82	52.23	38.68	28.95	174.6	8.597	117.6
8	55.67	50.46	61.34	36.4	175.1	8.167	116.7
g8	52.29	50.22	31.8	39.71	174.5	8.93	118.7
9	55.86	51.14	61.21	38.21	176.4	8.127	116.1
g9	48.78	54.62	42.3	29.05	180.9	9.155	119.1
10	55.44	50.52	61.11	36.32	175.5	8.123	115.9
g10	51.77	52.09	34.49	28.7	177.6	9.275	118.9
11	59.47	59.09	67.05	67.24	175.2	8.031	116.5
g11	51.37	56.38	36.33	60.86	174.9	8.162	118.9
12	55.86	49.8	58.9	37.08	173.6	7.806	114.7
g12	54.31	49.66	30.59	39.29	174.7	8.032	118.8
13	48.46	55.88	40.24	58.92	173.4	7.689	115.5
g13	50.01	58.27	34.42	60.01	174.5	7.651	118.6
14	54.19	54.22	30.67	26.17	178.2	7.515	115.3
g14	51.96	42.99	26.9	-	174.9	7.559	118.9
15	51.55	43.67	32.73	-	180.5	9.697	117.4
g15	48.44	49.62	18.3	39.44	173.2	7.282	120.2
16	51.85	52.26	30.76	40.42	176.1	9.15	118.8
g16	50.38	61.05	31.22	29.12	178.3	8.077	120
17	54.38	57.92	62.36	36.03	174.9	9.014	120.1

7. Appendix

g17	49.58	42.57	39.53	-	174	7.936	120.1
18	56.85	57.93	26.28	69.71	175.8	9.022	120.4
g18	49.64	50.38	42.69	31.14	176.2	7.647	123.1
19	51.74	54.92	28.03	38.05	175.7	8.916	120.7
g19	51.79	52.09	31.9	39.44	176.9	6.972	123.7
20	47.5	51.74	20.25	30.36	172.9	8.893	120.3
g20	56.11	52.31	37.95	31.43	175.9	8.969	124
21	55.7	50.4	40.28	36.45	175	8.832	120.3
g21	55.72	56.44	45.41	61.1	176.1	8.571	123
22	51.79	50.88	31.67	42.05	176.5	8.779	119.9
g22	49.77	43.24	17	-	174	8.48	126.1
23	54.46	56.05	37.3	26.66	178.7	8.674	119.7
g23	55.63	54.81	60.04	39.89	174.3	8.227	125.6
24	53	51.7	38.87	29.71	176.1	8.563	119.8
g24	43.16	55.03	-	33.79	176.6	8.394	106.8
25	53.41	51.9	28.61	30.5	176	8.483	119.7
26	-	50.61	43.91	45.9	175.3	8.434	119.8
g26	54.89	48.54	29	42.24	174.9	9.491	128.1
27	51.89	50.33	30.26	40.79	175.4	8.423	119.6
g27	43.87	61.41	-	35.64	175.5	7.136	99.67
28	50.26	51.95	39.97	26.6	173.5	8.471	120.2
g28	58.27	52.1	70.16	30.69	175.9	8.568	110.3
29	59.95	54.54	67.43	30.16	177.8	8.853	121.1
g29	51.8	62.93	30.62	35.88	176.5	8.097	110.7
30	54.93	51.79	38.25	30.1	174.1	8.799	121.1
g30	59.13	50.14	67.29	16.61	178.3	8.002	111.9
31	53.23	51.78	32.12	35.3	174.5	8.189	118.3
g31	54.25	52.96	26.52	26.49	177.6	7.294	112
32	54.67	54.15	32.54	30.44	177.9	8.065	117.7
g32	49.82	54.43	37.29	37.09	177.6	7.104	113.6
33	57.05	56.88	26.4	25.97	179.2	8.097	118.6
g33	53.51	53	63.82	38.77	172.1	9.556	114.6
34	54.97	55.21	28.84	37.37	177.8	8.021	119.1
g34	51.03	51.07	34.43	16.88	177.7	9.333	113.9

35	57.62	53.57	30.84	38.93	171.9	7.981	120
g35	43.99	51.56	-	27.77	174.4	8.887	112.1
36	51.98	52.37	28.08	34.18	173.9	7.704	117.8
g36	59.09	51.5	67.04	32.3	174.9	8.831	112.9
37	52.9	54.98	26.76	38.46	178.7	7.55	117.1
g37	58.13	51.56	66.05	34.21	175.5	8.885	112.1
38	54.03	55.21	30.12	28.62	177.3	7.486	117.1
g38	44.55	51.74	-	33.53	177.5	8.648	112.5
39	59.24	59.73	30.22	30.11	175.1	7.371	119.4
g39	53.42	59.89	39.11	31.18	176.9	8.791	116.4
40	54.98	56.87	38.58	26.16	179.3	7.586	120
g40	59.08	54.75	69.55	32.29	176.5	9.101	117.6
41	54.49	58.11	30.4	70.22	175.9	9.946	121.2
42	51.13	47.79	45.47	20.01	176.1	9.082	122.1
43	60.35	53.29	66.67	31.84	175.3	9.063	122.5
44	50.66	53.77	46.09	63.87	174	8.998	122.6
45	52.18	58.08	29	66.05	180.8	8.69	122.1
46	56.85	55.68	25.08	40.15	175.8	8.728	122.8
47	51.05	51.76	42.1	33.34	174.8	8.746	123.5
49	50.4	54.42	36.69	39.89	175.2	8.491	121.8
50	59.9	53.51	29.41	28.4	176.1	8.378	122
51	53.3	59.49	40.76	67.29	174.7	8.421	122.3
52	51.88	55.97	38.24	61.19	174.9	8.38	122.3
53	50.45	58.07	36.34	35.95	176	8.418	122.8
54	47.89	41.14	20.06	-	172.6	8.251	121.2
55	54.15	51.85	27.2	38.25	176.8	8.22	120.8
56	51.38	55.15	38.41	35.78	175.8	8.187	122
57	55.3	55.72	36	61.12	174.5	8.13	121.7
58	55.35	43.83	34.56	-	174.4	7.882	121
59	51.65	54.02	41.03	29.91	177.2	7.757	121.8
60	50.96	53.45	43.65	30.83	175.4	8.336	123.4
61	49.73	52.04	37.77	33.15	173.7	8.296	123.3
62	51.86	59.05	30.49	67.1	171.5	8.207	123.1
63	57.35	55.54	62.07	61.25	173.9	7.917	123

7. Appendix

64	59.7	53.42	66.61	25.74	174.2	9.512	126.2
65	51.95	50.99	28.06	42.7	174.3	9.483	126
66	53.45	52	26.01	27.83	175.3	9.255	125.6
67	51.59	51.07	29.84	45.28	173.9	9.231	125.3
68	58.88	54.37	28.78	62.35	172.7	9.137	124.4
69	54.72	51.87	40.03	30.21	175.5	9.074	123.9
70	51.78	57.6	33.54	30.66	174.7	9.065	124.8
71	49.26	51.56	41.43	40.4	175	8.978	124.9
72	50.6	59.07	42.47	69.6	172.2	9.048	126.3
73	51.05	52.32	16.88	30.44	177.2	8.92	126.5
74	52.05	51.63	30.69	40.9	176	8.811	125.4
75	50.92	48.49	42.84	40.13	173.8	8.744	125.5
76	52.18	56.63	40.54	24.74	175	8.474	124.3
77	49.95	54.07	16.51	26.74	176.6	8.272	124.6
78	50.16	54.09	16.56	27.2	176.8	8.247	124.2
79	53.42	51.37	31.02	36.11	175.7	8.146	123.7
80	59.6	59.11	27.1	30.09	175.3	8.012	124.3
81	41.39	53.35	-	40.89	176	7.394	103.3
82	56.09	48.58	26.97	37.57	175.9	7.243	125.7
83	55.4	55.65	37.52	59.94	173.6	7.424	127.2
84	58.31	59.62	36.15	29.3	176.2	8.102	126.3
85	51.63	51.84	40.55	31.49	173.7	8.107	127.1
86	52.01	52.13	36.21	43.7	174.4	9.975	129.2
87	56.07	59.54	32.13	66.76	174.1	9.289	129.2
88	52.76	50.71	29.99	42.29	174.3	9.254	129.3
89	50.46	60.23	40.97	66.8	173.3	9.081	131.5
90	54.34	51.94	27.66	27.87	175.2	9.065	131.5
91	51.97	54.25	33.4	27.26	175.8	8.798	128.5
92	48.8	52.02	37.65	35.96	173.2	8.723	129.2
93	58.44	52.73	36.24	29.79	174.7	8.78	129.9
94	50.42	59.85	40.49	67.45	175	8.512	131
95	63.09	56.1	36.12	31.87	175.2	8.358	128.7
96	42.72	50.01	-	34.17	176.2	8.2	107.3
180	57.8	55.28	69.69	34.36	176.2	9.009	120.5

750	54.56	58.76	29.2	28.54	175.3	8.733	125.6
1090	43.45	59.62	-	31.81	176.8	8.503	109.1

Any combination of characters can be pseudo residue names but the number of characters of the name has to be less than 25.

3. The primary sequence of the protein has to be in FASTA format. IMPORTANT: 'X' and 'Z' can not be used for the characters of a sequence.

C2A.fasta.tab

```
EANSYDSDEATTLGALEFSLLYDQDNSNLQCTIIRAKGLKPMDSNGLADPYVKLHLLPGASKSN
KLRTKTLRNTRNPVWNETLQYHGITEEDMQRKTLRISVCDEDKFGHNEFIGETRFSLKKLLKANQ
RK NFNICLERVI NSS
```

4. Secondary structure prediction table has to be in Psipred format. Use the Psipred web server to get the table.

C2A.psipred

PSIPRED PREDICTION RESULTS

Key

Conf: Confidence (0=low, 9=high)

Pred: Predicted secondary structure (H=helix, E=strand, C=coil)

AA: Target sequence

PSIPRED HFORMAT (PSIPRED V2.3 by David Jones)

Conf: 964457878644178999999738998799999835887435877587967999986589

Pred: CCCCCCCCCCEEEEEEEEEEECCCCEEEEEEEECCCCCCCCCCCCCEEEEEEECC

AA: EANSYDSDEATTLGALEFSLLYDQDNSNLQCTIIRAKGLKPMDSNGLADPYVKLHLLPGA
10 20 30 40 50 60

Conf: 987223302271799981376888865071320786799998548899876046799874

Pred: CCCEEEEEEEECCCCCCCCCEEEEEEECHHHHCCCEEEEEEECCCCCCCCCEEEEEEE

AA: SKSNKLRTKTLRNTRNPVWNETLQYHGITEEDMQRKTLRISVCDEDKFGHNEFIGETRFS
70 80 90 100 110 120

Conf: 34478998577877233343689

Pred: HHHCCCCCEEEEECCCCCCCC
AA: LKCLKANQRKNFNICLERVINSS
130 140

7.4. Pulse programs of PG-SLED and (HA)CANNH

◆ PG-SLED

```
;PG-SLED diffusion experiment according to Dobson in JBNMR
;set up by Markus Zweckstetter on 06-30-2004
;based on ledbpgp2s
;avance-version (03/04/24)
;2D sequence for diffusion measurement using stimulated
; echo and LED
;using bipolar gradient pulses for diffusion
;using 2 spoil gradients
;D. Wu, A. Chen & C.S. Johnson Jr.,
; J. Magn. Reson. A 115, 260-264 (1995).
#include Grad.incl
#include Delay.incl
define list: gradient diff: Difframp
"p2=p1*2"
"d12=20u"
"d16=1.0m"
"d30=50m"
"p30=6.3m"
"p19=6.3m"
"DELTA1=d20-p1*2-p2-p30*2-d16*2-p19-d16-d12*3-4u"
"DELTA2=d21-p19-d16-4u"
1 ze
2 d30
d12 pl9:f1
d1 cw:f1 ph29
4u do:f1
d12 pl1:f1
50u UNBLKGRAD
p1 ph1
p30:gp6*diff
d16
; p2 ph1
; p30:gp6*-1*diff
; d16
```

```
p1 ph1
p19:gp7
d16
d12 pl9:f1
d12 cw:f1 ph29
DELTA1
4u do:f1
d12 pl1:f1
p1 ph1
p30:gp6*diff
d16
;p2 ph1
;p30:gp6*-1*diff
;d16
p1 ph2
p19:gp8
d16
DELTA2
4u BLKGRAD
p1 ph2
go=2 ph31
d30 mc #0 to 2 F1QF(igrad diff)
exit
ph1= 0 0 1 1 2 2 3 3
ph2= 0 2 1 3 2 0 3 1
ph29= 0
ph31= 0 0 1 1 2 2 3 3
;p11 : f1 channel - power level for pulse (default)
;p1 : f1 channel - 90 degree high power pulse
;p2 : f1 channel - 180 degree high power pulse
;p19: gradient pulse 2 (spoil gradient)
;p30: gradient pulse (little DELTA * 0.5)
;d1 : relaxation delay; 1-5 * T1
;d16: delay for gradient recovery
;d20: diffusion time (big DELTA)
;d21: eddy current delay (Te) [5 ms]
;NS: 8 * n
;DS: 4 * m
;td1: number of experiments
;FnMODE: QF
; use xf2 and DOSY processing
;use gradient ratio: gp 6 : gp 7 : gp 8
```

7. Appendix

```
;          100 : -17.13 : -13.17
;for z-only gradients:
;gpz6: 100%
;gpz7: -17.13% (spoil)
;gpz8: -13.17% (spoil)
;use gradient files:
;gpnam6: SINE.100
;gpnam7: SINE.100
;gpnam8: SINE.100
;use AU-program dosy to calculate gradient ramp-file Difframp
;$Id: ledbpp2s,v 1.3.2.1 2003/05/06 12:40:00 ber Exp $
```

◆ (HA)CANNH

```
include "bits.mz"
#include Avance.incl
#include Grad.incl
;started from hnca-ge.abx
;hcannh-3D with grad enhancement 1/7/00
;p1 = 90 deg (10us) 1H pulse @p1
;p30 = 90 deg (60us) 1H pulse @p130
;p7 = 90 deg (50us) 15N pulse @p17
;p31 = 90 deg (180us) 15N pulse @p131
;p5 = selective 90 deg (53.0us) 13CA pulse @p15
;p4 = selective 180 deg (23.7*2us) 13CA pulse @p14
;p6 = 180 deg (191.7us=180deg) 13C pulse @sp1 using sinc1.0
;p6 = 90 deg (191.7us=90deg) 13C pulse @sp2 using sinc1.0
#define NITRO
#define CA          ; selection by hand
;#define BS
define loopcounter NLOOP
define loopcounter CLOOP
"NLOOP=26"          ;maximum "NLOOP=76"
"CLOOP=44"         ;maximum "CLOOP=126"
"d11=50m"
```

```

"d12=1m"
"d20=p7-p4"
"d21=p7-p1"
"d28=p4-p1"
;Gradient pulses
"p17=0.75m"
"p20=1.5m"
"p21=1.1m"
"p22=1.0m"
"p23=1.0m"
"p24=0.200m"
"p25=0.074m"           ; optimization of gradient selection
"p26=2.705m"
"p27=2.705m"
"p28=2.0m"
;"p29=1.5m"
"d2=1.5m-p21"
"d3=2.65m-p22"
"d4=2.65m-p23"
"d6=0.25m-p24"
"d7=0.25m-p25"
"d15=1.5m-p17"
;----Carbon Evolution-----
"d10 = 8u"
;"d16 = 14m-0.63661977*p5-4u-d10-p21-p6-p7"
;"d17 = 14m-0.63661977*p5-11u-p21-p7"
;--- if BS compensating pulse is used
"d16 = 14m-0.63661977*p5-4u-p6-p21-p7-d10"
"d17 = d16+d10-8u-4u"
;----Nitrogen Evolution-----
; !!!! all increment MUST satisfy the following relations
; ***** in22 = in25  &&  in18 = in24 + in25 *****

```

7. Appendix

```
"d22=7m-p6*0.5"      ;d22 =6.25m for in22 = 125u and 50 incs
"d18=d22-5.5m"      ;in18 = 225u
"d25=d22-p4*2-d24-5u" ;in25 = 125u
"d24=5u"            ;in24 = 100u for 15N incr of 700u
"d19=5.4m-p26-300u-10u-p1"

1      ze
      d12
      10u
      10u ru1
      10u ru2

;----- selection by hand
;      10u iu2      ; for recording 2D IP-(H)CA(N)NH spectrum
;      d12 dp14    ; if 2D (HCA)NNH, as Sx is required instead of Sy
;-----
      10u

2      10u
      1m
      d11 do:N
      d12

3      d12*4.0
4      d12*5.0
5      d12*5.0
6      d12*4.0 do:N
7      5u do:C1
      10u p14:C1
      d1 BLKGRAD
      1m UNBLKGRAD
      10u p11:H
      10u p17:N

;----- removal of boltzmann magnetization ---
      (p7 ph7):N (p4 ph0):C1
      2u
      p20:gp20
```

```
1.0m
;----- INEPT HA -> CA -----
    (p1 ph0):H
10u
p21:gp21
    d2
    (d28 p1*2 ph1):H (p4*2 ph8):C1
10u
p21:gp21
    d2
    (p1 ph2):H
10u
;----- flip back -----
; problems with water flip back !!
;     if "l2==1" goto 13
;     (p2 ph0):H
;     if "l2==2" goto 14
;13  (p2 ph20):H
;14  50u p11:H
    300u p15:C1
;----- IPAP selection -----
    if "l2==1" goto 15
    (p5 ph0):C1
    2u
    p17:gp20
    d15 p14:C1
    (p4*2 ph5):C1 (d28 p1*2 ph0):H
    2u
    p17:gp20
    d15 p15:C1
    (p5 ph3):C1
    4u
```

7. Appendix

```
p20:gp20
1m
(p5 ph14):C1
2u
if "l2==2" goto 16
15 20u ; symmetry gradients
p17:gp20
d15
p17:gp20
d15
p20:gp20
1m

(p5 ph0):C1
2u
;----- end IPAP selection -----
;----- CT evolution on CA -----
16 d10
(p6:sp1 ph0):C1 ;carbonyl decoupling with sinc
2u
p21:gp19
d16 pl4:C1
(d20 p4*2 ph13):C1 (p7*2 ph0):N
2u
p21:gp19
d17 pl5:C1
4u
(p6:sp1 ph0):C1 ;BS compensating pulse
2u
8u pl5:C1
(p5 ph6):C1
5u
```

```

p28:gp28
    300u pl5:C1
(p1 ph1):H          ;trim H decoup on
5u pl30:H
5u cpds1:H
;----- CT evolution on N -----
    (p7 ph10):N
    d22
    (p6:sp1 ph0):C1          ;carbonyl decoupling with sinc
    d22
    (p7*2 ph7):N
    d24
5u pl4:C1
    (p4*2 ph0):C1
    d25
    (p6:sp1 ph0):C1          ;carbonyl decoupling with sinc
    d18
    0.1m do:H                ;H decoupling off
10u pl1:H
(p1 ph3):H          ;trim pulse
d19 pl1:H
;alternating Rance-Kay coherence encoding
    if "l1==1" goto 10
    if "l1==2" goto 20
10    p26:gp26                ;coherence encoding gradient
    100u
    goto 30
20    p27:gp27                ;coherence encoding gradient
    100u
30    200u pl1:H
;end coherence encoding
    (p7 ph9):N (d21 p1 ph0):H

```

7. Appendix

```
;----- Rance-Kay transfer N -> HN -----  
    2u  
p22:gp22  
    d3  
    (d21 p1*2 ph0):H (p7*2 ph7):N  
    2u  
p22:gp22  
    d3  
    (p1 ph1):H (p7 ph8):N  
    2u  
p23:gp23  
    d4  
    (d21 p1*2 ph0):H (p7*2 ph7):N  
    2u  
p23:gp23  
    d4  
    (d21 p1 ph0):H (p7 ph0):N  
    4u  
p24:gp24  
    d6  
    (p1*2 ph0):H  
    2u  
p25:gp25  
    d7 pl31:N  
    (2u ph0)  
    go=2 ph31 cpd2:N  
10u do:N  
    1m BLKGRAD  
    d11 wr #0 if #0 zd  
;----- selection by hand  
d12 iu2                ; 3D IPAP selection  
lo to 3 times 2
```

```
d12 ru2
;-----
#ifdef NITRO
d12 ip9
d12 ip9
d12 iu1
lo to 4 times 2
d12 ru1
d12 dd22
d12 id18
d12 id24
d12 id25
lo to 5 times NLOOP
d12 rd22
d12 rd24
d12 rd25
d12 rd18
#endif
#ifdef CA
d12 ip6
lo to 6 times 2
d12 id10
d12 dd17
d12 ip31
d12 ip31
lo to 7 times CLOOP
#endif
#ifdef BS
d12 ip13
lo to 7 times td1
#endif
d12
```

7. Appendix

d12 do:C1

d12 do:N

exit

ph0=0

ph1=1

ph2=1 3

;ph2=3

ph3=3

ph5=0

;ph6=0 2

ph6=0

ph7=0

ph8=1

ph9=2

ph10=0 0 2 2

ph11=0

ph13=0

;ph13=(360) 11 ;BS compensation

ph14=2

ph20=2

ph31=0 2 2 0

Curriculum Vitae

Persönliche Daten

Name Hai-Young Kim
Geburtstag 04.05.1979
Geburtsort Pusan, Süd Korea
Staatsangehörigkeit Süd Korea

Ausbildung

03/1995 - 02/1998 Allgemeine Hochschulreife (Geochang Gymnasium in Süd Korea).
03/1998 - 08/2001 Chemiestudium an der Yonsei Universität in Süd Korea.
08/2001 Bachelor in Chemie
09/2001 - 02/2002 Praktikum an der Yonsei Universität in der Gruppe von Prof. Dr. Weontae Lee an der Yonsei Universität in Süd Korea.
03/2002 - 02/2004 Masterarbeit mit dem Titel "NMR studies on Bioactive Peptides; human Orexin-A, Pep27 and hCD99pep" in der Gruppe von Prof. Dr. Weontae Lee an der Yonsei Universität in Süd Korea.
02/2004 Master in Biochemie
04/2004 – 11/2008 Wissenschaftlicher Mitarbeiter am Institut für biophysikalische Chemie, Abteilung NMR-basierte Strukturbiologie von Prof. Dr. Christian Griesinger am Max-Planck-Institute für Biophysikalische Chemie in Germany.
04/2004 - 10/2004 Research assistant unter der Anleitung von Prof. Dr. Markus Zweckstetter (Dr. Sigrun Rumpel) mit Title: "Backbone resonance assignment of the homodimeric, 35kDa chaperone CesT from enteropathogenic *Escherichia coli*".
10/2004 - 11/2008 Anfertigung einer Doktorarbeit unter der Anleitung von Prof. Dr. Markus Zweckstetter und Prof. Dr. Christian Griesinger; Thema der Doktorarbeit: "Characterization of the amyloid precursor α -synuclein by NMR spectroscopy".

Göttingen, den 2008